Dissertation

submitted to the

Combined Faculty of Mathematics, Engineering and Natural Sciences

of Heidelberg University, Germany

for the degree of

Doctor of Natural Sciences

Put forward by

Kilian Alexander Dietrich

born in Tübingen

Date of oral examination: 08.02.2024

Development of radiofrequency coils for magnetic resonance-guided particle therapy

Referees:

Prof. Dr. Mark E. Ladd

Prof. Dr. Leif Schröder

Entwicklung von Hochfrequenzspulen für die Magnetresonanz-geführte Partikeltherapie

Ziel dieser Arbeit war die Entwicklung von Hochfrequenzspulen, die für die Magnetresonanz (MR)-geführte Partikeltherapie geeignet sind. Für zwei verschiedene MR-Systeme (1,5 T; 0,25 T) wurde eine Sende-/Empfangs-Körperspule und eine Empfangs-Wadenspule entworfen, konstruiert, optimiert und aufgebaut. Die beiden Spulen zeichnen sich durch einen sehr dünnen Leiter (Dicke: 35 µm) und eine hohe Strahlungstransparenz aus, um eine präzise Partikeltherapie bei gleichzeitiger MR-Bildgebung zu ermöglichen. Eine vernachlässigbare wasseräquivalente Dicke (WET) des Leiters (WET: 0,18−0,19 mm) wurde anhand der Dosisverteilung in einer Wassersäule gemessen. Weiterhin sind beide MR-Spulen drehbar, um eine flexible Partikeltherapie mit Mehrwinkelbestrahlung zu ermöglichen. Eine hohe Homogenität der Sende- (Körperspule) und Empfangsfelder (beide Spulen) wurde in homogenen Phantomen für verschiedene Drehwinkel der MR-Spulen bestätigt. Die Körperspule erreichte zudem eine ausreichende Sendeleistungseffizienz ($0{,}18-0{,}27\frac{\mu T}{\sqrt{W}}$) in der zentralen Schicht für eine komplette Rotation des Phantoms. Bezüglich der Bildqualität wurde das Signal-zu-Rausch-Verhältnis (SNR) in einem homogenen Phantom gemessen, wobei die Körperspule (SNR: $109-156$) und die Wadenspule (SNR: $74-90$) kommerziellen Spulen überlegen waren. Zusätzlich wurde die Funktionalität der beiden Spulen an einem anthropomorphen Phantom (Körperspule) und in vivo (Wadenspule) demonstriert.

Development of radiofrequency coils for magnetic resonance-guided particle therapy

The aim of this work was to develop radiofrequency coils suitable for magnetic resonance (MR)-guided particle therapy. For two different MR systems (1.5 T, 0.25 T), a transmit/receive body coil and a receive-only calf coil were designed, constructed, optimized and built. The two coils are characterized by a very thin conductor (thickness: 35 µm) and high radiation transparency to enable precise particle therapy with simultaneous MR imaging. A negligible water equivalent thickness (WET) of the conductor (WET: 0.18−0.19 mm) was measured based on the dose distribution in a water column. In addition, both MR coils can be rotated, allowing flexible particle therapy with multi-angle irradiation. A high homogeneity of the transmit (body coil) and receive (both coils) fields was confirmed in homogeneous phantoms for different rotation angles of the MR coils. The body coil also achieved sufficient transmit power efficiency ($0.18-0.27\frac{\mu T}{\sqrt{W}}$) in the central slice for a complete rotation of the phantom. In terms of image quality, the signal-to-noise ratio (SNR) was measured in a homogeneous phantom, where the body coil (SNR: $109-156$) and the calf coil (SNR: $74-90$) outperformed commercial coils. Furthermore, the functionality of the two coils was demonstrated in an anthropomorphic phantom (body coil) and in vivo (calf coil).

Contents

1 Introduction **1**

2 Physical background **5**

2.1 Nuclear magnetic resonance 5
2.1.1 Nuclear spin 5
2.1.2 Zeeman splitting 6
2.1.3 Macroscopic magnetization 7
2.1.4 Time evolution of the magnetization 9
2.1.5 Radiofrequency excitation pulse 10
2.1.6 T_1 & T_2 relaxation 11
2.1.7 Circularly-polarized excitation and reception 12
2.2 Magnetic resonance imaging 14
2.2.1 Slice selection 14
2.2.2 Phase encoding 15
2.2.3 Frequency encoding 16
2.2.4 Nyquist criterion 17
2.2.5 Pulse sequences 17
2.3 Hardware 19
2.3.1 Radiofrequency coils 19
2.3.2 Local coils and volume coils 19
2.3.3 Solenoid coil 21
2.3.4 Birdcage coil 22
2.3.5 Specific absorption rate 24
2.3.6 Signal-to-noise ratio 25
2.3.7 Tuning & matching 26
2.3.8 Quality factors of radiofrequency coils 28
2.3.9 Quadrature hybrid 29
2.3.10 Transmit/receive switch 30
2.4 Electromagnetic field simulations 33
2.4.1 Finite integration technique 33
2.5 Particle range in matter 36
2.5.1 Ionization chamber 36

2.5.2 Stopping power . . . 37
2.5.3 Bragg peak . . . 38

3 Methods **39**
3.1 MR systems . . . 39
3.1.1 "Offline" 1.5 T MR system . . . 39
3.1.2 "Online" 0.25 T MR system . . . 42
3.2 Developed radiofrequency coils . . . 44
3.2.1 Concept & design . . . 44
3.2.2 Setup . . . 50
3.2.3 Phantoms . . . 54
3.2.4 Simulation models . . . 56
3.2.5 Process of tuning & matching . . . 59
3.3 Supplementary radiofrequency electronics . . . 63
3.3.1 Transmit/receive switch . . . 63
3.3.2 Quadrature hybrid . . . 66
3.3.3 Radiofrequency preamplifier . . . 68
3.4 MR image acquisition . . . 71
3.4.1 Measurements . . . 71
3.4.2 Coil calibration . . . 72
3.4.3 Mapping of transmit and receive fields . . . 72
3.4.4 Determination of signal-to-noise ratio . . . 74
3.5 Particle irradiation . . . 75
3.5.1 Ion beam facility . . . 75
3.5.2 Investigation of depth-dose curves for particles . . . 75

4 Results **79**
4.1 Radiation transparency for particles . . . 79
4.1.1 Theoretical determination of the ion attenuation . . . 79
4.1.2 Bragg peak measurements . . . 83
4.2 Body coil for 1.5 T "offline" MR system . . . 86
4.2.1 Simulated S-parameters . . . 86
4.2.2 Radiofrequency field homogeneity . . . 87
4.2.3 Power efficiency . . . 95
4.2.4 Signal-to-noise ratio . . . 97
4.2.5 Safety assessment . . . 98
4.2.6 Application in anthropomorphic phantom . . . 98
4.3 Calf coil for 0.25 T "online" MR system . . . 100
4.3.1 Simulated S-parameters . . . 100
4.3.2 Receive field homogeneity . . . 101
4.3.3 Signal-to-noise ratio . . . 102
4.3.4 In vivo imaging . . . 106

5 Discussion **109**
5.1 Radiation transparency for particles . . . 110
5.1.1 Coil components . . . 110
5.2 Imaging performance of the RF body coil . . . 112
5.2.1 Patient rotation . . . 112
5.2.2 Radiofrequency field homogeneity . . . 113
5.2.3 Transmit power efficiency . . . 114
5.2.4 Signal-to-noise ratio . . . 115
5.2.5 Specific absorption rate & maximum transmit power . . . 115
5.3 Imaging performance of the RF calf coil . . . 116
5.3.1 Receive field homogeneity . . . 116
5.3.2 Signal-to-noise ratio . . . 117
5.3.3 In vivo imaging . . . 117
5.4 Supplementary electronics . . . 118
5.4.1 Transmit/receive switch & quadrature hybrid . . . 118
5.4.2 Preamplifier . . . 119

6 Conclusion **121**

Appendix

List of figures

List of tables

Acronyms

Acknowledgements

Chapter 1

Introduction

Nuclear magnetic resonance [Bloch, 1946] [Purcell et al., 1946] (NMR) is a spectroscopic technique that uses radiofrequency (RF) coils to generate electromagnetic fields to excite nuclear spins in a static magnetic field. The resulting deflected macroscopic magnetization precesses around the static magnetic field and induces a voltage in an RF coil, also called magnetic resonance (MR) signal, which can be analyzed to provide information about the chemical composition of a substance. In magnetic resonance imaging (MRI), the NMR technique is extended with spatially dependent magnetic fields to allow spatially resolved encoding of the MR signal [Lauterbur, 1973]. Thus, cross-sectional images of the sample volume can be generated in any spatial direction, which is of particular interest for in vivo imaging. From a clinical perspective, magnetic resonance imaging is characterized by excellent soft tissue contrast and the ability to generate different image contrasts, which is relevant for screening and evaluation of various pathologies.

In cancer treatment with radiotherapy, the goal is to deliver high dose to the tumor volume while minimizing the dose to surrounding healthy tissue, especially organs at risk. Therefore, reliable classification of different tissue types is critical for dose calculation and the success of the treatment depends heavily on the quality of the imaging technique. Due to the superior soft tissue contrast of MRI compared to computed tomography (CT), MR-guided radiotherapy (MRgRT) is gaining popularity as an alternative to conventional CT-guided radiotherapy [Pollard et al., 2017]. MRI does not rely on ionizing radiation for image acquisition, therefore frequent imaging can be performed without the risk of radiation-induced secondary tumors [Dzierma et al., 2018]. Consequently, MRI is a viable tool for closely monitoring tumor size, as well as anatomical and physiological processes within the patient throughout the treatment. In addition, tolerances in patient positioning between radiation fractions can be monitored when MRI is combined with linear accelerators (linacs) in a hybrid device, allowing for interfractional adjustments to the treatment plan. Furthermore, fast MR sequences such as bSSFP [Gao et al., 2018] (balanced Steady State Free Precession) allow real-time tracking of the clinical target volume, which can be used to control beam delivery in response to organ motion

caused, for example, by respiration [Ipsen et al., 2014]. In general, adaptive radiotherapy holds great potential for increasing the effectiveness of cancer treatment [Corradini et al., 2019] [Kurz et al., 2020] [Spindeldreier et al., 2021].

MR guidance can also be combined with particle therapy to compare patient position and anatomy with the treatment plan prior to each radiation fraction, with the goal of reliably irradiating the tumor volume and improving clinical outcomes. Because of the spatially localized dose distribution of particle beams in water-like tissues, the dose to adjacent tissues can be reduced [Hoffmann et al., 2020] [Harrabi et al., 2016]. As a result, an improvement in quality of life is expected, especially for cancer treatment near radiation-sensitive tissues such as the brain stem, spinal cord, internal organs or pediatric cancers [Mitin and Zietman, 2014] [Leeman et al., 2017] [Hess et al., 2016]. In particle therapy, the relative biological effect (e.g., ratio of dose for photons and ions that results in the same biological effect) depends on the ion species [Jäkel, 2009]. Therefore, modern accelerator facilities offer a selection of ion species ($^{1}H^{+}$,$^{4}He^{2+}$,$^{12}C^{6+}$, ...) for more flexibility in irradiation. The introduction of new ion species such as $^{16}O^{8+}$ or $^{7}Li^{3+}$ and the demonstration of the clinical benefit remain subjects of ongoing research [Tommasino et al., 2016].

Although MR-guided photon therapy with linear accelerators (linacs) has been demonstrated in vivo [Raaymakers et al., 2017] and MR-linacs are commercially available, the transition to MR-guided particle therapy (MRgPT) remains an ongoing challenge. In addition to the need for complex Monte Carlo simulations to calculate particle trajectories [Oborn et al., 2015] in the static magnetic field of the MR scanner, there are special requirements for the magnet design and hardware components. Since the energy transfer of charged particles in matter is subject to inelastic Coulomb interaction with increasing energy transfer at lower energies, a sharp dose maximum (also known as a Bragg peak) appears toward the end of the penetration depth. Therefore, even small deviations in the ion beam energy or tissue distribution from the treatment plan can significantly reduce the quality of the treatment. Accordingly, all materials in the path of the ion beam must be considered in the treatment plan. While homogeneous materials with a known water equivalent thickness (WET) can be compensated by higher initial beam energies, unknown heterogeneous materials or positioning will result in undefined penetration depths and uneven beam scattering. The WET is highly dependent on the density of the penetrated material. Therefore, highly attenuating electronic components such as those found in an RF coil (e.g., capacitors, preamplifiers, ...) should be avoided in the path of the ion beam. In addition, a small conductor thickness of the RF coil is favorable to minimize ion attenuation. However, the imaging quality of an RF coil also depends on adequate power transmission, resulting in a minimum thickness of the conductor defined by the skin depth for the given frequency.

In radiotherapy, it is often advantageous to irradiate from multiple angles, allowing better adaptation of the dose distribution to the tumor volume and better sparing of organs at risk. In contrast to MR-linacs with a compact photon source, where patient irradiation from multiple angles is relatively easy to implement, particle therapy requires large accelerator systems and treatment flexibility is difficult to achieve. Since the ions are accelerated to relativistic energies, deflection of the ions is challenging and requires a large and expensive ion gantry [Haberer et al., 2004], which is beyond the scope of many treatment centers. A possible alternative is the implementation of a patient rotation system to enable multi-angle irradiation even for accelerator centers with a fixed ion source, thus providing greater treatment flexibility. The feasibility of subject rotation has already been demonstrated in combination with an MR-linac [Whelan et al., 2017] [Buckley et al., 2019] [Buckley et al., 2020]. The high soft tissue contrast of MRI can be used to detect changes in body contours and organ displacements that may occur due to different directions of gravity at different rotation angles. For "on-table" adjustment of the treatment plan, a deformable image registration [Bohoudi et al., 2017] [Acharya et al., 2016] could be implemented to recalculate the dose distribution with the Monte Carlo simulations.

The main objective of this thesis was to design and construct radiofrequency coils compatible with MR-guided particle therapy and patient rotation for flexible treatment. In this context, two rotatable, radiation-transparent RF coils were designed and the influence of the coil components on an ion beam was investigated.

In a first step, a rotatable and radiation-transparent transmit/receive body coil with a suitable geometry was designed for a 1.5 T MR system with an implemented patient rotation system. For optimal performance in body imaging, the RF coil should be characterized by a homogeneous transmit and receive field over a large area and a high signal-to-noise ratio (SNR). To investigate the influence of patient rotation on the transmit and receive characteristics of the RF body coil, electromagnetic (EM) field simulations and MR measurements were performed for different rotation angles.

In a second step, a rotatable and radiation-transparent receive-only RF calf coil for extremities such as the human calf or hand was designed and constructed for a 0.25 T MR system. The coil geometry was designed and investigated in EM field simulations for different rotation angles to achieve a homogeneous sensitivity profile. In addition, the SNR of the RF calf coil was measured and compared to commercially available coils. Furthermore, the imaging performance of the RF calf coil was also investigated in vivo.

Parts of this work have already been presented at conferences or submitted as a research article to a journal (see Appendix).

Chapter 2

Physical background

In this chapter, both the physical principles of nuclear magnetic resonance as well as the most important aspects for the design process of transmit and receive coils are considered. The functionality of the high-frequency components used in this thesis and the simulation of electromagnetic fields are discussed. Furthermore, the concepts of radiation therapy, especially particle therapy, are explained.

2.1 Nuclear magnetic resonance

This section deals with the underlying theory of nuclear magnetic resonance and is based on the works of [Callaghan, 1993] [Slichter, 1978] [Abragam, 1983]. For a deeper insight into the theory of nuclear magnetic resonance, reference is made to the books mentioned.

2.1.1 Nuclear spin

The quantum state of a nucleus is characterized by the spin quantum number I and the magnetic quantum number m_I. I describes the intrinsic spin angular momentum of a nucleus in the ground state while m denotes the azimuthal component of the spin orientation in space, which can assume values between $-I$ and $+I$ in steps of 1 $(-I, -I+1, ..., +I-1, +I)$. It should be noted that the x, y and z orientations of the nuclear spin cannot be determined simultaneously, which is directly related to the commutator relation $[\hat{I}_i, \hat{I}_j] = i\hbar\hat{I}_k$. Since $[\hat{\boldsymbol{I}}^2, \hat{I}_z] = 0$ holds, the magnitude of the nuclear spin and an axial component (usually in the z direction) are chosen to determine the quantum state $|I, m_I\rangle$ of a nucleus. This representation leads to the following eigenvalue equations:

$$\hat{\boldsymbol{I}}^2 |I, m_I\rangle = I(I+1)\hbar^2 |I, m_I\rangle \tag{2.1}$$

$$\hat{I}_z |I, m_I\rangle = m_I\hbar |I, m_I\rangle \tag{2.2}$$

In this context, $I(I+1)\hbar^2$ and $m_I\hbar$ can be understood as the results of an observation. The nuclear spin leads to a magnetic dipole moment $\hat{\boldsymbol{\mu}}$ which is proportional to the angular momentum:

$$\hat{\boldsymbol{\mu}} = \gamma \hat{\boldsymbol{I}} \tag{2.3}$$

where γ describes the gyromagnetic ratio of the nucleus. This fundamental property is related to the g-factor of the nucleus g_n and the the nuclear magnetron μ_N via:

$$\gamma_n = g_n \frac{\mu_N}{\hbar} \qquad \text{with} \qquad \mu_N = \frac{e\hbar}{2m_p} \tag{2.4}$$

where m_p denotes the proton rest mass.

2.1.2 Zeeman splitting

In the presence of an external static magnetic field $\boldsymbol{B}$, the interaction energy of a magnetic dipole corresponds to:

$$\hat{H} = -\boldsymbol{\mu} \cdot \boldsymbol{B} \tag{2.5}$$

In the case where the magnetic field is oriented in the z direction $\boldsymbol{B} = (0, 0, B_0)$, the Hamiltonian operator can be written as follows:

$$\hat{H} = -\gamma\hbar B_0 \hat{I}_z \tag{2.6}$$

For nuclei with an odd mass number and/or an odd number of protons and neutrons, more than one energy state is allowed ($I \neq 0$). This degeneracy of energy levels is known as Zeeman splitting. The eigenvalues of eq. 2.2 directly define the number and the energy E_m of the allowed energy states of the quantum system:

$$\hat{H}\,|I, m_I\rangle = E_m\,|I, m_I\rangle \tag{2.7}$$

$$\hat{H}\,|I, m_I\rangle = -\gamma\hbar m B_0\,|I, m_I\rangle \tag{2.8}$$

This results in $2I + 1$ equidistant energy levels separated by:

$$\Delta E = E_m - E_{m+1} \tag{2.9}$$

$$\Delta E = \hbar\gamma B_0 \tag{2.10}$$

$$\Delta E = \hbar\omega_L \tag{2.11}$$

The frequency ω_L defines the energy absorbed or emitted during a transition between two quantum states. This frequency is called the Larmor frequency and depends on the applied magnetic field:

$$\omega_L = \gamma B_0 \tag{2.12}$$

The gyromagnetic ratio γ of hydrogen nuclei corresponds to [Harris et al., 2002]:

$$\frac{\gamma}{2\pi} \approx 42.577 \frac{\text{MHz}}{\text{T}} \tag{2.13}$$

If $I = \frac{1}{2}$, the Zeeman effect leads to a splitting of the two degenerate energy states, as shown in fig. 2.1. Moreover, the lower energy state ($I_z = +\frac{1}{2}$), corresponding to an alignment of the nuclear spins parallel to B_0, is slightly favored and therefore more frequently occupied.

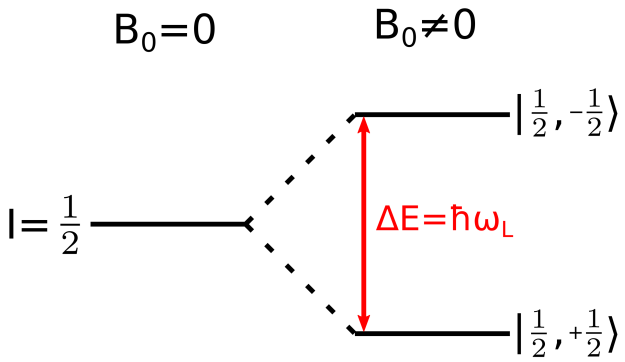

Figure 2.1: Energy level scheme for a nucleus with $I = \frac{1}{2}$. When an external magnetic field B_0 is applied, Zeeman splitting occurs, which leads to a degeneracy of the allowed energy levels. The energy difference between two quantum states is given by $\Delta E = \hbar\omega_L$.

A prominent example of a two-state energy level scheme is hydrogen, which plays a special role in nuclear magnetic resonance because of its abundance in many liquid substances as well as in human tissues.

2.1.3 Macroscopic magnetization

The above properties apply to a single nucleus, but nuclear magnetic resonance deals with large spin ensembles. For a group of nuclear spins, the total magnetic moment can be determined from the sum of all individual magnetic moments in the ensemble:

$$\boldsymbol{\mu} = \sum_k \boldsymbol{\mu_k} \tag{2.14}$$

From a quantum mechanical point of view, the individual nuclei can assume different states at any time. Therefore, the expectation value averaged over the ensemble must be considered to obtain the macroscopic magnetic moment. If p_m is the probability that a nuclear spin ensemble occupies the state $|I, m_I\rangle$, then the ensemble-averaged expectation value of the nuclear magnetic moment in the z direction μ_z is given by:

$$\langle \hat{\mu}_z \rangle = \overline{\langle I, m_I | \hat{\mu}_z | I, m_I \rangle} = \sum_m p_m \langle I, m_I | \hat{\mu}_z | I, m_I \rangle \tag{2.15}$$

In thermal equilibrium, the occupation probability of states for a spin ensemble is determined by a Boltzman distribution with temperature T and Boltzman constant k:

$$p_m = \frac{e^{-E_m/kT}}{Z} \qquad \text{with} \qquad Z = \sum_m e^{-E_m/kT} = 2I + 1 \tag{2.16}$$

Similarly, the averaging of a spin ensemble can also be described by the density matrix $\hat{\rho}$ with basis $(|\phi\rangle, |\psi\rangle)$:

$$\hat{\rho} = \langle \phi | \hat{\rho} | \psi \rangle = \sum_m p_m \langle \phi | I, m_I \rangle \langle I, m_I | \psi \rangle \tag{2.17}$$

The expectation value for any operator $\hat{O}$ can then be expressed as the diagonal entries of the matrix product with the density operator ρ:

$$\langle \hat{O} \rangle = Tr(\hat{O}\hat{\rho}) \tag{2.18}$$

From eq. 2.8 it follows that the energy gap between the eigenstates $|I, m_I\rangle$ of the quantum system is given by $\Delta E_m = \gamma \hbar m B_0$. At room temperature, the energy splitting is much smaller than the Boltzman energy ($\gamma \hbar B_0 << kT$) and the occupation probability from eq. 2.16 can be approximated by a first order Taylor series expansion:

$$p_m \approx \frac{1}{2I+1}\left(1 + \frac{\gamma \hbar m B_0}{kT}\right) \tag{2.19}$$

For a sample with a total number of nuclei N per volume V, the net macroscopic magnetization in the z direction can be expressed as follows:

$$M_z = \frac{N}{V} \cdot \overline{\langle I, m_I | \, \hat{\mu_z} \, | I, m_I \rangle} \tag{2.20}$$

$$\approx \frac{N}{V} \frac{1}{2I+1} \cdot \sum_m \gamma \hbar m \left(1 + \frac{\gamma \hbar m B_0}{kT} \right) \tag{2.21}$$

$$= \frac{N}{V} \frac{\gamma^2 \hbar^2 I(I+1) B_0}{3kT} \tag{2.22}$$

Thus, the net macroscopic magnetization depends on the number of nuclei N in the sample volume V, the gyromagnetic ratio γ of the nuclei, the temperature T of the sample, the nuclear spin I, and the external magnetic field B_0.

2.1.4 Time evolution of the magnetization

In quantum mechanics, the time evolution of a quantum state ψ is defined by the Schrödinger equation:

$$i\hbar \frac{\partial}{\partial t} |\psi(t)\rangle = H \, |\psi(t)\rangle \tag{2.23}$$

Similarly, the time evolution of the density matrix can be described by the Liouville-von Neumann equation:

$$i\hbar \frac{\partial \rho}{\partial t} = [H, \rho] \tag{2.24}$$

If the an observed quantity $\hat{A}$ is not explicitly time-dependent, the time evolution of the expectation value $\langle \hat{A} \rangle$ can be calculated by transforming eq. 2.24:

$$\frac{d}{dt} \langle \hat{A} \rangle = \frac{i}{\hbar} \langle [H, \hat{A}] \rangle \tag{2.25}$$

For a nuclear spin ensemble, eq. 2.25 yields the equation of motion for the macroscopic magnetization:

$$\frac{d\boldsymbol{M}(t)}{dt} = \gamma \boldsymbol{M}(t) \times \boldsymbol{B}(t) \tag{2.26}$$

It follows that the macroscopic magnetization will precess around the axis of the magnetic field unless the macroscopic magnetization is aligned parallel or antiparallel to it. Furthermore, the time evolution of the macroscopic magnetization can be manipulated by changing the applied magnetic field.

2.1.5 Radiofrequency excitation pulse

In addition to a static magnetic field $\boldsymbol{B_0} = (0, 0, B_0)$, an additional radiofrequency (RF) field $\boldsymbol{B_1}$ can be applied to change the orientation of the magnetization:

$$\boldsymbol{B}(t) = \boldsymbol{B_0} + \boldsymbol{B_1}(t) \tag{2.27}$$

In the laboratory reference frame, the magnetic field $\boldsymbol{B}(t)$ acting on the magnetization can be described as follows:

$$\boldsymbol{B}(t) = \begin{pmatrix} B_1 \cdot cos(\omega_{RF} \cdot t) \\ B_1 \cdot sin(\omega_{RF} \cdot t) \\ B_0 \end{pmatrix} \tag{2.28}$$

A more intuitive description of the system is obtained by performing a coordinate transformation into the rotating reference frame ($\sim$). For this purpose, the laboratory reference frame is rotated around the z axis with the frequency of the RF pulse ($\Omega = \omega_{RF}$), resulting in a simplified version of eq. 2.26 without explicit time dependence:

$$\frac{d\tilde{\boldsymbol{M}}(t)}{dt} = \gamma \tilde{\boldsymbol{M}}(t) \times \tilde{\boldsymbol{B}} \qquad \text{with} \qquad \tilde{\boldsymbol{B}} = \begin{pmatrix} B_1 \\ 0 \\ B_0 - \frac{\Omega}{\gamma} \end{pmatrix} \tag{2.29}$$

If the excitation pulse corresponds to the Larmor frequency ($\Omega = \omega_L$), an effective magnetic field $\tilde{\boldsymbol{B}} = (B_1, 0, 0)$ can be generated, which is stationary in the rotating frame and orthogonal to B_0 along the x axis. In this case, the B_1 field is orthogonal to the macroscopic magnetization of the ground state nuclei, and coherent excitation of the nuclear spins leads to an oscillation of the macroscopic magnetization $\tilde{M}$ on the $\tilde{y}$z plane in the rotating reference frame. For nuclei with a two-state system (see figure 2.1), the occupation probability of the two states during the pulse can be described by the Rabi oscillation [Foot, 2004]. Thus, the most efficient manipulation of the magnetization can be achieved if the RF pulse is applied exactly in resonance with the Larmor frequency ($\omega_{RF} = \omega_L$).
The angle in the $\tilde{y}$z plane between the macroscopic magnetization before (ground state) and after the pulse (excited state) is referred to as flip angle. The total flip angle α is defined by the amplitude of the applied RF pulse integrated over the pulse duration t_{pulse}:

$$\alpha = \int_0^{t_{pulse}} \gamma |B_1(t)| dt \tag{2.30}$$

B_1 can take any shape over the pulse duration, but in the case of a rectangular RF pulse, the flip angle can be simplified to:

$$\alpha = \gamma B_1 t_{pulse} \tag{2.31}$$

Since $|\boldsymbol{B_1}| << B_0$ holds for all practical cases, it can be assumed that the B_1 field has no effect on the energy levels of the system and the Larmor frequency remains constant.
Moreover, circularly-polarized (CP) pulses lead to a more efficient excitation of the magnetization than linearly-polarized (LP) pulses, since the B_1 field of CP pulses remains orthogonal to the magnetization in the rotating reference frame (see eq. 2.29). A more detailed explanation is given in section 2.1.7.

2.1.6 $\mathbf{T_1}$ & $\mathbf{T_2}$ relaxation

After the excitation pulse, the transverse magnetization $M_\perp$ continues to rotate around the z axis in the laboratory frame. If an RF coil is placed along the x or y axis, an RF signal at the Larmor frequency can be detected via induced currents in the coil.
Infinite motion of the magnetization in the transverse plane is only valid if the interactions between the nuclei and their surroundings are neglected. In reality, the nuclei exchange energy with the environment and the magnetization returns to the energetically preferred ground state, where the magnetization is aligned along the z axis, parallel to B_0. This decay is characterized by the relaxation time T_1 and is referred to as spin-lattice relaxation. In addition, dipole-dipole interactions between neighboring nuclei can lead to local energy loss and dephasing of the spin ensemble. This effect is called spin-spin relaxation and can be described by the relaxation time T_2 which is usually shorter than T_1. Taking these decay parameters into account, eq. 2.29 can be transformed into the Bloch equations:

$$\frac{dM_x(t)}{dt} = \gamma(\boldsymbol{M}(t) \times \boldsymbol{B}(t))_x - \frac{M_x(t)}{T_2} \tag{2.32}$$

$$\frac{dM_y(t)}{dt} = \gamma(\boldsymbol{M}(t) \times \boldsymbol{B}(t))_y - \frac{M_y(t)}{T_2} \tag{2.33}$$

$$\frac{dM_z(t)}{dt} = \gamma(\boldsymbol{M}(t) \times \boldsymbol{B}(t))_z - \frac{M_z(t) - M_0}{T_1} \tag{2.34}$$

In addition to the naturally occurring dephasing of a spin ensemble due to dipole-dipole interactions, inhomogeneities in the B_0 field can also cause dephasing of the spin ensemble due to different Larmor frequencies in the sample volume. This dephasing effect of the transverse magnetization can be described by an additional decay parameter T_2^*, which in this case replaces T_2 and which is usually shorter than

the spin-spin relaxation time ($T_2^* < T_2$). T_1, T_2 and T_2^* are substance-dependent parameters and depend mainly on the applied field strength B_0 and the molecular tumbling rate, which is influenced by the chemical structure and the temperature of the sample. After the excitation pulse, the MR signal induced in a nearby RF coil corresponds to a free induction decay (FID) with the characteristic relaxation time T_2 or T_2^*, depending on the applied MR sequence (see section 2.2.5).

2.1.7 Circularly-polarized excitation and reception

A B_1 field rotating in the xy plane, generated by an RF coil to manipulate the magnetization (see section 2.1.5) can be separated into a co-rotating component ($\tilde{B}_1^+$), which rotates in the same direction as the rotating reference system ($\sim$) or the magnetization, and a component with opposite direction of rotation ($\tilde{B}_1^-$). Both rotating field components can be described by the x and y components of the B_1 field in the laboratory system [Hoult, 2000]:

$$\tilde{B}_1^+ = \frac{B_{1,x} + iB_{1,y}}{2} \qquad \tilde{B}_1^- = \frac{B_{1,x}^* + iB_{1,y}^*}{2} \tag{2.35}$$

where (*) denotes the complex conjugate.

Using the rotating wave approximation [Foot, 2004], it can be assumed that the RF field component rotating in the opposite direction of the rotating reference frame (B_1^-) does not contribute to the deflection of the magnetization and can therefore be neglected during transmission. However, the RF field component rotating in the same direction as the magnetization (B_1^+) should be maximized to increase power efficiency and achieve efficient manipulation of the magnetization. In the case of reception, the RF signal is transmitted from the rotating nuclear magnetization to the RF coil and thus has opposite polarization [Vaidya et al., 2016]. Consequently, the B_1^- field corresponds to the receive sensitivity profile of the RF coil.

A linearly-polarized B_1 field can be decomposed into two circularly-polarized components, each with half the amplitude oriented along the initial B_1 field ($\frac{|B_1|}{2}$) and opposite angular direction of rotation (see fig. 2.2).

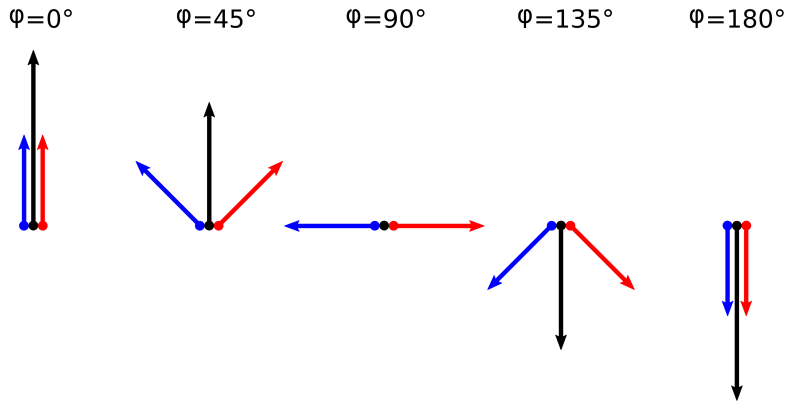

Figure 2.2: Decomposition of a linearly-polarized RF field into circularly-polarized field components with opposite angular directions of rotation. The superposition of the clockwise (red) and counterclockwise (blue) components corresponds to the linearly-polarized RF field (black).

Perfectly circularly-polarized transmit fields require only half the power to achieve the same flip angle as linearly-polarized transmit fields [Glover et al., 1985]. Furthermore, quadrature detection allows all components of the circularly-polarized MR signal to be detected, increasing the sensitivity by a factor of $\sqrt{2}$ [Chen et al., 1983]. A circularly-polarized transmit field (B_1^+) can be achieved with two orthogonally aligned coils, each driven with an excitation pulse of equal amplitude and a phase difference of 90° corresponding to the precession direction of the magnetization. For birdcage coils, a quadrature hybrid (see section 2.3.9) can be used to provide circularly-polarized transmit or receive fields.

2.2 Magnetic resonance imaging

This section introduces the concept of spatial encoding using gradient fields in combination with RF pulses and is based on the books of [Bernstein et al., 2004], [Haacke et al., 2014], [Callaghan, 1993] and [Schlegel et al., 2018], where a more detailed description of magnetic resonance imaging can be found. In order to use nuclear magnetic resonance for imaging, it is necessary to distinguish NMR signals by the location of the signal. As mentioned earlier in eq. 2.12, the Larmor frequency depends on the applied magnetic field. Therefore, gradient fields with non-constant magnetic field strengths in the z direction are required to obtain a spectrum of Larmor frequencies for different volume subunits within the sample. In three dimensions, these subunits are called voxels. Each orthogonal field gradient provides additional spatial information, allowing, for example, the assignment of the position of the MR signal in the sample for another dimension. Therefore, three gradient fields are sufficient to uniquely address each voxel in the sample. Since a linear correlation between the voxel position and the Larmor frequency is favorable, linear gradient fields are preferred. The gradient fields can be time-dependent and are superimposed on the static magnetic field B_0:

$$B_z = B_0 + G_x(t) \cdot x + G_y(t) \cdot y + G_z(t) \cdot z \tag{2.36}$$

$$= B_0 + \frac{\partial B_z(t)}{\partial x} \cdot x + \frac{\partial B_z(t)}{\partial y} \cdot y + \frac{\partial B_z(t)}{\partial z} \cdot z \tag{2.37}$$

Generally, the three gradient fields can be chosen in any direction as long as they are orthogonal to each other.

2.2.1 Slice selection

If a field gradient G_{slice} is applied in the z direction, the Larmor frequency changes according to $\omega_L(z) = \gamma(B_0 + G_{slice} \cdot z)$ and thus depends on the position along the z axis. Consequently, an RF pulse transmitted simultaneously with the gradient field will result in resonant excitation in one slice of the sample rather than in the entire volume. As shown in fig. 2.3, the thickness of the slice is determined by the strength of the gradient field. Larger field strengths reduce the slice thickness, resulting in higher spatial resolution. Considering the bandwidth $\Delta\omega$ of the RF pulse, the slice thickness along the z axis can be defined as follows:

$$\Delta z = \frac{\Delta\omega}{\gamma G_{slice}} \tag{2.38}$$

This technique allows the excitation of a single slice in the gradient isocenter. To change the position of the slice along the z axis, the carrier frequency of the RF

pulse must match the Larmor frequency of a different position on the z axis. Thus, a complete three dimensional (3D) image dataset of the sample volume can be obtained by acquiring a stack of two dimensional (2D) slices, each with a different carrier frequency of the RF pulse.

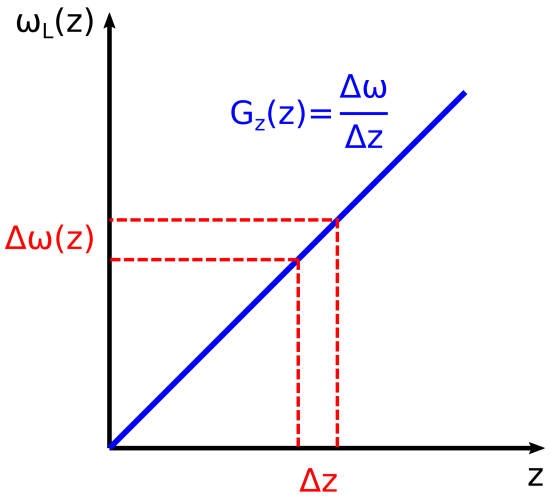

Figure 2.3: A linear gradient field for slice selection in the z direction G_z allows for uniform spatial encoding, where the relationship between the bandwidth ($\Delta\omega$) and the slice thickness (Δz) depends on the slope of the gradient.

2.2.2 Phase encoding

After the magnetization of the nuclei has been transferred to the transverse plane by the RF pulse, a gradient field can be applied in another direction. If a gradient field G_{PE} is applied along the y axis for a duration T, the transverse magnetization $M_\perp = M_x + iM_y$ rotates in the xy plane with a different Larmor frequency and the nuclei along the y axis accumulate a phase equal to:

$$\phi(y) = \int \omega(y)dt \tag{2.39}$$

$$= \gamma y \int_0^T G_{PE}(t)dt \tag{2.40}$$

$$= 2\pi k_y y \qquad \text{with} \qquad k_y = \frac{\gamma}{2\pi}\int_0^T G_{PE}(t)dt \tag{2.41}$$

k_y has the unit of inverse distance and describes the y axis of the k-space in the frequency domain, which represents the Fourier transform of the MR image. For a point source, the MR signal S is characterized by the complex sum of the magnetization including a factor describing the phase of the nuclear spins along the y axis:

$$S(k_y) \propto \int |M_\perp(y)| \cdot e^{-i\phi(y)} dy \tag{2.42}$$

For a discrete set of different gradient fields, the integral from eq. 2.42 can be approximated with discrete steps Δy along the y axis:

$$S(k_y) \propto \sum_{n=0}^{N_y-1} |M_\perp(n\Delta y)| \cdot e^{-2\pi i \cdot n\Delta y \cdot k_y} \tag{2.43}$$

The summed MR signal of all nuclear spins within a step Δy, can be assigned to the respective position along the y axis. This procedure is repeated for N_y RF pulses and different gradient field strengths G_{PE} that are equidistant from each other, resulting in N_y different accumulated phases of the transverse magnetization according to eq. 2.41. The gradient field is chosen such that $0 < \phi < 2\pi$ holds and a unique relationship between position and phase of the MR signal is obtained. The accumulated phase of the MR signal is compared to the initial phase, providing information about the position along the y axis.

2.2.3 Frequency encoding

Spatial encoding along the x axis can be achieved by applying a gradient field G_{FE} in the x direction during the readout of the MR signal. Similar to the phase encoding, the spins begin to accumulate different phases along the x axis and the MR signal from eq. 2.42 changes to:

$$S(k_x, k_y) \propto \iint |M_\perp(x, y)| \cdot e^{-i(\phi(x,t)+\phi(y))} dx dy \tag{2.44}$$

$$= \iint |M_\perp(x, y)| \cdot e^{-i \cdot 2\pi(k_x(t)x + k_y y)} dx dy \tag{2.45}$$

The main difference between phase encoding and frequency encoding is the time at which the gradient field is applied: While the gradient field for phase encoding is turned off before the MR signal is acquired, the gradient for frequency encoding is applied during signal acquisition, resulting in a time-dependent phase $\phi(x, t)$ along the x axis. Therefore, the MR signal can be sampled along the x axis with a single RF pulse.
The spatially encoded magnetization can be obtained from the acquired signal by inverse Fourier transformation:

$$M_\perp(x, y) \propto \iint S(k_x(t), k_y) \cdot e^{i(\phi(x,t)+\phi(y))} dk_x dk_y \tag{2.46}$$

Similar to the phase encoding in eq. 2.43, the data acquisition is discrete and the sampling is divided into N_x uniformly distributed dwell times. Thus, each slice of a sampled object is represented by a discrete set of MR signals $S(k_x^m, k_y^n)$. If the central position $k_x = k_y = 0$ of the k-space is defined at $G_x = G_y = 0$, the transverse magnetization for each position (x_i, y_j) in a slice of the sampled object can be written as follows:

$$M_\perp(x_i, y_j) \propto \sum_{m=0}^{N_x-1} \sum_{n=0}^{N_y-1} S(k_x^m, k_y^n) \cdot e^{i(mx_i\Delta k_x + ny_j\Delta k_y)} \tag{2.47}$$

A particularly efficient calculation of the final MR image can be achieved using the Fast Fourier Transform (FFT) algorithm [Cooley and Tukey, 1965]. In combination with the slice selection, a discrete 3D image dataset of the sample volume can be acquired.

2.2.4 Nyquist criterion

The nominal resolution of any spatial coordinate Δs of an MR image is related to the total number N_s of sampled points in k-space and the corresponding step Δk_s along the axis:

$$\Delta s = \frac{1}{N\Delta k_s} \tag{2.48}$$

A discrete sampling rate leads to a maximum image size at which the spatial mapping remains unambiguous and the MR image can be reconstructed without artifacts. This limit can be defined as the field of view (FOV) along each axis of k-space:

$$FOV = \frac{1}{\Delta k_s} \tag{2.49}$$

2.2.5 Pulse sequences

The entire imaging procedure consists of a series of RF pulses, gradient fields, and signal acquisitions. Two of the most common pulse sequences are the spin echo (SE) and gradient echo sequences (GRE).
The spin echo sequence begins with a gradient field for slice selection and a SINC-shaped RF pulse that flips the magnetization by 90°. In this way, the excitation pulse takes a rectangular shape in the frequency domain, and the same flip angle can be achieved for the entire slice. Afterwards the phase encoding gradient changes the phase along one axis in the slice, a second RF pulse is applied at time $\frac{T_E}{2}$ with a flip angle of 180° to reverse the dephasing effect of the T_2^* decay. As a result, the

excited spins rephase and an echo signal appears at time T_E after the initial pulse. The gradient field of the frequency encoding results in the acquisition of an complete line in k-space. Before a new excitation pulse can be applied, it is necessary to wait for the magnetization to decay back to the ground state in parallel with B_0. The time between two consecutive 90° excitation pulses is called the repetition time T_R. T_E, T_R and the flip angle of the RF pulse are adjustable sequence parameters and can be used to obtain different image contrasts [Jung and Weigel, 2013].
By taking advantage of the different T_1 relaxation times in different tissue types (e.g., water, fat, muscle,...), a T_1-weighted contrast can be obtained by selecting a short T_R and a short T_E. Similarly, different tissue contrasts can be obtained based on their specific T_2 relaxation time by choosing both a long T_R and a long T_E. A proton density weighted MR image is obtained with long T_R and short T_E.
In the gradient echo sequence, no second RF pulse is used to rephase the excited spins. Therefore, the MR signal is acquired from the initial free induction decay (FID), and the image contrast is affected by the T_2^* decay. Accordingly, with a long T_E and a long T_R, a T_2^*-weighted image contrast is obtained [Markl and Leupold, 2012]. If a flip angle of less than 90° is chosen, the magnetization quickly decays back to the ground state, greatly reducing T_R for an almost complete relaxation.

2.3 Hardware

This section provides an insight into the design and function of RF coils and additional electrical components used in magnetic resonance applications. In MRI, typical field strengths between 0.2 T and 7 T for the static magnetic field B_0 result in a Larmor frequency in the range of about 10−300 MHz, according to eq. 2.12. Therefore, many RF technologies from the broadcast and cell phone sectors can be adopted for the development of MR coils.

2.3.1 Radiofrequency coils

RF coils are a critical part of the MR scanner as they represent the link between the electronics for pulse generation or image acquisition and the object being measured. Consequently, the image quality is highly dependent on the quality of the RF coil. In general, a distinction can be made between transmit and receive coils. The transmit coil transmits a radiofrequency pulse from the MR scanner to the object to be measured, so that in the standard case hydrogen nuclei are excited from their ground state. The receive coil, on the other hand, is needed to detect the signal emitted by the precessing magnetization. Separate coils are often used to transmit the RF pulse and receive the MR signal. However, so-called transceiver (transmit/receive) coils can be used for both applications if an RF switch (see section 2.3.10) is installed to separate the transmit path from the receive path of the RF coil.

2.3.2 Local coils and volume coils

The type of coil depends on the task of the coil, accordingly different types of coils are beneficial for transmission and reception of RF signals. For transmit coils, the transmit field should be as homogeneous as possible, while the receive coil should achieve a maximum signal-to-noise ratio (SNR) (see section 2.3.6). For signal acquisition in the receive case, local coils are often used that can be positioned close to the object to be imaged to increase sensitivity. This can be achieved for example with surface coils, consisting of a simple conductor loop coil with capacitors and a matching network (see section 2.3.7). In addition, multiple loops can be combined into a coil array to receive the MR signal over a larger area and to better match the coil geometry to the shape of the object being measured. In addition, the measurement time can be reduced with parallel imaging [Hamilton et al., 2017]. The shape of surface coils allows for a high signal-to-noise ratio in close proximity to the coil. However, the sensitivity of surface coils is locally limited and the depth of penetration into tissue is shallow. Furthermore, the receive field is highly inhomogeneous and dependent on the coil geometry.
For a transmit coil, a homogeneous excitation profile in a large volume is usually desired since, in that case the flip angles of the excited nuclei differ only slightly,

and uniform magnetization and thus image contrasts can be achieved.
In human MRI, volume coils are often combined with local surface coils to take advantage of both coil configurations. The resonance frequency of the receive coil can be detuned during excitation of the nuclei to avoid coupling with the transmit coil during transmission of an RF pulse in the transmit coil, which can damage the receive coil preamplifier and pose a safety risk to the patient. The receive coil can be detuned using either an actively controlled RF circuit or passive components. For the transmit coil, detuning of the resonance frequency during signal acquisition is required to avoid coupling with the receive coil, which can cause image artifacts. If volume coils are used to transmit the RF pulse and receive the MR signal (so-called transmit/receive (Tx/Rx) coils), an RF switch is required to separate the transmit path from the receive path (see section 2.3.10). Since the distance between a volume coil and the patient is usually greater than with surface coils, often less voltage is induced during signal acquisition, resulting in a lower signal-to-noise ratio, especially at the patient's surface.

2.3.3 Solenoid coil

The solenoid coil is an example of a volume coil and consists of a spiral conductor with multiple turns around the object to be imaged and at least one capacitor (see fig. 2.4).

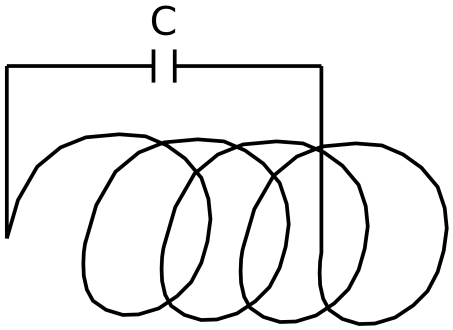

Figure 2.4: Schematic illustration of a solenoid coil with a capacitor on the conductor to adjust the resonance frequency.

A solenoid coil of infinite length results in a very homogeneous magnetic field B_1 within the enclosed volume and also achieves high sensitivity in receiving the MR signal. While the sensitivity of a solenoid does not depend on the number of turns [Mispelter et al., 2006], the RF field homogeneity is affected by a large distance between two adjacent turns. Both the number of turns and the length of the coil are limited in reality, thus RF field inhomogeneities can be expected in a real setup, especially near the conductor and at the coil openings. This effect can be partially corrected if the turns of the solenoid coil are not evenly distributed along the coil length and the distance between two adjacent turns decreases near the coil end [Leifer, 1993].
The B_1 field of a solenoid coil is linearly-polarized and axially aligned. Since the B_1 field must be orthogonal to the B_0 field to excite the magnetization, and today's clinical MR scanners often have an axial bore along the B_0 field to position the patient, the in vivo use of solenoids is limited to small animal imaging or applications at MR scanners with a different B_0 field direction (e.g., C-shaped magnets).
In addition, the inductance increases sharply with the radius and the number of turns of the solenoid coil, so that the resonance frequency decreases rapidly with the size of the object to be imaged (see eq. 2.57). Since the imaging performance depends primarily on the ratio of wavelength to coil size, a solenoid coil is often used for small sample volumes and for low-field MR scanners where orientation perpendicular to the B_0 field is possible. The solenoid coil is also suitable for NMR spectroscopy.

2.3.4 Birdcage coil

Another type of a homogeneous resonator is the birdcage coil [Hayes et al., 1985] [Tropp, 1989]. This resonator is rotationally symmetric and consists of two conductive end rings with several rungs between them and capacitors distributed on the conductor to match the resonance frequency to the Larmor frequency (see section 2.3.7). The arrangement of the capacitors determines the characteristics of the resonator and can be divided into the low-pass and high-pass configurations [Pascone et al., 1991]. A schematic representation of the two birdcage configurations, including the electronic components, is shown in fig. 2.5.

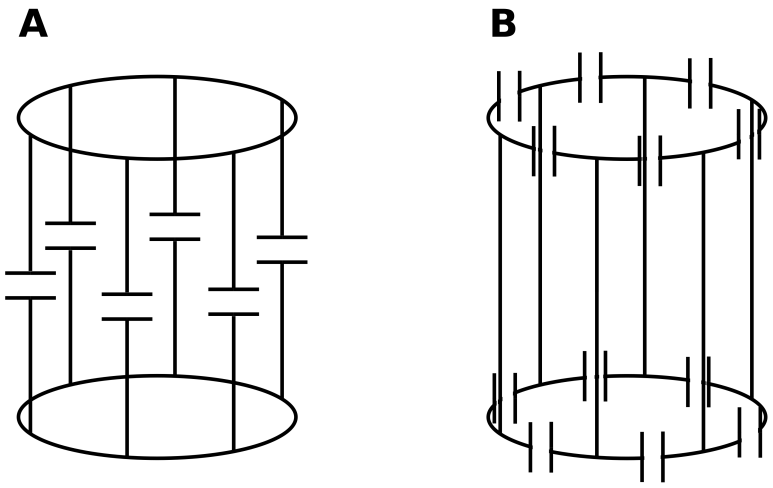

Figure 2.5: Schematic illustration of a birdcage resonator in a low-pass (**A**) and high-pass (**B**) configuration with tuning capacitors located either on the rungs or the end rings.

Depending on the configuration, different resonance modes can be generated in the birdcage resonator. A larger number N of rungs improves the homogeneity of the transmit and receive fields [Mispelter et al., 2006], but also increases the complexity of the resonator and the number of resonance modes.

If the birdcage resonator is connected to the scanner at only one point, only a linearly-polarized B_1 field can be generated. To achieve circular polarization, the birdcage coil can be connected to the scanner at, for example, two points with a 90° phase difference in the current distribution (e.g., on one of the end rings (see fig. 2.5) separated by a quarter circle). If an RF signal at the resonance frequency with the same amplitude and a phase difference of 90° is applied to both connections, the resulting B_1 field of a birdcage coil is oriented perpendicular to the coil axis and rotates in the transverse plane (see fig. 2.6).

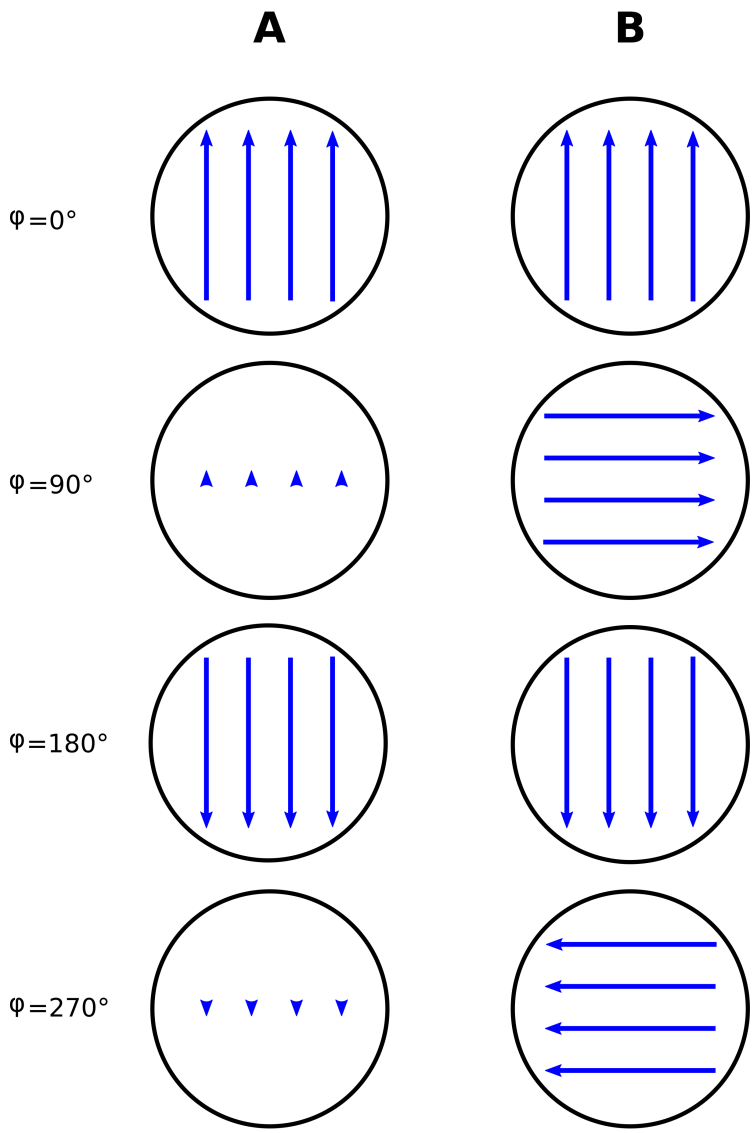

Figure 2.6: Illustration of a linearly-polarized (**A**) and a circularly-polarized (**B**) B_1-field (blue) for different phases (φ) generated in a birdcage resonator. For circular polarization of the B_1 field, the RF power must be fed into two ports with an ideal phase difference of 90°, where the sign defines the direction of rotation.

Similarly, a birdcage coil with quadrature reception can detect both components of the MR signal in the transverse plane (see fig. 2.2). Accordingly, a birdcage resonator can be used as a transmit and receive coil in conventional MR scanners with a B_0 field in the axial direction. To achieve a high field homogeneity in a large excitation volume, a birdcage resonator with many rungs ($N = 64$ or more) is mainly used as a transmit body coil in clinical MR systems. However, there are also applications as a receive coil for the head or extremities such as the knee.

2.3.5 Specific absorption rate

In addition to the risk of passive burns from contact with heated electronic components, the tissue is inevitably heated when the nuclear spins are excited by absorption of electromagnetic field energy from the RF transmit field. The effective heating of the tissue depends on the RF pulse and sequence parameters, as well as other factors such as the thermal regulation of the tissue or the individual. Since tissue damage can occur with heating of only a few degrees, very close monitoring of tissue temperature would be beneficial to ensure safety. Accordingly, the International Electrotechnical Commission (IEC) has established limits for the maximum allowable temperature and temperature rise [IEC, 2022]. Unfortunately, in vivo tissue temperature can only be measured invasively or indirectly. Therefore, to assess the safety of a pulse sequence, the specific absorption rate (SAR) is used, which is a measure of the absorbed energy of the B_1^+ field per unit mass and is defined as follows [Collins et al., 1998]:

$$SAR = \frac{1}{V} \int \frac{\sigma \cdot (|E_x|^2 + |E_y|^2 + |E_z|^2)}{2\rho} dV \tag{2.50}$$

The specific absorption rate depends on the electrical conductivity (σ) and the density (ρ) of the tissue as well as on the electric field component (E_x, E_y, E_z) of the transmit field. According to the IEC regulations, the average SAR in the human body is limited to avoid a critical temperature rise in the tissues. Depending on the body region and the safety level, there are different limits, which can be found in table 2.1.

Table 2.1: SAR limits for volume transmit coils from the IEC. The SAR limit for a part of the body can be calculated from the ratio m_{ratio} of the mass for that part of the body ($m_{partial}$) and the total mass of the body (m_{whole}). The SAR limits define the upper limit of the average SAR within a 6 min interval.

Operating mode	**Whole body** $[\frac{\mathbf{W}}{\mathbf{kg}}]$	**Partial body** $[\frac{\mathbf{W}}{\mathbf{kg}}]$	**Head** $[\frac{\mathbf{W}}{\mathbf{kg}}]$
Normal	2	$10 - 8 \cdot m_{ratio}$	3.2
First level	4	$10 - 6 \cdot m_{ratio}$	3.2

For whole body SAR monitoring, a supervision of the accepted power (forward minus reflected power) is sufficient. However, the partial body SAR limit is influenced by the mass and tissue distribution of the corresponding body part. Therefore, accurate electromagnetic field simulations with realistic voxel models are required to obtain a reliable safety assessment. In the quasi-static regime up to about 80 MHz

[Fiedler et al., 2018] the specific absorption rate increases with the B_0 field, the flip angle α and the bandwidth Δf of the RF pulse as follows:

$$SAR \propto B_0^a \alpha^2 \Delta f \qquad \text{with} \qquad a = 2 \tag{2.51}$$

At RF frequencies above 80 MHz, a dependence of $SAR \propto B_0^a$ with a less than a quadratic increase ($a < 2$) with the magnetic field has been demonstrated. However, RF field interference in the body is more pronounced at shorter wavelengths, leading to local SAR hotspots and tissue heating that must be considered to ensure patient safety [Fiedler et al., 2018]. For volume coils in MR scanners with a B_0 field of 3 T or less, consideration of the whole body SAR is sufficient to assess patient safety.

2.3.6 Signal-to-noise ratio

In general, the quality of an MR image depends on the image contrast and the signal-to-noise ratio (SNR):

$$SNR = \frac{signal}{noise} \tag{2.52}$$

Accordingly, the SNR is considered an important measure of the imaging quality of a receive coil, since it characterizes both the sensitivity and the noise of an imaging coil. The sensitivity is determined by the receive field and the magnetization of the nuclear spins [Haacke et al., 2014]:

$$signal \propto \frac{\partial}{\partial t} \iiint \vec{M} \vec{B}_1^- dxdydz \tag{2.53}$$

The noise of an RF coil can be described by the coil temperature T, the bandwidth Δf and the Boltzman constant k:

$$noise \propto \sqrt{4kT\Delta f R_{eff}} \tag{2.54}$$

The effective resistance R_{eff} is the sum of all resistances that contribute to the noise level in the final image, including the resistance of electronic components $R_{electronics}$ such as capacitors, inductors, resistors, diodes and the preamplifier or cables R_{cable}:

$$R_{eff} = R_{coil} + R_{sample} + R_{electronics} + R_{cable} + R_{radiation} \tag{2.55}$$

R_{coil} and $R_{radiation}$ describe the power losses associated with the conductor and the radiated power in the far field of the transmit coil, respectively. Due to the

large sample volumes in clinical MRI, R_{eff} is usually dominated by the sample losses R_{sample}. For small coils, such as those found in small animal scanners or NMR spectroscopy, the coil losses may dominate, and cooling of the coil would contribute to a substantial improvement in SNR. In addition, the SNR increases at least linearly with the radiofrequency, resulting in improved image quality at higher static magnetic field strengths [Platt et al., 2021]:

$$SNR \propto \omega_L^a \qquad \text{with} \qquad a \geq 1 \tag{2.56}$$

2.3.7 Tuning & matching

To tune an RF coil to the Larmor frequency ω_r of the nuclear spins, the inductors or capacitors must be chosen so that the resonance frequency is equal to the Larmor frequency ($\omega_r = \omega_L$). For a series RLC circuit consisting of an inductor L, a capacitor C and a resistor R (see fig. 2.7), the resonance condition is as follows:

$$\omega_r = \frac{1}{\sqrt{LC}} \tag{2.57}$$

Since the inductance of a coil is largely determined by the conductor geometry and size, the resonance frequency can be adjusted by the capacitor values on the conductor.
In addition, each RF coil is connected to the MR scanner by one or more cables to transmit the corresponding RF pulse or to receive the MR signal. Therefore, the RF coils must be matched to the source impedance of the MR scanner to avoid power loss at the connection. A common standard for the source impedance is $Z_{scanner} = 50\,\Omega + 0\,\mathrm{j}\Omega$, where j denotes the imaginary number.
For a series RLC circuit, with the impedances $Z_R = R$, $Z_C = \frac{1}{j\omega C}$, $Z_L = j\omega L$, the input impedance Z_{RLC} can be calculated as follows:

$$\frac{1}{Z_{RLC}} = \frac{1}{Z_C} + \frac{1}{Z_R + Z_L} \tag{2.58}$$

For optimal power transfer, the total input impedance (Z_{total}) of the coil matching network, with its real part (effective resistance) and its imaginary part (reactance), should match the conjugate source impedance of the MR scanner:

$$\mathrm{Re}(Z_{total}) = \mathrm{Re}(Z_{scanner}) = 50\,\Omega \tag{2.59}$$
$$\mathrm{Im}(Z_{total}) = \mathrm{Im}(Z_{scanner})^* = 0\,\mathrm{j}\Omega \tag{2.60}$$

While the real part of the coil's impedance can be adjusted via a parallel capacitor, a matching network (see fig. 2.7) with a series inductance or capacitance (X_{serial}) is required to balance the coil's reactance:

$$X_{serial} = \mathrm{Im}(Z_{RLC}) \tag{2.61}$$

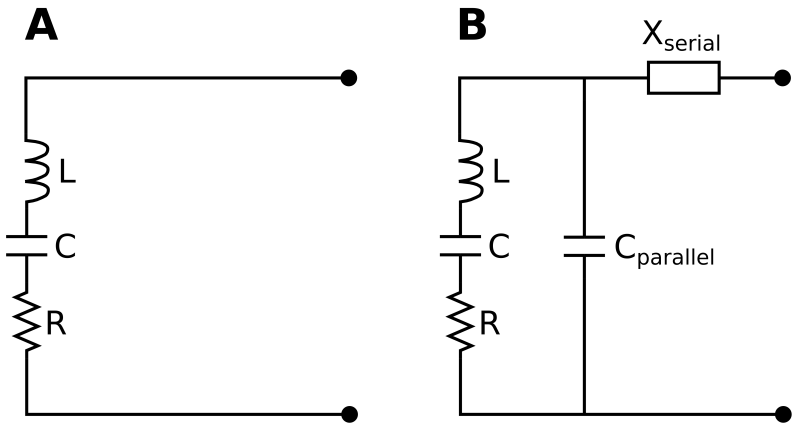

Figure 2.7: Schematic of a series RLC circuit (**A**) and a matching network for impedance matching of the RLC circuit (**B**) including a parallel capacitor ($C_{parallel}$) and a serial reactance (X_{serial}).

In practice, the tuning and matching of an RF coil can be checked with a network analyzer. The network analyzer generates an RF signal and measures the ratio S between the received power P_i at port i and the transmitted power P_j at port j [Zinke and Brunswig, 1995]:

$$S_{ij} = 10 \cdot log_{10}\left(\frac{P_i}{P_j}\right) \qquad \text{in dB} \tag{2.62}$$

The network analyzer can measure the reflected power at a single RF output (S_{11}) or the transmitted power between two different RF outputs (S_{21}). When RF power is transmitted from port 1, the S-parameter S_{11} describes the measured power at port 1 and S_{21} corresponds to the measured power at port 2.
If a coil is connected to the network analyzer via a coaxial cable, the S_{11} parameter can be used to determine the resonance frequency or the matching to the impedance of the coaxial cable. If the RF coil is off-resonant or poorly matched, almost all of the transmitted power will be reflected ($S_{11} \rightarrow 0\,\mathrm{dB}$). For good impedance matching, almost all of the power will be transmitted to the resonator and is not reflected back to the network analyzer ($S_{11} \rightarrow -\infty$ dB).
To determine the losses in an electronic device or an RF cable, the transmitted power between the RF input (port 1) and output (port 2) of the device can be

measured by the S-parameter S_{21}. For an ideal conductor, all power is transmitted ($S_{11} \rightarrow -\infty$ dB, $S_{21} \rightarrow 0$ dB) while an insulator results in a high reflection of power ($S_{11} \rightarrow 0$ dB, $S_{21} \rightarrow -\infty$ dB). Accordingly, S-parameters are used to characterize RF coils and, in particular, to determine the resonance frequency and impedance matching.

2.3.8 Quality factors of radiofrequency coils

Similar to the evaluation of receive coils based on the SNR (see section 2.52), transmit coils are evaluated based on their transmit power efficiency. If an excitation pulse of power P is applied to a transmit coil, the power efficiency can be written as $\frac{B_1^+}{\sqrt{P}}$. The transmit power efficiency can thus be used as a measure to compare the power required to achieve a given flip angle of the magnetization in the sample between different transmit coils. Transmit coils with a low transmit power efficiency require more powerful amplifiers to achieve a flip angle of 180° in a short excitation time. Furthermore, a low transmit power efficiency indicates large power losses outside the sample (see eq. 2.55).
In addition, another measure can be defined to estimate the quality of a transmit coil loaded with a lossy sample:

$$Q = \omega \cdot \frac{stored\ energy}{power\ loss} \tag{2.63}$$

The Q-factor of a transmit coil describes the fraction of the stored energy that leaves the resonator system per cycle and can also be determined experimentally from the bandwidth at half maximum $\Delta\omega_{FWHM}$ of the resonance curve with center frequency ω_r:

$$Q = \frac{\omega_r}{\Delta\omega_{FWHM}} \tag{2.64}$$

A small pickup coil consisting of two decoupled loops can be used to study the resonance behavior of an RF coil. From two measurements of the Q-factor in the loaded (Q_{loaded}) and unloaded ($Q_{unloaded}$) states of a transmit RF coil in the quasi-static regime, the absorbed power in the sample P_{sample} can be estimated as follows:

$$P_{sample} = P \cdot (1 - \frac{Q_{loaded}}{Q_{unloaded}}) \tag{2.65}$$

Due to the principle of reciprocity [Hoult, 2000], eq. 2.65 can also be used to determine if a receive coil is sample noise dominated.

2.3.9 Quadrature hybrid

To achieve quadrature driving (see section 2.1.7) for the birdcage resonator described in section 2.3.4, a quadrature hybrid can be used as a passive element.
A quadrature hybrid when driven by a single RF amplifier has four ports (two RF inputs and two RF outputs) to which RF signals can be applied via coaxial cables, assumed here to have a characteristic impedance of $Z_0 = 50\,\Omega$. When an excitation pulse is applied to the RF input of the quadrature hybrid, the pulse is split into two components of half power with a phase difference of 90° with respect to each other before leaving the two RF outputs of the quadrature hybrid. With a suitable connection to the birdcage resonator, quadrature excitation can be achieved.
In addition, a quadrature hybrid also allows quadrature reception for a birdcage coil. Due to the precessing magnetization, the detected MR signal has a phase difference of 90° between the two birdcage ports. The received MR signal from the sample is transferred from the two birdcage coil ports to the RF inputs of the quadrature hybrid. In the quadrature hybrid, RF signals with a phase difference of 90° are combined with a phase difference of 90° and forwarded to the RF output of the quadrature hybrid. A schematic diagram of the operation principle of a quadrature hybrid is shown in fig. 2.8 including the schematics with all the necessary components [Mispelter et al., 2006].

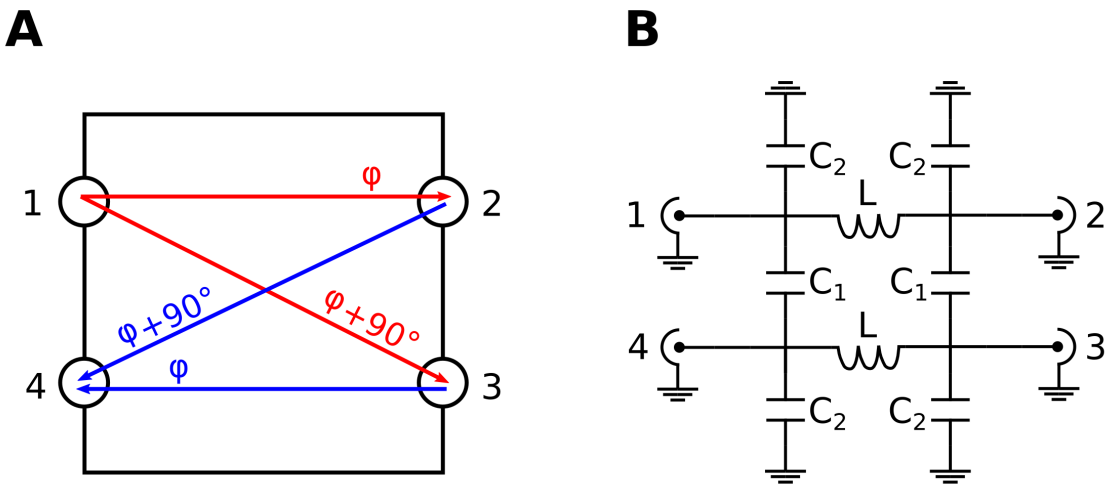

Figure 2.8: Illustration (**A**) and schematic (**B**) of a quadrature hybrid including inductors and capacitors. By adjusting the capacitance (C_1, C_2) and the inductance L, an ideal operation of the quadrature hybrid at the desired RF frequency can be achieved. In the transmit case (red), the quadrature hybrid splits the incoming RF signal (port 1) equally to the two RF outputs (port 2, port 3) with a phase difference of 90°. In the receive case (blue), incoming signals from port 2 and port 3 are combined and forwarded to port 4.

The characteristics of a quadrature hybrid are frequency dependent and determined by the built-in capacitances (C_1, C_2) and inductances (L). Proper matching of the electrical components of the quadrature hybrid is important to minimize RF power loss due to unwanted reflections at the RF inputs and outputs. The corresponding theoretical values for the components of a quadrature hybrid at $\omega = 2\pi \cdot 63.9\,\text{MHz}$ and impedance $Z_0 = 50\,\Omega$ can be found in table 2.2.

Table 2.2: Calculated inductance and capacitance values of a quadrature hybrid at 63.9 MHz using the design from fig. 2.8.

Component	Calculation	Value
C_1	$\frac{1}{\omega Z_0}$	49.8 pF
C_2	$\frac{\sqrt{2}-1}{\omega Z_0}$	20.6 pF
L	$\frac{\sqrt{2}Z_0}{2\omega}$	88.1 nH

2.3.10 Transmit/receive switch

As mentioned in section 2.3.2, transmit/receive coils require an RF switch to operate the RF coil in both transmit and receive modes. An illustration of a transmit/receive switch for RF signals is shown in fig. 2.9.

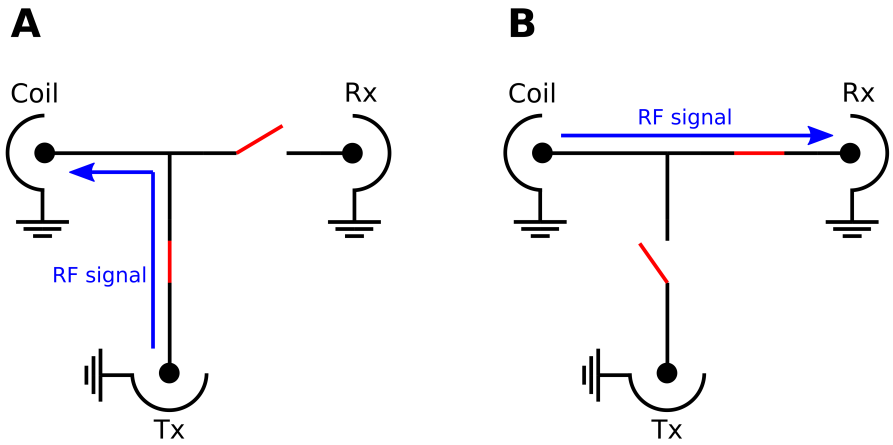

Figure 2.9: Functionality of a transmit/receive switch that separates the transmit (Tx) and receive (Rx) paths. In the case of transmission (**A**), the RF signal is transmitted from the MR system to the RF transmit coil, while in the case of reception (**B**) the MR signal is forwarded to the receive electronics.

Fig. 2.9 A shows the switch in transmit mode (Tx) in which the excitation pulse

is transmitted into the RF coil with minimum loss, but cannot pass through the receive path.

Fig. 2.9 B illustrates the receive mode (Rx) in which the MR signal induced in the RF coil is transmitted to the preamplifier, but cannot pass on the transmit path.

Good isolation between the transmit and receive paths is critical. Without protection, the sensitive preamplifier in the receive path would be destroyed by the excitation signal, which has an amplitude several orders of magnitude greater than the induced MR signal. Furthermore, losses during the transfer of the received RF signal can thus also be minimized. In addition, the switching time between the transmit and receive mode of the switch must be in the order of some tens of microseconds or faster since the MR signal decays over time. To achieve the switching between the transmit and receive mode according to the above criteria, a so-called π-element (see fig. 2.10), consisting of an inductor (L) and two identical capacitors (C) can be used as a central component in a transmit/receive (Tx/Rx) switch.

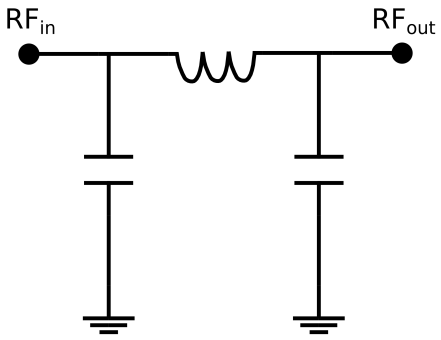

Figure 2.10: Schematic of a π-element between an RF input (RF_{in}) and an RF output (RF_{out}) consisting of an inductor and two capacitors. At a specific frequency, the π-element transforms the impedance of the transmission line ($RF_{in} \rightarrow RF_{out}$) by 90°.

In the case of transmission, RF signals on the transmission line between the RF coil and the preamplifier ($RF_{in} \rightarrow RF_{out}$) can be blocked using a π-element. If the transmission line is terminated with a short (see fig. 2.11 A), an ideal π-element transforms the input impedance of the transmission line to $Z_{in} = \infty\Omega$, effectively blocking RF signals. In the receive case, the MR signal acquired by the RF coil should pass the ideal π-element without losses. For a coaxial cable with a characteristic impedance of $Z_0 = 50\,\Omega$, this can be achieved with $Z_{in} = Z_{out} = Z_0$ thus, no further termination of the transmission line is required for ideal transfer of the RF signal (see fig. 2.11 B). Fast switching between the transmission and receive case can be realized via a PIN diode, that can either act as short or insulator. Further components such as RF chokes, direct current (DC) blocks and resistors are required to enable proper operation of the RF and DC circuit lines.

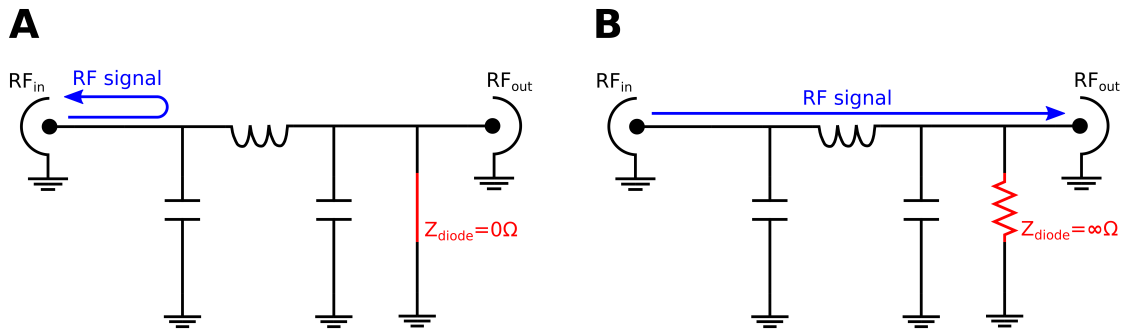

Figure 2.11: π-element between transmit and receive path with illustration of the two switching states using a PIN diode. In the transmit mode (**A**), a PIN diode is forward biased corresponding to an almost perfect conductor ($Z_{\text{diode}} \to 0\,\Omega$). The π-element transforms the input impedance to $Z_{\text{in}} \to \infty\Omega$, thus blocking RF power along the transmission line. In the receive mode (**B**), the diode is reverse-biased corresponding to an almost perfect insulator ($Z_{\text{diode}} \to \infty\Omega$). The input impedance of the transmission line is then transformed to the output impedance, which corresponds to the characteristic impedance of the transmission line ($Z_{\text{in}} = Z_{\text{out}} = Z_0 = 50\,\Omega$). This allows the RF signal to pass the π-element on the transmission line, ideally without loss.

The above properties of a π-element are only valid for a specific frequency. The corresponding capacitance and inductance values at the desired frequency of 63.9 MHz can be found in table 2.3.

Table 2.3: Calculated inductance and capacitance values of a π-element at 63.9 MHz.

Component	**Calculation**	**Value**
C	$\frac{1}{\omega Z_0}$	49.8 pF
L	$\frac{Z_0}{\omega}$	124.5 nH

2.4 Electromagnetic field simulations

This section deals with the basic principle of electromagnetic (EM) field simulations and explains the numerical consideration of Maxwell's equations. A more detailed insight into electromagnetic field simulations is given in [Taflove and Hagness, 2005]. In particular, the finite integration technique (FIT) [Weiland, 1977] can be used to tune the resonance frequency and match the impedance of custom designed RF coils with arbitrary geometry. Furthermore, realistic EM field distributions can be calculated in phantoms and even in human body models. With increasing computing power, even complex models and fine details can be rendered and approximated with a high level of accuracy in an acceptable computational time. Therefore, electromagnetic field simulations provide a versatile and powerful development tool that simplifies the coil design and development as well as the optimization process [Gurler and Ider, 2015]. In addition, the calculated RF field distribution in realistic human voxel models can be used to calculate the spatially resolved specific absorption rate (see section 2.3.5) to ensure the safety of RF coils in in vivo applications [Collins et al., 1998] [Fiedler et al., 2017].

2.4.1 Finite integration technique

The propagation of electric and magnetic fields in homogeneous and source-free media can be described by Maxwell's equations in integral form:

$$\oint_{\partial A} \boldsymbol{E} \cdot d\boldsymbol{s} = -\iint_A \frac{\partial \boldsymbol{B}}{\partial t}\, d\boldsymbol{A} \tag{2.66}$$

$$\oint_{\partial V} \boldsymbol{B} \cdot d\boldsymbol{A} = 0 \tag{2.67}$$

$$\oint_{\partial A} \boldsymbol{H} \cdot d\boldsymbol{s} = \iint_A \left(\frac{\partial \boldsymbol{D}}{\partial t} + \boldsymbol{J} \right) d\boldsymbol{A} \tag{2.68}$$

$$\oint_{\partial V} \boldsymbol{D} \cdot d\boldsymbol{A} = \iiint_V \rho\, dV \tag{2.69}$$

with line s, surface area A and volume V with arbitrary dimensions. The material equations are given by:

$$\boldsymbol{D} = \varepsilon_0 \varepsilon_r \boldsymbol{E}, \qquad \boldsymbol{B} = \mu_0 \mu_r \boldsymbol{H}, \qquad \boldsymbol{J} = \sigma \boldsymbol{E} \tag{2.70}$$

In the FIT method, the three-dimensional space is discretized into hexahedral voxels on a grid (i, j, k) and describes points with a distance of $(\Delta x, \Delta y, \Delta z)$ along the spatial coordinates [Yee, 1966]. Furthermore, the time evolution of the electromagnetic waves is calculated in time steps (n) for $n \cdot \Delta t$. In this discrete representation, the average material properties $(\varepsilon_r, \mu_r, \sigma)$ of modeled objects are assigned to each voxel.

If the voxel size is smaller than a fraction of the wavelength, the electromagnetic field does not change considerably over the volume of a single voxel. Therefore, the electric and magnetic field components can be approximated with constant values at a given time. A graphical visualization of the discretization of the electric and magnetic fields within a voxel is shown in fig. 2.12.

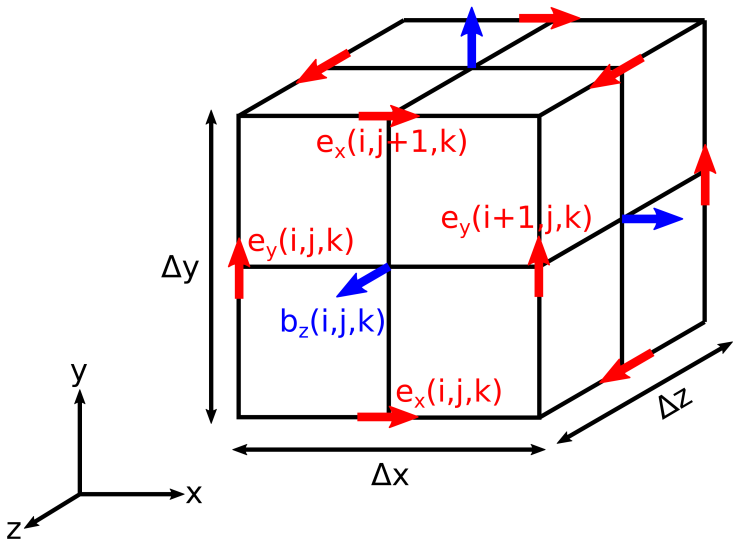

Figure 2.12: Illustration of a Yee cell representing a hexahedral voxel on a three-dimensional grid (i, j, k) with spatial coordinates (x, y, z) including electric and magnetic field components. The material properties within a single voxel are assumed to be constant, and the electric and magnetic field strengths do not vary considerably over the volume of a sufficiently small voxel. The voxel size determines the accuracy of the finite integration technique.

The exemplary electric and magnetic field components in fig. 2.12 can be described as [Clemens and Weiland, 2001]:

$$e_x(i,j,k) + e_y(i+1,j,k) - e_x(i,j+1,k) - e_y(i,j,k) = -\frac{d}{dt} b_z(i,j,k) \tag{2.71}$$

where the individual electric and magnetic field components can be calculated as follows:

$$e_x(i,j,k) = \int_{x_i,y_j,z_k}^{x_{i+1},y_j,z_k} \boldsymbol{E} \cdot d\boldsymbol{s} \tag{2.72}$$

$$b_z(i,j,k) = \int_{A_z(i,j,k)} \boldsymbol{B} \cdot d\boldsymbol{A} \tag{2.73}$$

Increasing the number of voxels or the time interval will result in a more accurate representation of the simulation model and a more accurate solution of Maxwell's equations. However, a larger number of voxels or time steps leads to longer computation times, and a trade-off between computational speed and accuracy must be made. It is recommended that the voxel size corresponds to less than one tenth of the wavelength [Taflove and Hagness, 2005]. FIT in the time domain discretizes the Maxwell equations in their integral form and is equivalent to the better known finite difference time domain (FDTD) method [Weiland, 1996]. Furthermore, FIT is characterized by fast computation time and high accuracy, especially for obtaining volumetric information of EM field distributions in heterogeneous voxel models with many mesh cells.

2.5 Particle range in matter

This section introduces the concept of cancer treatment with ionizing particle beams and describes the main differences of irradiation with protons and heavy ions compared to conventional photon therapy. A summary of particle therapy with clinical applications and a description of the underlying theoretical concepts in medical physics can be found in [Jäkel, 2009], [Schlegel et al., 2018] and [Thomson, 2013].
In conventional cancer therapy with photons, the energy of the photons is transferred to the penetrated material by the photoelectric effect, Compton scattering or pair production. In the case of protons and heavy charged particles, the energy is transferred via Coulomb interactions with the atoms of the material being irradiated. Both types of ionizing radiation result in damage to the deoxyribonucleic acid (DNA) in the irradiated tissue. The applied dose D can be expressed by the mass m of the irradiated tissue type and the transferred energy E of the radiation:

$$D = -\frac{dE}{dm} \tag{2.74}$$

Since the biological effect depends on the type of radiation and the tissue, some tumors can be controlled better with particle therapy than with conventional radiotherapy using photons. To distinguish between different types of radiation, the relative biological effectiveness (RBE) was introduced, which describes the dose required for ion beams (D_{ion}) to achieve the same biological effect as with photon radiation (D_x):

$$RBE = \frac{D_x}{D_{ion}} \tag{2.75}$$

In clinical use, protons are assumed to have a constant RBE of 1.1, while the RBE of carbon ions can range from 2 to 4 and must be adapted for each treatment plan [Schlegel et al., 2018].

2.5.1 Ionization chamber

The dose of ionizing radiation can be measured in ionization chambers. An ionization chamber consists of a gas-filled chamber, two conductors, a cathode and an anode, to which a DC voltage is applied. When ionizing radiation enters the chamber, the interaction of the radiation with the gas molecules results in the creation of ions and electrons. The applied electric field causes the electrons to migrate to the anode, resulting in a detectable current. To prevent recombination of ions and electrons and to ensure detection of ionization events, the voltage between the cathode and anode should be $50-300\,\mathrm{V}$ [Schlegel et al., 2018]. By measuring the dose in a material at different penetration depths, e.g. with a movable ionization chamber, it is possible to obtain the corresponding depth-dose curve.

2.5.2 Stopping power

The energy loss E of a charged particle along a path x depends on the properties of the penetrated material and can be expressed in terms of the stopping power of the material:

$$S = -\frac{dE}{dx} \tag{2.76}$$

For cancer therapy in the human body, particle energies of up to several hundred of $\frac{\text{MeV}}{\text{u}}$ (u: unified atomic mass unit) are required for proton and carbon ions to reach a penetration depth of several centimeters. In this energy range, the stopping power is mainly dominated by the Coulomb interactions with the electrons of the material. Thus, the stopping power for a particle with charge $q = z \cdot e$ and velocity $v = \beta c$, given the electric charge of an electron e, the number of electrons removed from the ion z (charge number), and the particle velocity as a fraction of the speed of light β, can be approximated by the Bethe-Bloch equation [Bloch, 1933]:

$$S \approx \frac{4\pi\hbar^2\alpha^2 n z^2}{m_e\beta^2} \cdot \left(\ln\left[\frac{2m_e c^2\beta^2}{I_E \cdot (1-\beta^2)}\right] - \beta^2\right) \tag{2.77}$$

Here m_e denotes the electron mass and $\hbar$ corresponds to the Planck constant, while the fine structure constant $\alpha = \frac{e^2}{4\pi\varepsilon_0\hbar c} \approx \frac{1}{137}$, with the dielectric constant ε_0, represents the coupling strength of the electromagnetic interaction. For any material with atomic number Z and mass number A, the electron density is given by

$$n = \frac{Z \cdot \rho}{A \cdot m_u} \tag{2.78}$$

with atomic mass m_u. The effective ionization potential averaged over all atomic electrons can be approximated by:

$$I_E \approx 10 \text{ eV} \cdot Z \tag{2.79}$$

Since the ratio $\frac{Z}{A}$ remains approximately constant for all elements, the stopping power depends primarily on the density ρ of the penetrated material.
The attenuation an ion beam experiences when penetrating a material depends on both the distance traveled in the object (d_{object}) and the stopping power (S_{object}) of the material. To better compare the ion attenuation of different objects, the distance traveled in an object is often expressed as the thickness of a water column, that would result in the same ion attenuation.
For materials with a homogeneous stopping power, the water equivalent thickness (WET) can be calculated using the stopping power of water S_{water}:

$$WET_{object} = \frac{S_{object}}{S_{water}} \cdot d_{object} \tag{2.80}$$

2.5.3 Bragg peak

When charged particles penetrate matter, the energy of the particles decreases with the distance traveled. However, at lower particle energies ($S \propto \frac{1}{\beta^2}$), the energy transfer to the penetrated material increases. Thus, the maximum energy is close to the final penetration depth, resulting in a sharp peak (Bragg peak) in the dose distribution (Bragg curve) at the end of the particle range.
To achieve different penetration depths, the position of the maximum dose can be adjusted by the energy of the accelerated ions. Combined with raster beam scanning in the lateral directions, the entire volume of a tumor can be irradiated by a spread-out Bragg peak.
Since the dose prior to the Bragg peak is small and the Bragg peak is locally confined to a small volume, the healthy tissue can be spared better with ion beams than with photon beams. In addition, particle beams, especially heavy ions, are less affected by lateral scattering effects [Ebert et al., 2019], which further increases the precision of the planned dose and improves tumor control and sparing of organs at risk (OAR). Moreover, particle beams, especially heavy ions, have a higher potential to generate secondary particles, resulting in greater damage to DNA (see eq. 2.75). This increased biological effectiveness compared to photons is advantageous for the treatment of radiation-resistant tumors, such as hypoxic tumors [Gérard et al., 2019] [Tinganelli et al., 2015].
In general, the success of particle therapy depends strongly on the precision of the applied ion range due to the locality of the Bragg peak. Therefore, attenuating materials in the irradiation field should be well known or even avoided as they may reduce the ion range and affect the resulting dose distribution.

Chapter 3

Methods

This chapter describes the experimental setups and the RF coils and electronic components developed. The designs and the development process in the simulations and with the real setups are discussed. Furthermore, the different MR measurements with the developed RF coils are described and the corresponding evaluation methods are explained.

3.1 MR systems

This section introduces the MR systems used for the measurements in this thesis. This includes the general structure and the existing interfaces for additional hardware such as RF coils as well as conditions regarding the application in combination with particle therapy. RF coils have been designed and built for two different MR systems. Although both MR systems are located in an ion therapy center, a distinction is made between an "offline" MR system without direct beam access and an "online" MR system connected to the beam line of an ion accelerator.

3.1.1 "Offline" 1.5 T MR system

The "offline" MR system is a 1.5 T MR system (MAGNETOM Sola, Siemens Healthineers AG, Erlangen, Germany), which can be used for whole body imaging (see fig. 3.1). Accordingly, all MR measurements with the designed RF body coil (section 3.2.1) were performed on this scanner. The superconducting coil of the closed-bore MR scanner achieves a magnetic field strength of about 1.5 T oriented along the negative Z axis, which corresponds to a Larmor frequency of 63.68 MHz (eq. 2.12) for hydrogen nuclei.

Figure 3.1: Whole-body closed-bore MR system with a static magnetic field of 1.5 T. The magnetic field B_0 is oriented in the negative direction along the Z axis of the MR system. A height-adjustable patient table can be detached from the MR system and used as a mobile patient shuttle.

The following technical specifications of the MR system are taken from the MR scanner user manual [Siemens, 2020]:

With a bore opening diameter of 70 cm and a distance of 1.57 m from one bore opening to the other, the MR system can be used for whole body imaging. The gradient fields along the X, Y, and Z axes reach a maximum field strength of $33\frac{mT}{m}$ with a maximum slew rate of $125\frac{T}{m \cdot s}$. The gradient fields remain linear along each axis in a range up to $\approx \pm$ 20 cm from the isocenter, resulting in a viable FOV for imaging of $\approx$ 40 cm in each direction. The maximum peak power of the transmitter amplifier is 29.2 kW.

The patient table (see fig. 3.1) has additional slots for connecting transmit and receive coils to the MR system. For custom-built RF coils, an adapter (called Tim Coil Interface, see fig. 3.2) is also required between the coil connector and the patient table to allow access to the transmit and receive channels.

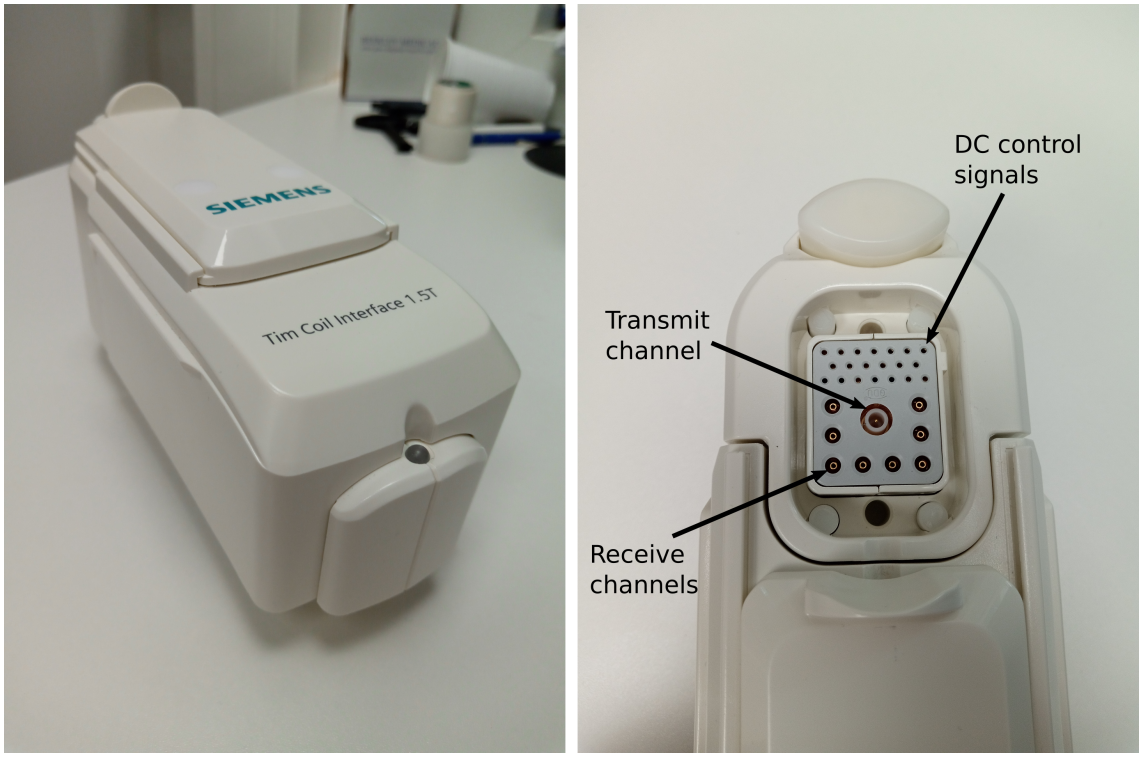

Figure 3.2: The Tim Coil Interface adapter is required to connect custom RF coils to the coil socket of the "offline" 1.5 T MR system. The adapter provides one transmit channel, up to 8 receive, and multiple DC signals for powering or controlling active electronics such as a transmit/receive switch (see section 2.3.10) and for encoding the coil.

In addition, the Tim Coil Interface adapter is also used to transmit DC signals from the MR system, which can be used both for coil identification and to control active electronics such as diodes. Information about the operation of the transmit and receive signals and the DC signals of a coil can be defined in a coil file. Each coil can be recognized by the coil identifier, a specific resistance on a DC signal line, and assigned to the appropriate coil file. In addition to powering preamplifiers, a transmit/receive switch can also be controlled via DC signals in order to separate the transmit and receive paths of transceiver coils. The MR system can drive the diodes with DC voltage in either forward or reverse bias, thus changing the characteristics of the transmit or receive path (see section 3.3.1).
The patient table can be detached from the MR system and is suitable for patient transport. This allows the patient to be positioned on the mobile patient table outside of the scanner room and then transported to the MR system.

3.1.2 "Online" 0.25 T MR system

The "online" MR system is a 0.25 T C-shaped magnet (S-Scan, Esaote, Genoa, Italy), which can be used e.g., for limb imaging (see fig. 3.3). All MR measurements with the developed RF calf coil (see section 3.2.1) were performed with this MR system. The magnetic field is generated by a C-shaped permanent magnet and reaches a field strength of 0.25 T, which corresponds to a Larmor frequency of 10.25 MHz (see eq. 2.12) for hydrogen nuclei.

Figure 3.3: C-shaped permanent magnet (left) with a magnetic field strength of 0.25 T, oriented in the negative Z direction. The MR system is surrounded by an RF cabin (right), which shields the MR scanner from RF noise and provides access to a particle accelerator through an irradiation window.

The following technical specifications of the MR system are taken from the MR scanner user manual [Esaote, 2019]:
Magnetic field stability in a maximum FOV of 270 mm in each direction is achieved by thermal control of the magnet with five individual heating channels. The gradient fields reach a maximum intensity of $20\frac{mT}{m}$ with a slew rate of $25\frac{T}{m \cdot s}$ and can be considered linear in a region of $\approx \pm 20$ cm from the isocenter, corresponding to ≈ 40 cm in each direction. The integrated transmit coil is based on two linearly-polarized surface loops and can be operated with two RF power amplifiers of up to 1500 W each, resulting in a transmit field of $B_{1,rms} = 5.16\,\mu T$. The MR system

interface for imaging coils is limited to receive-only coils that can be connected via a connector.
The MR system has a size of approximately 159 cm×100 cm×177 cm in the X, Y, and Z directions and is located in an ion acceleration facility (see section 3.5.1) in order to investigate effects between particle beams and MR imaging that are relevant for MR-guided radiotherapy. For this purpose, the MR system and the RF cabin have been mounted on rails to allow positioning in front of the beam exit.

3.2 Developed radiofrequency coils

In the scope of this thesis, an RF coil was developed for each of the two MR systems with a special focus on the compatibility of the RF coils with MR-guided particle therapy. In this section, the developed imaging coils for the "offline" and "online" MR systems, including the corresponding simulation models and the phantoms used in this work, are presented. Both the structure of the RF coils and the rotation systems for flexible coil and patient positioning are discussed. Furthermore, the coil tuning and matching process as well as the coil characteristics in transmit and receive mode are investigated.

3.2.1 Concept & design

For RF coils to be used in MR-guided particle therapy, special requirements must be met:

- The influence of the coil components on the radiation must be minimized so as not to affect the quality of the treatment. Particle beams are particularly sensitive to the materials in the beam path (see section 2.5.3).
- Ideally, the patient can be irradiated from multiple directions in order to make the treatment as flexible as possible. Therefore, a large irradiation window of the developed coils is desired.
- Homogeneous transmit and receive fields as well as sufficient image quality with preferably high signal-to-noise ratio (SNR) are advantageous to enable classification of different tissues and differentiation from tumor tissue.
- Patient safety must be considered in terms of specific absorption rate and coil coupling.

Due to the different magnet designs, two different types of RF coil types were developed in this thesis:
An RF transmit/receive body coil for imaging the entire torso was designed for the "offline" MR system, and a receive-only RF calf coil for imaging of the leg and other extremities was designed for the "online" MR system.

RF body coil

A cylindrical birdcage resonator [Tropp, 1989][Hayes et al., 1985] was developed as the RF body coil for the "offline" MR system in order to achieve a high degree of homogeneity of the B_1 field distribution in a large FOV. The RF body coil measures 52 cm in the axial (Z) direction and has a diameter of 53 cm, allowing complete coverage of the human torso. The coil consists of two end rings, that are electrically connected to 16 equidistant rungs of the conductor. To tune the RF body coil to the appropriate Larmor frequency, capacitors are placed at 16 positions on each of the two end rings between the rungs (in total: 32 capacitors). This arrangement of the capacitors corresponds to the high-pass configuration of the birdcage resonator (see section 2.3.4) and is particularly suitable in combination with sensitive particle beams, since additional ion damping and scattering by capacitors can be avoided over a large part of the RF body coil between the end rings (see fig. 3.4) and patient irradiation can be achieved with lateral beam access. In addition, the RF body coil is designed to allow rotation of the entire assembly, including the patient, around the longitudinal (z) axis of the coil. This increases the flexibility of the treatment plan by facilitating beam access from different angles. Furthermore, rotation of the patient allows irradiation from multiple angles even with a fixed ion beam source, eliminating the need for a complex and costly ion gantry.

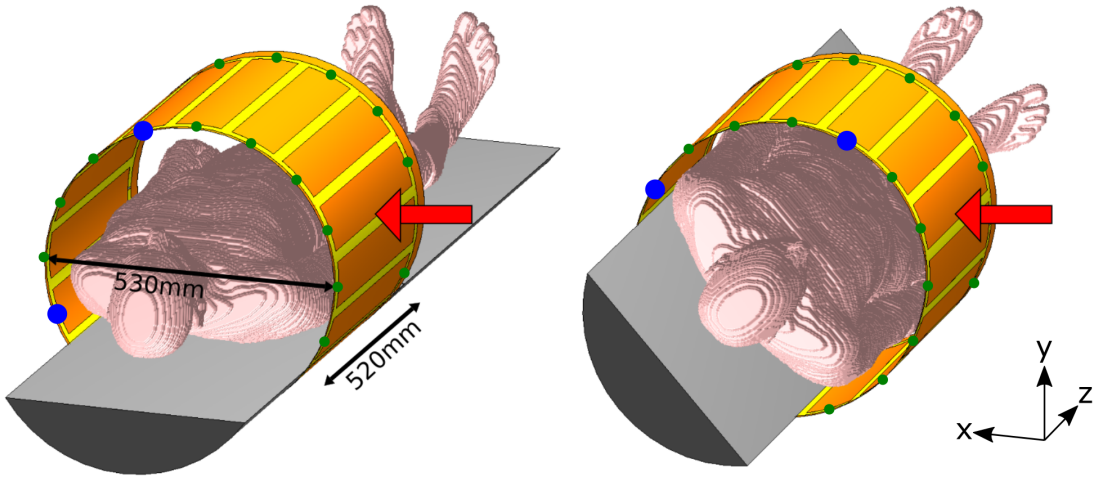

Figure 3.4: 3D model of the RF body coil with a human voxel model on a custom pad (gray) to simulate realistic patient loading (voxel model (CST Studio Suite 2021): Gustav, 38 years, 176 cm, 79 kg, male). Due to the high-pass birdcage configuration of the RF body coil, all tuning capacitors (green circles) and the two matching networks (blue circles) are located at the end rings. Thus, a potential particle beam (red) is not affected by electronic components in a large window between the two end rings. The human voxel model is shown in the feet-first position along the z axis of the RF coil's coordinate system (x, y, z). The rotation of the RF body coil and the patient, allows flexible multi-angle radiotherapy with a static particle beam from a single direction.

In addition, the RF body coil can operate as both a transmit and receive coil, eliminating the need for additional RF surface coils for signal acquisition. As a result, additional components in the beam path can be avoided in order to maintain the quality of the particle beam. To operate the RF body coil as a transmit/receive coil, a transmit/receive switch is required to separate the transmit path from the receive path and protect the sensitive receive electronics, such as the preamplifier, from the high RF power of the excitation pulse. The functionality of the developed transmit/receive switch is explained in detail in section 3.3.1.

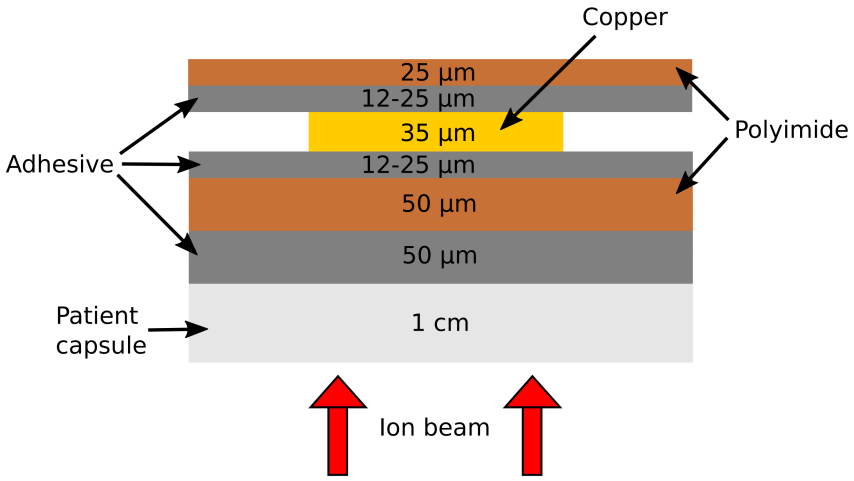

Figure 3.5: Cross-sectional view of the structure of the developed RF coils. In particular, the individual layers of the printed circuit board are shown, including their respective thicknesses. A potential ion beam (red) penetrates the homogeneously distributed layers, while the conductor (copper) is only penetrated at certain positions.

The presented RF body coil operates as a single-channel transmit/receive coil. In order to achieve higher transmit power efficiency and better imaging quality, circularly-polarized excitation and detection (see section 2.1.7) was realized for the RF body coil. For this purpose, a quadrature hybrid was used as a passive component to provide quadrature excitation and detection. The functionality of the quadrature hybrid is described in detail in section 3.3.2.
In fig. 3.4 it is shown that the RF body coil is connected to the quadrature hybrid at two locations. A matching network is required for each of these ports to match the impedance of the RF coil to the transmission lines ($Z = 50\,\Omega$) and the scanner's source impedance (see section 2.3.7). The tuning and matching process is discussed in detail in section 3.2.5.
A flexible printed circuit board (PCB) was designed with the goal of a minimal WET for optimal radiation transparency of the RF body coil. Limited by manufacturer's specifications, the flexible PCB was divided into four equal segments and attached to the inside surface of a patient capsule with an acrylic-based adhesive, where the segments were electrically connected to capacitors. The flexible PCB is attached

directly to the patient capsule, eliminating the need for a rigid housing. In addition, the RF body coil was designed without an RF shield, thus further increasing the radiation transparency of the RF body coil.
The layered structure of the flexible PCB is shown in fig. 3.5. The materials of the flexible PCB consist of a flat copper conductor with a thickness of 35 µm and a width of 2 cm, which is embedded between two layers of polyimide and acrylic based adhesive. The patient capsule corresponds to a polymethylmethacrylate (PMMA) cylinder with a thickness of 1 cm and an inner diameter of 53 cm in the x and y directions. A potential particle beam would penetrate the patient capsule and the individual layers of the flexible circuit board, which can lead to ion attenuation and thus affect the treatment plan. While the WET of homogeneously distributed layers can be corrected with higher beam energy, inhomogeneous layers such as the conductive layer pose a greater challenge.
However, a conductor layer that is too thin can lead to losses in the acquisition of the MR signal and thus in a reduction of the SNR in the image [Barta et al., 2021]. A measure of the absorption of an RF signal of frequency ω in an electrical conductor of resistivity ρ and permeability μ is given by the skin depth [Giovannetti et al., 2023]:

$$\delta = \sqrt{\frac{2\rho}{\omega\mu}} \tag{3.1}$$

For copper, the skin depth for alternating currents at a radiofrequency of $\omega = 2\pi{\cdot}63.68\,\text{MHz}$ corresponds to $\approx 8\,\mu\text{m}$. The conductive layer of the RF body coil with a thickness of 35 µm corresponds to approximately four skin depths and is therefore sufficient to absorb most of the RF power without considerable SNR loss in the image.
In terms of patient safety, the high dielectric strength of the polyimide films of over $600\frac{V}{\mu m}$ [Diaham et al., 2020] provides sufficient electrical insulation between the patient and the conductor.
The layered structure of the RF body coil shows an uncertainty in the manufacturer's specification for the thickness of the adhesive layers between 12 µm and 25 µm, which further complicates the assessment of the RF body coil's radiation transparency. Therefore, the influence of the flexible PCB on the range of the particle beam was investigated (see section 3.5).
In addition, tolerances in the manufacturing process of the patient capsule could result in a spatially varying wall thickness, leading to uneven WET across the irradiation window, which could affect the treatment quality. The wall thickness tolerance was specified as ± 1 mm (Thyssenkrupp AG, Essen, Germany). To estimate the radiation transparency of the patient capsule, the wall thickness was measured at 16 evenly spaced positions distributed over a full rotation. Each measurement at a position consists of 10 individual measurements to provide a more accurate value for the average wall thickness as well as for variations between individual measurements.

RF calf coil

A solenoid coil design was chosen for the RF calf coil (see section 2.3.3).
Since the B_1^- field for receiving the MR signal must be orthogonal to the static B_0 field, the design of a birdcage is impractical for the "online" MR system. Due to the special orientation of the static magnetic field in the vertical direction (cf. fig. 3.3), a solenoid design was chosen for the RF calf coil.
The single-channel receive-only coil consists of four turns of a copper conductor and a connection between the two outer turns. Although solenoid coils generally have a high B_1 field homogeneity, a finite length inevitably leads to inhomogeneities towards the coil ends. To compensate for this effect, the B_1 field homogeneity of a solenoid coil can be considerably improved by increasing the turn density per length at the RF coil ends [Leifer, 1993]. Therefore, the turns of the RF calf coil have different pitch angles, resulting in different distances between two adjacent turns (see fig. 3.6).

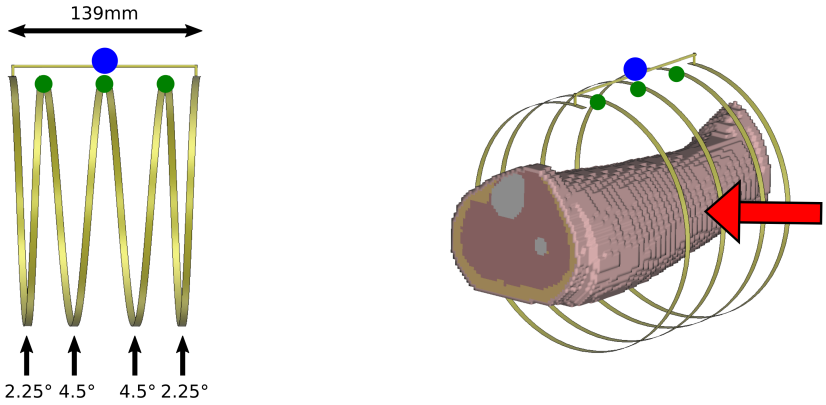

Figure 3.6: 3D model of the developed RF calf coil including the three positions for the tuning capacitors (green) and the matching network (blue) where the RF coil is connected to the scanner via a coaxial cable. The specified pitch angles between the individual turns of the RF calf coil increase the homogeneity of the receive sensitivity profile especially towards the coil openings. A potential particle beam (red) for irradiating a calf through the developed RF coil is shown.

A pitch angle of 4.5° was chosen for the inner two turns and a pitch angle of 2.25° for the outer two turns.
The RF calf coil was designed on a flexible PCB with the same layered structure as the RF body coil of the "offline" MR system (see fig. 3.5). However, the flexible PCB of the RF calf coil was attached to the outer surface of a PMMA cylinder. The PMMA cylinder has a length of 18 cm with an outside diameter of 18 cm and a wall thickness of 4 mm. Due to the smaller dimensions of the RF calf coil, the coil could be constructed from a single flexible PCB. The flexible PCB covers a total

axial length of 15 cm, leaving enough space at the ends of the PMMA cylinder for a support system that allows the RF calf coil to rotate (see section 3.2.2).
To homogenize the current distribution along the conductor, the resonance frequency of the RF calf coil was tuned with capacitors distributed along a line (see fig. 3.6), thus resulting in the largest possible area without capacitors for irradiation with a particle beam.
Furthermore, the skin depth of electromagnetic radiation in copper is given by $\approx 20\,\mu m$ at a frequency of 10.25 MHz. A thickness of 35 µm corresponds to about two skin depths. Thus, small losses in the MR signal acquisition are possible, however, a larger conductor thickness would lead to an increased WET of the conductor. In addition, a larger conductor thickness could lead to a stronger shielding of the object to be examined from the transmit field of the internal coil in the "online" MR system and thus reduce the flip angle of the magnetization or affect the homogeneity of the transmit field. Since the "online" MR system only allows the connection of receive-only coils, the RF calf coil must be off-resonant during the transmission of the excitation pulse from the internal transmit coil of the MR scanner. A detuning of the resonance frequency can be achieved with passive diodes, which is discussed in more detail in section 3.2.5. In addition, a fast-acting fuse (0464.500DR, Littlefuse, USA) with a resistance of 237 mΩ was installed in series at the end of an outer turn in order to detune the RF calf coil in the event of excessive current flow and to protect the examined subject.
Imaging with the RF calf coil also required the development of a preamplifier to amplify the MR signal received from the RF coil. In particular, a low noise figure of the preamplifier is advantageous to achieve a maximum SNR in the signal acquisition. The schematic structure and design of the preamplifier is described in more detail in section 3.3.3.
Similar to the patient capsule of the RF body coil, the wall thickness of the PMMA cylinder of the RF calf coil was measured at 20 different positions to assess the radiation transparency of the entire setup.

3.2.2 Setup

The main features of the measurement setup for the two MR systems and the patient positioning systems of the developed RF coils are described below.

RF body coil setup

A schematic representation of the measurement setup of the RF body coil is shown in fig. 3.7.

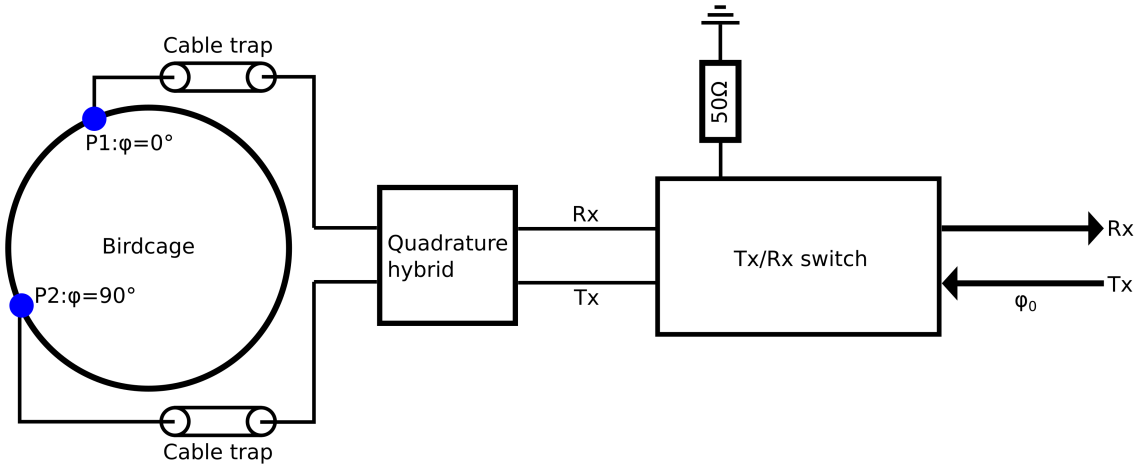

Figure 3.7: Schematic structure of the transmit and receive chain for the developed RF body coil. The transmit pulse (Tx) passes through the transmit/receive switch (Tx/Rx switch) and is split into two signal components in the quadrature hybrid and fed into two ports (blue) of the birdcage resonator to achieve quadrature excitation. Similarly, the two receive signals (Rx) are combined in the quadrature hybrid before being amplified in the preamplifier located on the Tx/Rx switch and passed to the MR system. A 50 Ω termination absorbs power that is reflected to the sensitive receive electronics during transmission. Cable traps suppress RF losses on the outer conductor of the coaxial cables.

The transmit/receive switch is connected to the MR system via the adapter (Tim Coil Interface, fig. 3.2), allowing either transmission of the RF pulse to the RF body coil or reception of the MR signal to the MR system. Coaxial cables (K-02252-D-08, Huber & Suhner) connect the transmit/receive switch to the quadrature hybrid, which splits the signal line for the two coil ports. Inductively coupled cable traps [Seeber et al., 2004] in front of each coil port suppress RF currents on the outer conductor of the coaxial cable and facilitate the process of tuning and matching of the RF body coil. The two ports are located on the same ring of the birdcage resonator, but the position is offset by a quarter circle (see fig. 3.7). The patient capsule, including the RF body coil, is mounted on a two-part wooden table (upper and lower) with rollers (see fig. 3.8) that allow full rotation of the object of investigation (phantom, human).

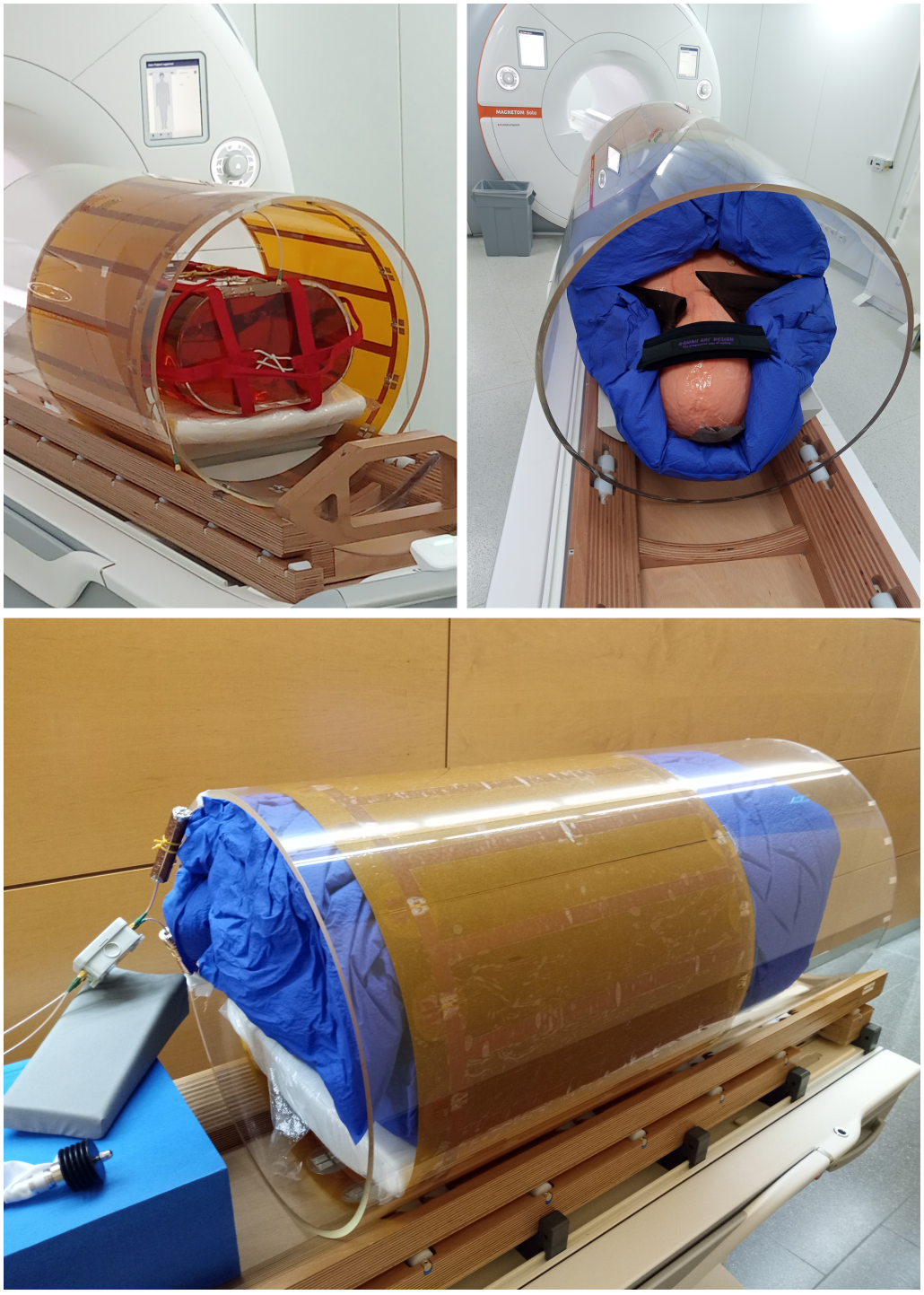

Figure 3.8: Measurement setup of the RF body coil at the "offline" 1.5 T MR system. The RF body coil is attached to a PMMA patient capsule and can be rotated on a wooden table. To demonstrate torso imaging at different rotation angles for MR-guided radiotherapy, a homogeneous phantom or heterogeneous anthropomorphic phantom (see section 3.2.3) was positioned and fixed using vacuum mattresses.

The upper part of the wooden table can be moved into the bore of the "offline" MR system to allow stable positioning of the patient capsule. For measurements at the desired angle of rotation, the patient capsule was locked and positioned on the wooden table using markings indicating the angle of rotation and axial position (Z) along the magnet bore. The phantoms were placed in the center of the RF coil on top of a cushion and tailored pad with a small circle segment (width: 31 cm, height: 10 cm) made of Obomodulan 210. Vacuum mattresses are used as rigid cushions to ensure the same position of the phantom for all angles of rotation. In addition, the vacuum mattresses provide electrical insulation between the object of investigation and the RF coil and act as a spacer, allowing a minimum distance from the electrical conductor to be achieved. Further electrical insulation is provided by special 3D-printed photopolymer caps that also protect the capacitors on the RF coil end rings from mechanical stress from the vacuum mattress. The stopping power of the vacuum mattresses used is low, because the filling material (styrofoam balls) has a very low density. In addition, it can be assumed that the vacuum mattresses are filled homogeneously and that there are no major changes in the stopping power throughout the volume. Therefore, the ion beam attenuation of the vacuum mattresses is neglected in this study.

RF calf coil setup

The measurement setup of the "online" MR system including the developed RF calf coil as well as the supporting structure is shown in fig. 3.9.

The RF calf coil is connected to the developed preamplifier (see section 3.3.3) and the "online" MR system via a detachable cable. A 3D-printed semicircular holder, which is attached on a mounting plate, is used to position and fix the RF calf coil and also allows the RF coil to rotate around the longitudinal axis of the RF coil. To fix the RF coil and plate in the X and Y directions, the base plate is mounted to designated holes in the patient table. The phantom can be positioned with pads in the center of the RF calf coil, while the position of the RF calf coil along the Z-axis can be adjusted with four plastic screws in the mounting plate. For ease of positioning, the focal point of the particle beam is indicated by a laser system.

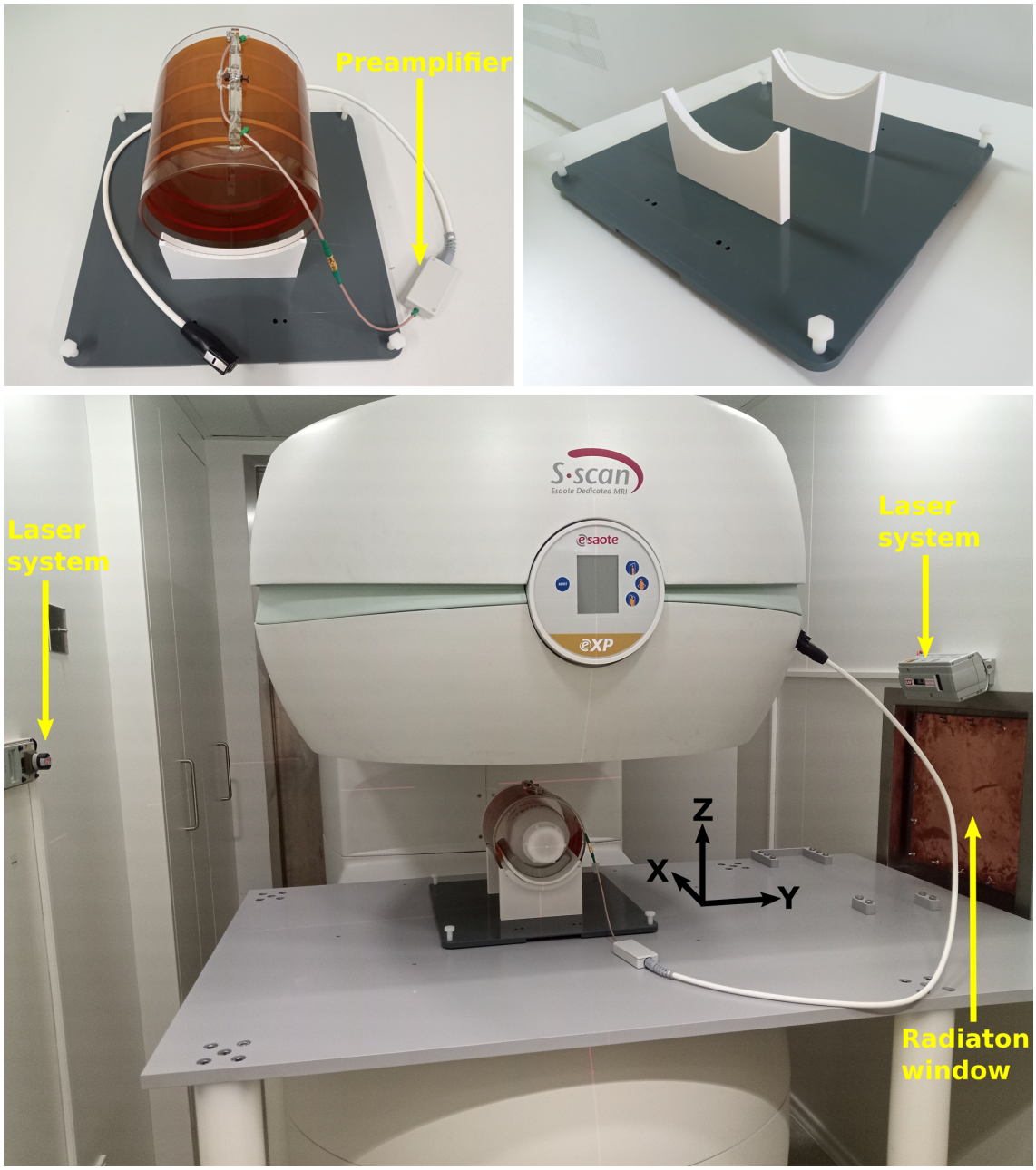

Figure 3.9: Measurement setup of the developed RF calf coil including the developed preamplifier (see section 3.3.3) and the constructed holder at the "online" 0.25 T MR system. The RF calf coil is positioned on a holder that allows rotation along the longitudinal (X) axis of the RF coil for more flexibility in possible radiation therapy. The mounting plate allows reproducible positioning of the RF coil in the isocenter. Since the holder has a square base plate, holder and RF coil can be rotated by multiples of 90°. Laser systems indicate the focal point of the particle beam.

3.2.3 Phantoms

In this thesis different phantoms have been used for MR measurements and simulations. In general, a distinction can be made between homogeneous and heterogeneous phantoms.

A large cylindrical phantom with an oval cross section (dimensions: 32 cm × 20 cm × 50 cm, volume: 40 L) was used for the MR measurements with the RF body coil at 63.9 MHz (see fig. 3.10). The phantom body is made of PMMA filled with a homogeneous tissue-simulating liquid containing water, polyvinylpyrrolidone (PVP) and sodium chloride [Platt et al., 2018]. The measured dielectric properties correspond to $\varepsilon_r = 55.5$ and $\sigma = 0.43\frac{S}{m}$ at 64 MHz. In the simulation model, the homogeneous phantom was implemented with the same dielectric properties to minimize the differences between simulations and measurements.

A cylindrical calf phantom (diameter: 11 cm, height: 20 cm, volume: 2 L) containing water and sodium chloride (mass fraction: $w_{\mathrm{NaCl}} = \frac{m_{\mathrm{NaCl}}}{m_{\mathrm{NaCl}}+m_{\mathrm{H_2O}}} = 0.23\,\%$) was prepared for the MR measurements and simulations at 10.25 MHz with the RF calf coil. The dielectric properties of the liquid ($\varepsilon_r = 80$ and $\sigma = 0.47\frac{S}{m}$ at 10.25 MHz) were measured with a dielectric assessment kit (Speag, Schmid & Partner Engineering AG, Zurich, Switzerland) and different concentrations of sodium chloride were tested to achieve the desired conductivity (m_{NaCl}: 4.78 g, $m_{\mathrm{H_2O}}$: 2073.22 g, m_{total}: 2078 g).

In addition, EM field simulations for the RF body coil and the RF calf coil were also performed with a heterogeneous human voxel model [Christ et al., 2009] (voxel model (CST Studio Suite 2021): Gustav, 38 years, 176 cm, 79 kg, male). The human voxel model (voxel size: $(2\,\mathrm{mm})^3$) contains anatomical structures (organs, muscles, bones, fat, ...) and their individual dielectric properties for the respective frequency (63.9 MHz or 10.25 MHz) [Gabriel et al., 1996][Hasgall et al., 2022]. To check the plausibility of the homogeneous phantoms, the dielectric properties of the human voxel model in the body parts inside the RF coils (torso, calf) were averaged over all voxels. Thus, the averaged real component of the complex permittivity ε_r and the electrical conductivity σ correspond to $\varepsilon_r = 47.1$ and $\sigma = 0.39\frac{S}{m}$ for the torso (including the arms) at 63.9 MHz and $\varepsilon_r = 150.6$ and $\sigma = 0.45\frac{S}{m}$ for the calf at 10.25 MHz. The homogeneous torso and calf phantoms as well as the corresponding homogeneous simulation models and the body parts of the human voxel model for the determination of the average dielectric properties are shown in fig. 3.10.

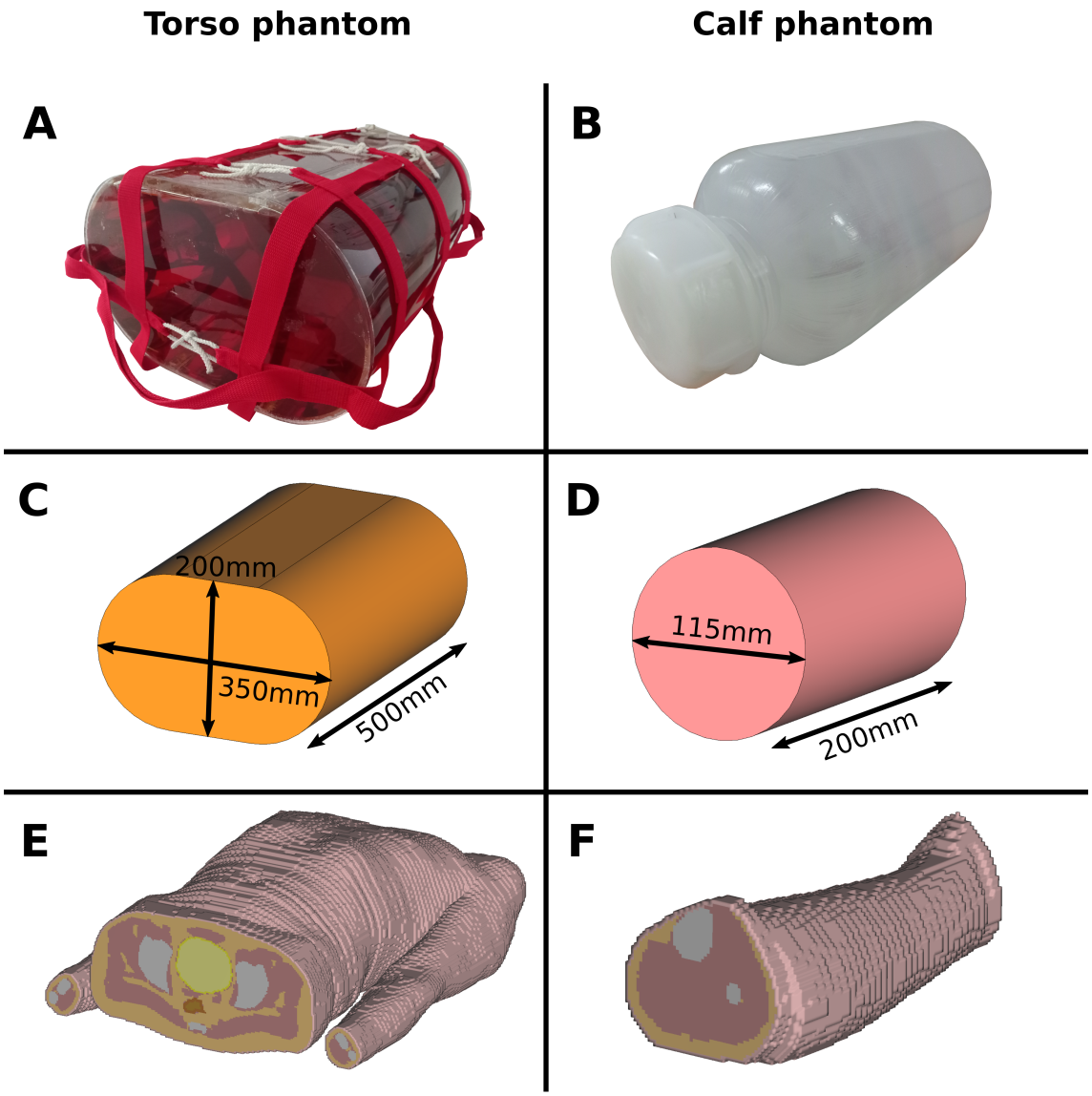

Figure 3.10: The homogeneous torso-sized phantom (**A**) and the calf-sized phantom (**B**) which were used for RF body coil and RF calf coil measurements, respectively. A model of the homogeneous phantoms with similar size, shape, and dielectric properties (ε_r, σ) was created (**C**, **D**) to simulate the RF field distributions of the developed RF coils. Realistic dielectric properties of the homogeneous phantoms were determined from the averaged dielectric properties of the different tissues in a human voxel model for body parts of similar size in the human torso (**E**) and calf (**F**).

For the EM field simulations performed with the heterogeneous human voxel model, the complete human voxel model including head and legs was implemented for the transmit/receive RF body coil (see fig. 3.4), while for simplicity, only the calf of the voxel model was implemented for the EM field simulations of the receive-only RF

calf coil (see fig. 3.6).
Furthermore, MR measurements with the RF body coil were also performed using an anthropomorphic silicone torso phantom filled with different liquids to create the image contrast of different organs (see fig. 3.11).

Figure 3.11: Torso-sized anthropomorphic phantom used for MR measurements with the RF body coil to simulate realistic patient loading. The phantom is based on a silicone-cast mannequin filled with agar and contains organ-like structures with various fluids to simulate different tissue contrasts.

3.2.4 Simulation models

To facilitate the coil development process for the RF body coil and the RF calf coil, electromagnetic field simulations were performed for both MR systems. The simulation software "CST Studio Suite 2021" (Dassault Systèmes, Vélizy-Villacoublay, France) uses a numerical approach based on the finite integration technique (FIT) [Weiland, 1977] to compute the solutions of Maxwell's equations (see section 2.4.1). In a first step, a simplified model of the measurement setup including a phantom is implemented in the simulation software. The structure of the measurement setup is represented by a hexahedral mesh (see fig. 2.12), thus providing a discrete version of the geometry for the calculation of the 3D electromagnetic field distributions. To model the setup of the two MR systems with sufficent accuracy, a hexahedral mesh of $30-50$ million cells was used for all simulations. Each hexahedral cell contains information about the material specific properties (permittivity ε_r, permeability μ_r, electrical conductivity σ and density ρ). In addition, the positions of the capacitors on the coil geometry and the connections of the RF coil to the MR system were defined as ports which enable the stimulation and the absorption of RF energy. The

RF field distributions can then be calculated for each port position. In an additional co-simulation, the capacitor values can be changed and the S-parameters of the RF coils can be calculated without having to recalculate the 3D field distributions of the first simulation step. Accordingly, the capacitor values can be adjusted and a good tuning and matching of the RF coils to the given frequency and the 50 Ω impedance of the coaxial cable can be achieved in the co-simulation. Once the optimal S-parameters have been found, the phase and the power of the RF signal and the impedance of the ports can be specified. The combination of the calculated field distributions for the individual port positions leads to the overall solution of the electromagnetic field distribution of the RF coils. The simulation models used for the 3D field calculations of the two MR systems are shown in fig. 3.12.

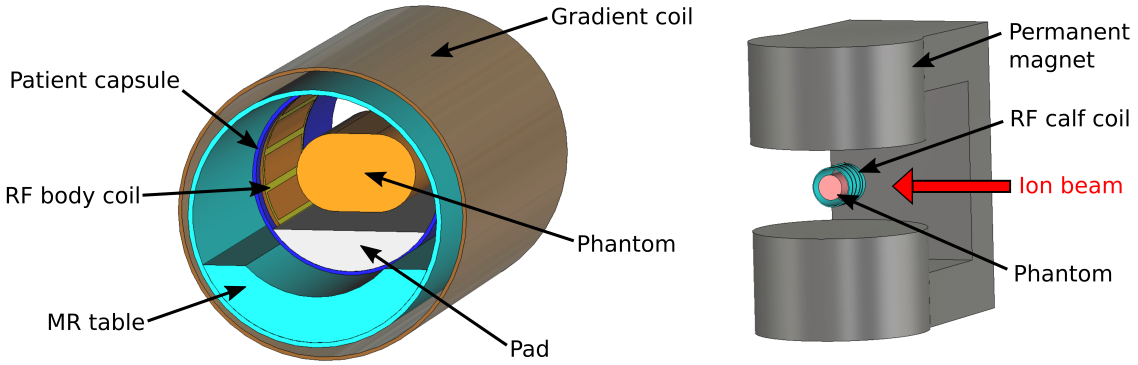

Figure 3.12: Simplified models of the "offline" 1.5 T (**A**) and "online" 0.25 T MR systems (**B**) with the components essential for the RF field calculations of the RF coils. The MR table in the bore of the "offline" 1.5 T MR system leads to an elevated (y) position of the patient capsule including the radiation-transparent RF body coil and the phantom with respect to the central Y axis of the MR scanner (y = Y + 56 mm). The gradient coil was represented by a cylinder consisting of a perfect electrical conductor. For the EM field simulations with the "online" 0.25 T MR system, a model of the developed radiation-transparent RF calf coil and the permanent magnet was used. In addition, the RF cabin (not shown in the figure) was included in the simulations as a boundary condition for the radiated RF power.

The cross section of the simulation model of the "offline" MR system shows the various components of the setup. The scanner housing and the patient table were combined as one unit with the material properties of PMMA. The gradient coil is modeled with a perfect electrical conductor (PEC). The transmit/receive body coil is attached to a rotatable patient capsule that is elevated with respect to the center of the magnet. This mismatch of the central axes of the patient capsule (x, y, z) and the magnet bore (X, Y, Z) corresponds to $\Delta y = y - Y = 56\,\text{mm}$ (x = X, z = Z). Since the RF body coil is unshielded, the effect of the mismatch of the center axes on the performance of the RF body coil is investigated in this thesis. The measured impedances at the ports of the transmit and receive network (see fig. 3.7) in the

transmit and receive case as well as the measured phase relationship between the two ports connected to the RF body coil were implemented in the simulation. For the "online" MR system, the permanent magnet has been modeled in a simplified manner neglecting the integrated transmit coil and the gradient coils. Furthermore, the RF calf coil is positioned in the center of the MR system with an orientation that allows lateral irradiation through the RF calf coil. Therefore the coordinate system of the RF calf coil (x, y, z) coincides with the coordinate system of the MR system (X, Y, Z) (cf. fig. 3.9). The RF cabin around the "online" MR system acts as a static boundary condition where the electric field is set to zero and the radiated RF power is completely absorbed.

As part of the simulations, the S-parameters for the ports of the RF body coil and the RF calf coil were calculated in steps of 15° for a full rotation (0° − 360°) of the RF coil and the homogeneous phantom. The tuning and matching capacitors were optimized for the horizontal position of the phantom (0° rotation) and assigned to all rotation angles. Thus, the influence of the rotation on the S-parameters of the RF coils can be evaluated. In addition, the transmit and receive field distributions of the RF body coil and the receive field distributions of the RF calf coil were calculated for the same rotation angles in a homogeneous phantom and a human voxel model with a stimulated power of 1 W (see section 4.2.2 and section 4.3.2). The homogeneity of the simulated transmit and receive fields of the RF body coil was then compared to the homogeneity of the measured B_1 maps.

To evaluate the safety of the transmit/receive RF body coil, the specific absorption rate was calculated in the whole human voxel model and in the body part with mass $m_{partial}$ near the RF coil where 95 % or less of the total RF power was absorbed [IEC, 2022]. In particular, the specific absorption rate for the whole body ($SAR_{sim,total}$) and the partial body ($SAR_{sim,partial}$) were calculated in the simulation for a complete rotation of the patient capsule. Due to the proportionality of the specific absorption rate and the transmit power (SAR $\propto$ P) at the desired frequencies (see eq. 2.51 and eq. 2.31), the maximum allowed transmit power (P_{max}) for the whole body and the partial body could be calculated using the respective SAR limits ($SAR_{limit,total}, SAR_{limit,partial}$) from table 2.1 and the accepted simulated power P_{sim} for the normal and first level mode:

$$P_{max,total} = P_{sim} \cdot \frac{SAR_{limit,total}}{SAR_{sim,total}} \tag{3.2}$$

$$P_{max,partial} = P_{sim} \cdot \frac{SAR_{limit,partial}}{SAR_{sim,partial}} \tag{3.3}$$

The lowest value of the two specified power limits ($P_{max,total}, P_{max,partial}$) for the different angles of rotation is considered safe according to IEC safety regulations.

3.2.5 Process of tuning & matching

The developed RF coils were tuned with capacitors to the respective Larmor frequency of 63.68 MHz (RF body coil) and 10.25 MHz (RF calf coil). To achieve realistic patient loading, the RF coils were tuned while loaded with homogeneous phantoms. Furthermore, all S-parameter measurements of the unshielded RF coils were performed in the respective MR system and with the corresponding patient rotation systems, so that the environment was included in the tuning process. During the tuning of the resonance frequency of the RF body coil, the patient capsule including the homogeneous phantom was positioned in the horizontal position (0° rotation). S-parameters for other rotation angles of the two RF coils including the phantom were investigated in more detail in simulations (see section 4.2.1 and section 4.3.1). The resonance frequency was tuned to the Larmor frequency using tuning capacitors at 32 positions (see fig. 3.4) on the birdcage structure. However, the two tuning capacitors at the position of the matching network were later replaced by parallel capacitors for impedance matching. Similarly, the resonance frequency of the RF calf coil was tuned to the Larmor frequency using tuning capacitors at four positions distributed across the conductor on the solenoid structure, before the tuning capacitor at the matching network was replaced with a parallel capacitor for impedance matching (see fig. 3.6). The simulated and actual capacitance values of the tuning capacitors for the two RF coils are listed in table 3.1.

Table 3.1: Comparison of simulated and actual tuning capacitor values to tune the resonance frequency of the two developed RF coils to the corresponding Larmor frequency.

RF coil	**C_{tune} (setup)**	**C_{tune} (simulation)**	**Relative deviation**
RF body coil	64.2 pF	55.2 pF	16 %
RF calf coil	300.0 pF	238 pF	26 %

The required capacitance values are in a feasible range and can be realized with low-resistance ceramic capacitors. In addition, the deviations of 16−26 % for the measured and simulated capacitance values imply a good agreement between the simulation models (see section 3.2.4) and the real measurement setup (see section 3.2.2).
For the RF body coil, two ports (P1, P2) are required to achieve quadrature excitation and reception (see fig. 3.7). Each port is connected to a coaxial cable via a matching network as shown in fig. 2.7. Adjustable capacitors were used to determine the required parallel and series capacitance in the real setup. Once the RF body coil was matched to the impedance of the coaxial cable ($Z_{cable} = 50\,\Omega$), the parallel and series capacitance was measured (LCR Meter HM8018, HAMEG Instruments GmbH) and the adjustable capacitors were replaced by ceramic capacitors with a

fixed capacitance and a breakdown voltage of 2500 V.
Since the RF calf coil operates as a receive-only coil, smaller ceramic capacitors with a lower breakdown voltage (500 V) could be used. In addition, an adjustable capacitor was implemented in the final design to adjust the resonance frequency for different calves and associated different patient loads. While the RF body coil matching network includes a single serial capacitor, the RF calf coil matching network includes two serial capacitors. Both the inner and outer conductor of the coaxial cable are connected to the solenoid coil via a serial capacitance (see fig. 3.13).

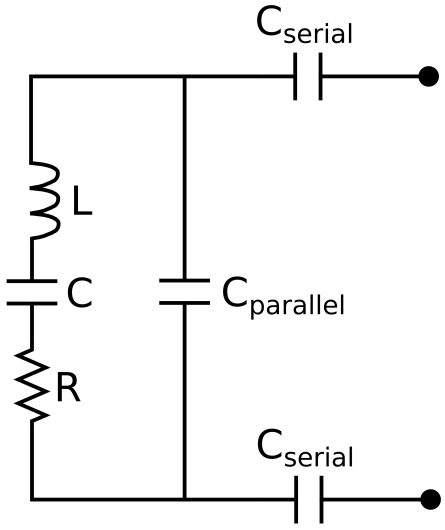

Figure 3.13: Schematic of a balanced matching network with one parallel ($C_{parallel}$) and two serial capacitors (C_{serial}) for impedance matching. In this schematic, the RF calf coil (see fig. 3.6) was simplified as series RLC circuit (L, C, and R).

This balanced configuration of the matching network reduces the dielectric losses, especially in the case of a solenoid coil, and increases the performance of the RF coil [Mispelter et al., 2006].
To detune the RF calf coil during transmission and to protect the developed preamplifier (see section 3.3.3), antiparallel diode pairs (UMX9989AP) were connected in parallel to each of the three tuning capacitors and the parallel capacitor in the matching network (see fig. 3.6). When the induced voltage in the receive-only RF calf coil exceeds a threshold value (≈ 0.7 V) during transmission, the diodes become conductive and act as a short circuit. This bypasses the capacitors and detunes the solenoid. For better detuning, an inductor is placed in series with the diode pairs in the matching network. Additional diodes are located directly on the circuit board of the developed preamplifier (see section 3.3.3).
Table 3.2 summarizes the measured S-parameters, impedances, and Q-factors with (Q_{loaded}) and without realistic patient load ($Q_{unloaded}$) for the two built RF coils.

Table 3.2: Reflection coefficient (S_{11}) and impedance matching at the two coil ports (P1, P2) of the RF body coil and the port of the RF calf coil, measured with a network analyzer at the corresponding Larmor frequencies. In addition, the reflection coefficient and impedance matching of the RF calf coil were determined for both a low power RF signal (0.01 mW) to test the receive case (tuned) and a higher power RF signal (10 mW) to test the transmit case (detuned). The Q-factors measured with a pickup probe with and without realistic patient loading are also shown.

Measurement	**Reflection S_{11}**	**Impedance**	**$Q_{unloaded}$**	**Q_{loaded}**
Body coil (P1)	$-38.7\,\mathrm{dB}$	$50.7\,\Omega - 1.0\,\mathrm{j}\Omega$	≈ 67[1]	≈ 13[1]
Body coil (P2)	$-34.1\,\mathrm{dB}$	$49.4\,\Omega + 1.9\,\mathrm{j}\Omega$	≈ 24[1]	≈ 9[1]
Calf coil (tuned)	$-28.0\,\mathrm{dB}$	$54.0\,\Omega + 0.7\,\mathrm{j}\Omega$	83.2 ± 0.9	67.2 ± 2.6
Calf coil (detun.)	$-1.4\,\mathrm{dB}$	$45.1\,\Omega - 154.9\,\mathrm{j}\Omega$	-	-

[1] Due to large measurement fluctuations and a low response signal of the RF body coil, especially in the loaded case, only approximate values for the Q-factor of the RF body coil could be determined.

The low reflection values for the two coil ports of the RF body coil and the port of the RF calf coil indicate good tuning of the resonance frequency to the Larmor frequency of the respective MR system. In addition to the reflection coefficient, a decoupling of $S_{21} = -16.4\,\mathrm{dB}$ could be achieved between the two ports of the RF body coil, allowing adequate decoupling between the two ports of the RF body coil during transmission and reception.
The impedance of the matching networks is close to $50\,\Omega$ for both coils, allowing RF signals to be transmitted and received with minimal power loss.
For the RF calf coil, the impedance at the coil port during transmission shows a substantial deviation from the impedance of the coaxial cable indicating the detuned state of the RF calf coil. Due to the maximum output power (10 mW) of the network analyzer, the detuning of the RF calf coil could only be evaluated to a limited extent with this setup. While better detuning is expected at higher powers that can be induced in the receive coil during transmission mode, a change in resonance frequency and impedance can also be observed at this power level.
To further characterize the developed RF coils, the Q-factor was measured using a double loop coil (pickup probe) and a network analyzer. For this purpose, the two loops were first decoupled and then positioned inside the RF coil to be investigated. During the measurement, the ports of the RF coil were terminated with an impedance of $50\,\Omega$. In addition, cable traps between the double-loop coil and the network analyzer reduce the interaction with the environment due to sheath waves. To determine the Q-factors (see table 3.2), the mean and standard deviation of three

measurements at different positions within the developed RF coils with and without the homogeneous phantom were calculated. According to eq. 2.65, the power absorbed in the phantom can be calculated from the ratio of the Q-factors in the loaded and unloaded cases. This results in an absorbed power of $P_{torso} \approx 0.7 \cdot P_{total}$ (average of both ports) for the torso phantom in the RF body coil and $P_{calf} = 0.2 \cdot P_{total}$ for the calf phantom in the RF calf coil. Therefore, the power loss in the RF body coil is sample noise dominated, while the power loss in the RF calf coil is coil noise dominated.

3.3 Supplementary radiofrequency electronics

This section deals with additional RF electronics that were designed and tested in this thesis to ensure the functionality of the developed coils. In particular, an RF switch was implemented to separate the transmit and receive modes of the RF body coil. In addition, a quadrature hybrid was designed to achieve circular polarization. For the RF calf coil of the "online" MR system, a low-noise RF preamplifier was developed in order to amplify the detected MR signal. Printed circuit boards were designed in EAGLE (version 9.6.2) for each electronic device in this section. Each PCB consists of two conductive layers, one for the transmission lines and one for the ground plane, separated by an insulating material (FR4). The width of the transmission lines on the PCB has been set so that the impedance between the transmission lines and the ground plane is 50 Ω to minimize power dissipation.

3.3.1 Transmit/receive switch

The RF body coil designed for the "offline" MR system operates as a transmit and receive coil. Accordingly, a transmit/receive switch is required in order to connect the RF coil to the MR system and separate the transmit and receive signals (see section 2.3.10). The schematic of the developed transmit/receive switch is shown in fig. 3.14.
The transmit/receive switch can be divided into the transmit path where the RF power is transferred from the MR system (Tx_{in}) to the RF input of the quadrature hybrid (Tx_{out}), and the receive path, where the MR signal is transferred from the quadrature hybrid (Rx_{in}) through a low-noise preamplifier (Rx_{out}) to the MR scanner.
Multiple π-elements (see fig. 2.10) are used along the transmit and receive paths providing adequate isolation of the preamplifier during RF power transfer. The π-elements act as either an effective blocking circuit or can be passed with almost no power loss with switching via actively controlled positive intrinsic negative (PIN) diodes. During transmission, a current of 100 mA is applied to the PIN diodes, resulting in forward biased PIN diodes that allow RF signals to pass with low loss. Thus, the π-elements act as a blocking circuit, resulting in the reflection of RF power at the appropriate frequency. In the receive mode, the PIN diodes are reverse-biased with −30 V, blocking RF signals. Therefore, RF signals at the given frequency can pass through the π-elements with little loss (see fig. 2.11). The RF switch has a total of three switchable π-elements, two in the receive path and one in the transmit path. In addition to the actively controlled PIN diodes required for switching between the two described states of the π-elements (D2, D4, D5), additional PIN diodes (D1, D3) were implemented to block RF signals during reception. Furthermore, a PIN diode (D4) ensures that the RF power passed to port Rx_{in} from the RF body coil during the transmission mode is dissipated as heat in a 50 Ω termination (6550.17.AA, Huber

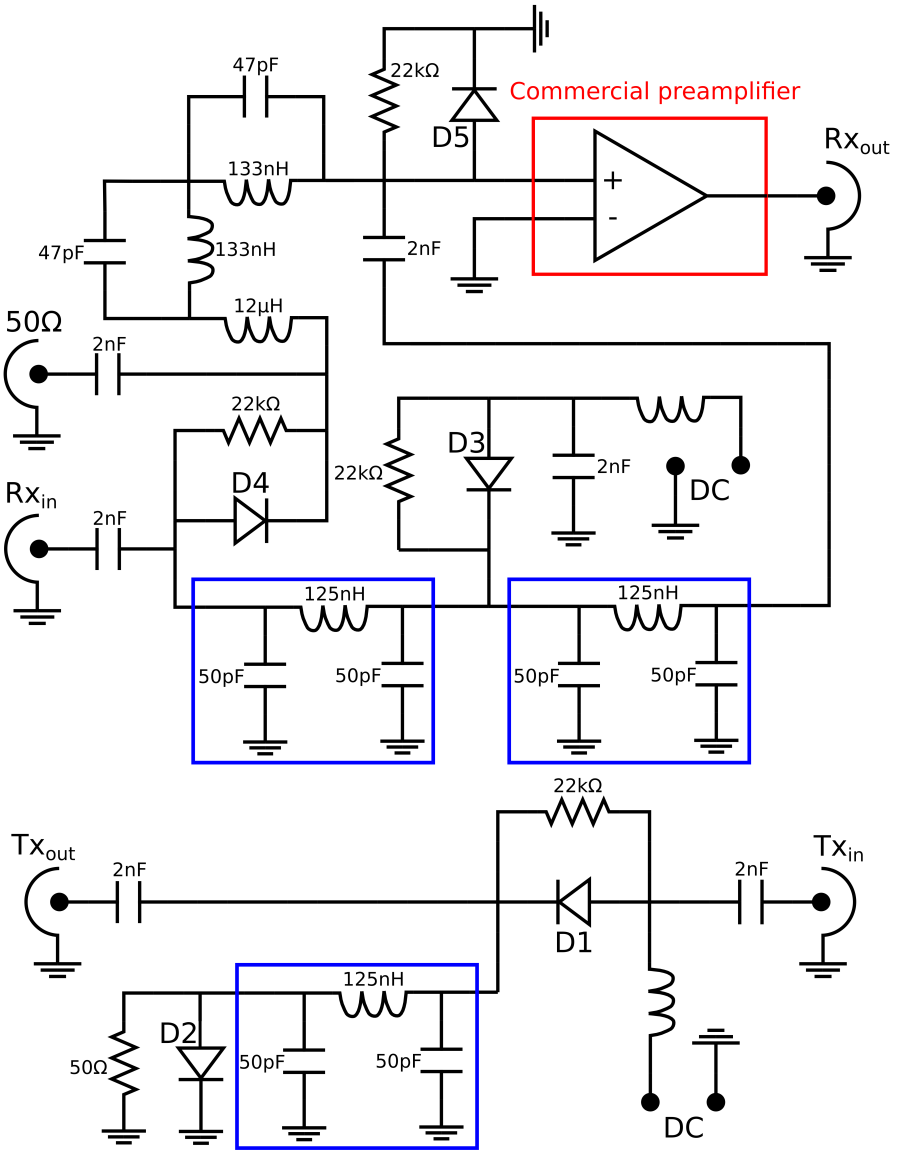

Figure 3.14: Schematic of the designed transmit/receive switch for the "offline" 1.5 T MR system, including values used for all capacitors, inductors, and resistors involved. A total of five positive intrinsic negative (PIN) diodes (D1, D2, D3, D4, D5) are controlled by two DC signals (100 mA/−30 V) for switching the corresponding π-elements (blue boxes) to block or pass the RF signals. A commercial preamplifier (red box) is operated with a supply voltage of 10 V via the receive channel.

& Suhner, Pfäffikon, Switzerland). Table 3.3 shows the S-parameters measured with the network analyzer (Agilent E5061B) between the RF inputs and outputs of the Tx/Rx switch for the transmit and receive cases. In the transmit case, the RF signal can pass through the transmit path ($Tx_{in} \rightarrow Tx_{out}$) without substantial power loss, while the receive path ($Rx_{in} \rightarrow Rx_{out}$) has a high level of isolation to protect the sensitive preamplifier. At the same time, the power passed to port Rx_{in} from the the RF body coil is transferred directly to the 50 Ω termination ($Rx_{in} \rightarrow 50\,\Omega$). During reception, the MR signal reaches the low-noise preamplifier ($Rx_{in} \rightarrow Rx_{out}$) while both the transmit path and the connection to the 50 Ω termination are blocked at the appropriate RF frequency.

Table 3.3: S-parameters between the different RF outputs of the transmit/receive switch during transmission and reception, measured with a network analyzer at 63.68 MHz.

Signal path	**Transmit coefficient S_{21} (transmission)**	**Description**
$Tx_{in} \rightarrow Tx_{out}$	−0.6 dB	Little losses
$Rx_{in} \rightarrow 50\,\Omega$	−0.4 dB	Little losses
$Rx_{in} \rightarrow Rx_{out}$[1]	−47.3 dB	Good isolation
Signal path	**Transmit coefficient S_{21} (reception)**	**Description**
$Tx_{in} \rightarrow Tx_{out}$	−29.3 dB	Good isolation
$Rx_{in} \rightarrow 50\,\Omega$	−28.5 dB	Good isolation
$Rx_{in} \rightarrow Rx_{out}$[1]	−0.4 dB	Little losses

[1] The RF signal was measured at the input of the preamplifier facing the RF body coil.

The capacitance and inductance values from table 2.3 were slightly modified to match the π-elements in the real setup to the Larmor frequency of the MR system (63.68 MHz). An LCR meter (HM8018, HAMEG Instruments) and an impedance analyzer (Agilent 4294A) were used to measure and adjust the capacitance and inductance values.
A commercial low-noise preamplifier (gain: 29.8 dB, noise figure: 2.5 dB at 63.68 MHz measured with a noise figure analyzer (Agilent N8973A) using a reference noise source (Agilent N4000A)) was mounted on the designed PCB. Five capacitors (C = 1 nF) connect the separate ground plane of the preamplifier and the ground plane of the Tx/Rx switch in order to avoid DC currents between the two areas. Furthermore, the Tx/Rx switch was mounted in a box and connected with coaxial cables to the corresponding transmit and receive channels as well as to the 50 Ω termination and the DC signals for driving the PIN diodes (see fig. 3.15).

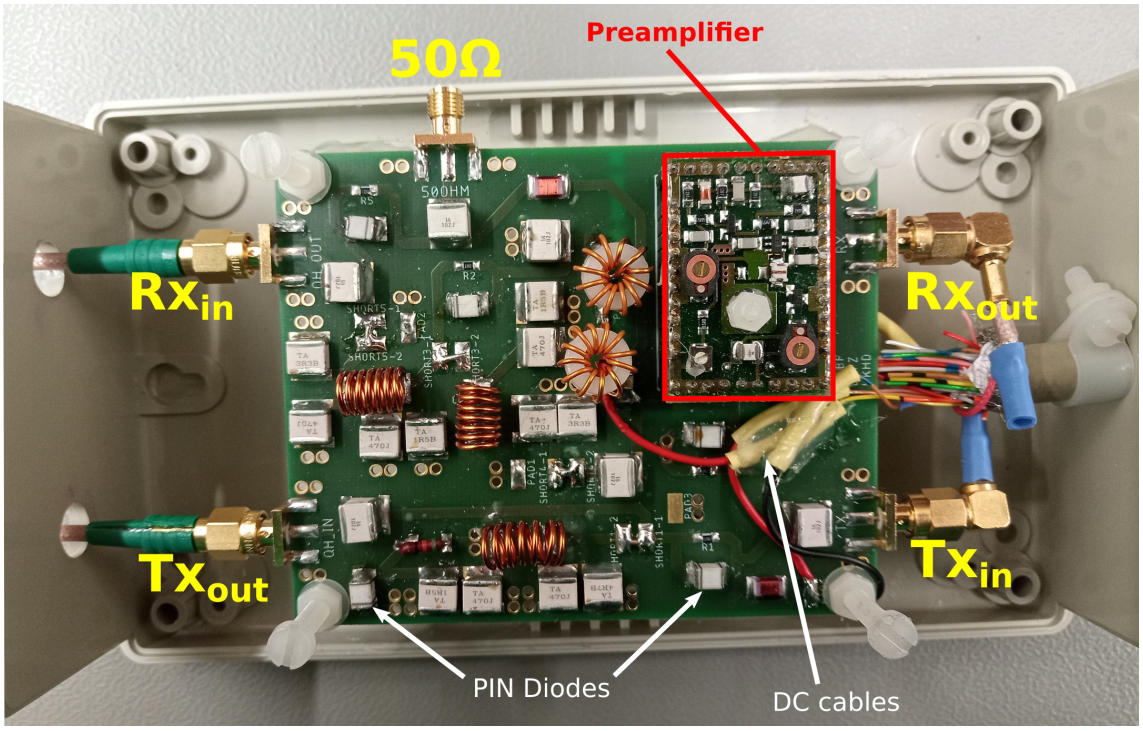

Figure 3.15: Transmit/receive switch with a preamplifier designed for 63.68 MHz. π-elements with the appropriate capacitance and inductance values provide high isolation between the transmit and receive paths for the given frequency and can be actively controlled by PIN diodes. The printed circuit board is mounted in a box that protects the sensitive electronics from mechanical shock and prevents direct contact between the patient and the conductor.

3.3.2 Quadrature hybrid

A quadrature hybrid was designed for the "offline" MR system according to the schematic in section 2.3.9 and used as a passive element to achieve circular polarization of the RF body coil. The theoretical capacitor and inductor values from table 2.2 were slightly modified for the real setup to optimize the quadrature hybrid for the Larmor frequency of 63.68 MHz. Similar to the Tx/Rx switch in the previous section, the quadrature hybrid was mounted in a box to protect both the electrical components and the patient (see fig. 3.16).

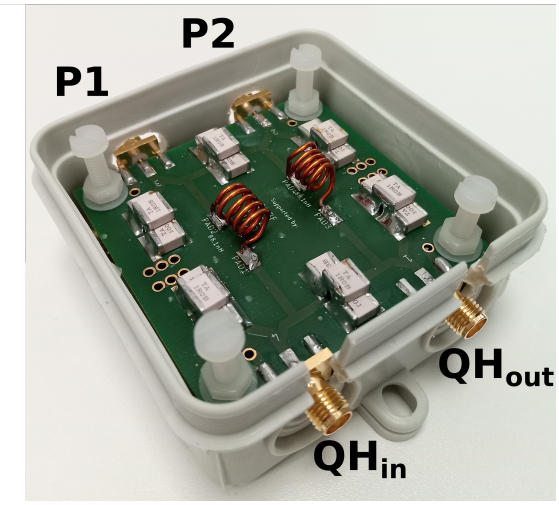

Figure 3.16: Realization of a quadrature hybrid (see section 2.3.9) at 63.68 MHz. To achieve circular polarization during transmission, the RF signal of the incoming RF pulse (QH_{in}) is divided equally between the two outputs leading to the coil ports (P1, P2) (see fig. 3.7) with a phase shift of 90°. In the receive mode, the received MR signal from both coil ports (P1, P2) is combined with the same phase and transmitted to the Tx/Rx switch with the preamplifier via the output of the quadrature hybrid (QH_{out}).

The phase relationships and S-parameters between the RF inputs and outputs are listed in table 3.4.

Table 3.4: S-parameters and accumulated phases between the different RF outputs of the quadrature hybrid measured with a network analyzer at 63.68 MHz.

Signal path	**Transmit coefficient (S_{21})**	**Transmitted power**	**Phase difference (S_{21})**
QH_{in} → Coil Port 1	−3.10 dB	49 %	-104.57°
QH_{in} → Coil Port 2	−3.23 dB	48 %	-14.63°
Coil Port 1 → QH_{out}	−3.23 dB	48 %	-14.84°
Coil Port 2 → QH_{out}	−3.11 dB	49 %	-104.75°
QH_{in} → QH_{out}	−22.45 dB	<1 %	-168.69°

The S-parameters show that the quadrature hybrid distributes the RF power approximately equally ($\approx$ −3.01 dB) between the two coil ports during transmission. Since the outgoing RF power at both ports is less than 50 % of the incoming power, combined losses of up to −0.32 dB can occur in the quadrature hy-

brid. A phase difference of $|\Delta\phi| = |(-14.63°) - (-104.57°)| = 89.94°$ could be achieved between the two coil ports in the transmit case, and a phase difference of $\Delta\phi = |(-14.84°) - (-104.75°)| = 89.91°$ in the receive case. In addition, a high isolation was achieved between the RF input of the quadrature hybrid and the RF output to the receive path.

3.3.3 Radiofrequency preamplifier

For the "online" MR system, a printed circuit board for a low-noise preamplifier was designed to amplify the MR signal from the developed RF calf coil. The central component of the low-noise preamplifier at the frequency of 10.25 MHz is the "PHA-23LN+" amplifier element, which requires a supply voltage of 3.3 V for optimal performance. However, the supply voltage was measured at the output of the "online" MR system and corresponds to 15 V. Therefore, two voltage dividers (15 V→5 V and 5 V→3.3 V) were used in series connection to reduce the supply voltage at the input of the amplifier component. Since the noise figure of the preamplifier is highly dependent on the stability of the supply voltage, parallel capacitors with large capacitance values were added to avoid voltage fluctuations. A complete schematic of the preamplifier is shown in fig. 3.17. Two passive diodes in opposite direction at the RF input and the RF output of the preamplifier board were implemented in parallel to the ground plane in order to protect the sensitive RF components during the transmission of an excitation pulse.
Electrical connections between the top and bottom plane of the PCB (vias) near the voltage dividers and the amplifier element increase the heat transfer to the ground plane and protect the electronic components from overheating (see fig. 3.18).
To characterize the preamplifier, both the noise figure and the gain between the RF input and the RF output were determined at a frequency of 10.25 MHz. A noise figure of 1.0 dB was measured for the preamplifier with a noise figure analyzer (Agilent N8973A) using a reference noise source (Agilent N4000A). The gain of the preamplifier was measured with a network analyzer (Agilent E5061B) and corresponds to 23.5 dB. For use in the MR system, the preamplifier was packaged in a case to protect the sensitive electronics.

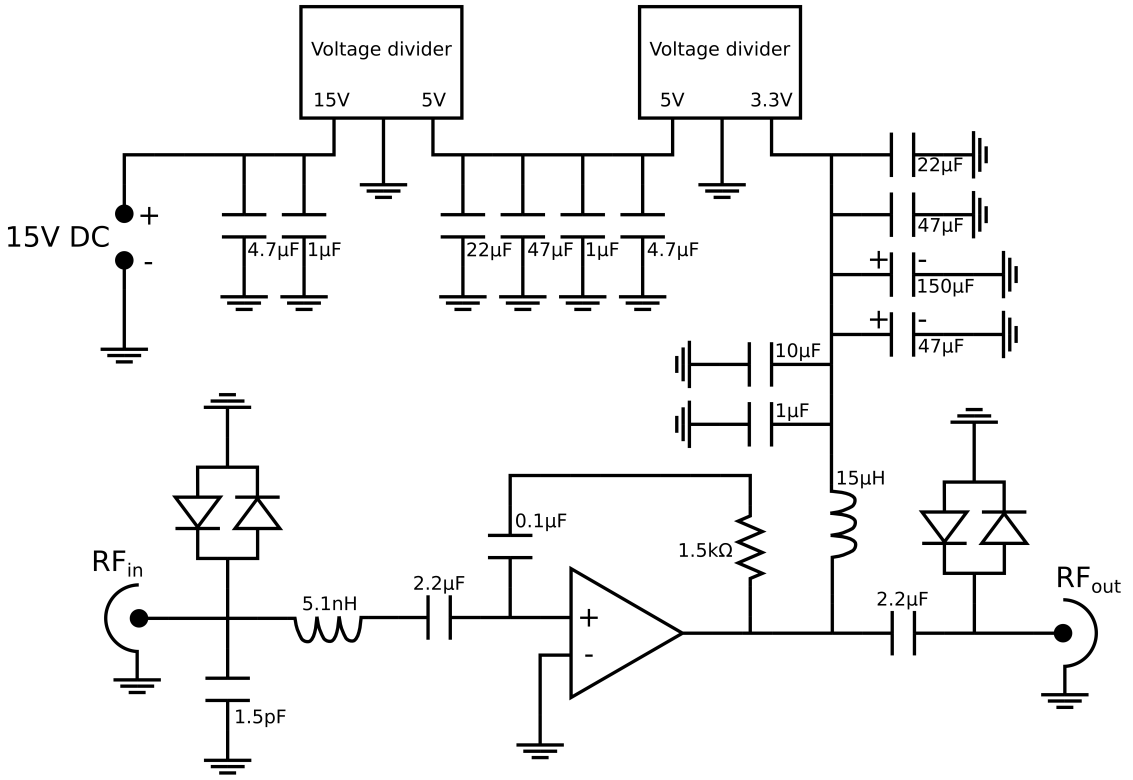

Figure 3.17: Schematic of the designed preamplifier for the "online" 0.25 T MR system, including values for all capacitors, inductors, and resistors involved. The supply voltage of 15 V is converted to 5 V and then to 3.3 V according to the specifications of the amplifier component. Parallel capacitors between DC and ground plane compensate for supply voltage fluctuations, reducing the noise figure of the preamplifier. The RF transmission line and power supply are separated for RF signals by a high inductance (15 µH), resulting in a high impedance ($Z = \omega L$) that effectively blocks all RF signals.

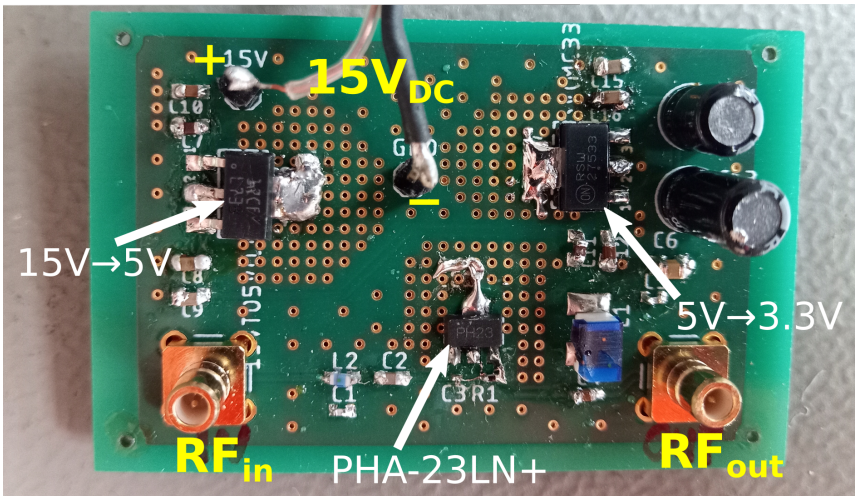

Figure 3.18: Low-noise preamplifier design to amplify the received MR signal from the RF calf coil. Incoming RF signals (RF_{in}) are amplified in the amplifier component (PHA-23LN+) and transmitted to the MR system (RF_{out}). The supply voltage of 15 V from the MR system is connected via DC cables to the DC ports of the preamplifier and is reduced to 5 V in the first voltage divider (15V→5V) and then to 3.3 V in the second voltage divider (5V→3.3V) to match the specifications of the amplifier component. In addition, numerous vias ensure sufficient thermal conductivity to the ground plane.

3.4 MR image acquisition

This section deals with the acquisition and processing of the measured MR images for both developed RF coils. In this context, the different measurements are listed and the main objectives are described. In addition, the calculation of the B_1 maps and the signal-to-noise ratio from the image data is described.

3.4.1 Measurements

In order to characterize the performance of the developed RF coils, several MR measurements were performed to evaluate the imaging properties of the RF body coil and the RF calf coil. Relevant information regarding the pulse sequences used for imaging will be addressed in the respective sections. The image acquisition in this thesis can be divided into three parts:

- **B_1 maps:** To evaluate the transmit and receive characteristics of the RF body coil, the B_1 maps were acquired in a homogeneous torso-sized phantom for a complete rotation of the patient capsule in steps of 15°. Two MR images were required for each of the 24 different rotation angles in order to calculate the corresponding B_1 field distributions (see section 3.4.3). A gradient echo (GRE) sequence was chosen for image acquisition. The rotation angles of the patient capsule were measured in a scout image at the edge of the phantom before the actual measurement and could be adjusted accordingly. To position the phantom in the center of the magnetic field, a fingertip-sized PinPoint phantom (Beekley Medical, Bristol, USA) was placed at the top center, which was also visible in the scout image.

- **SNR:** In terms of SNR, the above mentioned MR measurements of the RF body coil were compared with those for the internal body coil of the "offline" MR system. For this purpose, the same homogeneous torso phantom was measured in an identical patient capsule without an RF body coil using the internal body coil for image acquisition. Correspondingly, 24 additional measurements were performed with the internal body coil at the same rotation angles of the patient capsule using the same MR sequence. For the SNR study of the RF calf coil on the "online" MR system, the homogeneous calf-sized phantom was oriented in the horizontal position (0° rotation). To compare the SNR of the RF calf coil with commercial reference coils, additional MR images of a dual-channel knee coil and a single-channel cervical coil were acquired using a GRE sequence with the same parameters for all three RF coils.

- **Image contrast:** To confirm the imaging quality of the developed RF coils and to demonstrate the high image contrast that can be achieved between different tissue types, MR images were acquired from a heterogeneous phantom

and in vivo. For the RF body coil, a heterogeneous silicone-based torso phantom filled with agar (see fig. 3.11) was measured using T_1- and T_2-weighted MR sequences for two different rotation angles of the patient capsule (0° and 90°) to illustrate different contrasts. Similarly, in vivo imaging with T_1- and T_2-weighted MR sequences was performed on the "online" MR system.

3.4.2 Coil calibration

To meet the requirements for optimal imaging, the developed RF coils were calibrated to the respective MR system. For the "online" MR systems however, the receive-only RF calf coil could only be calibrated indirectly since access to the developer environment was not possible.
In contrast to the "online" MR system, access to the development environment was available for the "offline" MR system. Therefore, power limits and other parameters for the transmit/receive RF body coil could be set manually in a user-defined coil file. In addition, the reference voltage of the RF body coil could be determined individually for all setups by the user.
The reference voltage U_{ref} is defined by the manufacturer of the "offline" MR system as the pulse voltage of a rectangular RF pulse with a pulse duration of $t_{pulse} = 1\,\text{ms}$ that is required to achieve a flip angle of $\alpha = 180°$. The reference voltage for the developed RF body coil and the internal body coil of the MR scanner were measured with the homogeneous torso phantom and corresponded to $U_{pulse} = 315\,\text{V}$ and 343 V, respectively. Since the flip angle is proportional to the applied pulse voltage ($\alpha \propto U_{ref}$), a lower pulse voltage is required with the RF body coil than with the internal body coil to achieve the same flip angle. The pulse voltage can be adjusted to achieve the desired flip angle when the reference voltage is known.

3.4.3 Mapping of transmit and receive fields

To investigate the performance of the two developed RF coils in a volume, several 2D slices were measured for each MR image. The distance between two adjacent slices and the nominal width of a slice were chosen to correspond to the voxel width of the phase encoding and frequency encoding directions. Thus, a 3D dataset with an isotropic spatial resolution in all spatial directions could be obtained from the MR measurements. For both the calculation of the B_1 maps and the SNR calculation, the measured 3D datasets were exported as Digital Imaging and Communications in Medicine (DICOM) files and accessed with a Python script. Similarly, the simulated B_1 maps were exported as text file and accessed by another Python script. In the Python scripts, the 3D datasets were converted into an array (Python package: numpy [Harris et al., 2020]), allowing the selection of a 3D subvolume or a 2D slice in any spatial direction to study the RF field and intensity distributions of the MR images. In addition, the dataset could be better investigated for the determination

of RF field homogeneity and the SNR using thresholds or a region of interest (ROI) of defined size.
The B_1 maps of the RF body coil were obtained using the double-angle method [Insko and Bolinger, 1993]. Accordingly, two MR images of the homogeneous phantom were acquired with the same sequence parameters, except for different flip angles. Furthermore, the flip angles of the two MR images were chosen in such a way that the flip angle of the first measurement (α_1) corresponds to exactly half of the flip angle of the second measurement ($\alpha_2 = 2 \cdot \alpha_1$). Since the signal intensity S in the MR images depends on the selected flip angle, the ratio (R_{12}) of the signal intensities from the two MR images (S_{α_1}, S_{α_2}) can be used to calculate the flip angle map of the transmit coil:

$$R_{12} = \frac{S_{\alpha_1}}{S_{\alpha_2}} = \frac{sin(\alpha_1)}{sin(\alpha_2)} = \frac{sin(\alpha_{map})}{sin(2 \cdot \alpha_{map})} = \frac{1}{2 \cdot cos(\alpha_{map})} \tag{3.4}$$

$$\alpha_{map} = arccos\left(\frac{1}{2 \cdot R_{12}}\right) \tag{3.5}$$

Consequently, the flip angle map (α_{map}) can be obtained for the set nominal flip angle α_1. Using eq. 2.31, the B_1^+ map can be calculated from the flip angle map as follows:

$$B_{1\ map}^{+} = \frac{1}{\gamma \cdot t_{pulse}} \cdot arccos\left(\frac{1}{2 \cdot R_{12}}\right) \tag{3.6}$$

Due to the constant spin density ρ_{spin} in a homogeneous phantom, intensity fluctuations in MR images can only be attributed to inhomogeneities in the B_1 maps (B_0 is assumed to be constant). Thus, the relative receive map (B_1^-) can be calculated from the transmit field map (B_1^+) and the intensity distribution of the corresponding MR image with flip angle α_1:

$$S_{\alpha_1} \propto \rho_{spin} \cdot sin(\alpha_{map}) \cdot B_{1\ map}^{-} \tag{3.7}$$

$$B_{1\ map}^{-} \propto \frac{S_{\alpha_1}}{sin(\alpha_{map})} \tag{3.8}$$

Since the determination of the B_1 maps from measurements with the double angle method involves the division of two MR images (see eq. 3.4), extreme values may occur in the flip angle map, especially at the edges of the phantom. Since these extreme values do not reflect the RF field distribution, they should not be considered when evaluating the performance of the RF coil. Therefore, the values outside the phantom (background) were identified using a threshold, and set to zero. Subsequently, all voxels directly adjacent to the edge of the phantom were also removed

from the calculation of the B_1 maps, as these can be distorted, e.g. by partial volume effects.
The B_1 maps from the measurements were calculated according to eq. 3.6 and 3.7 while the simulated B_1 maps were calculated from the exported real and imaginary parts of the B_1 field distributions. In addition, the transmit power efficiency of the developed Tx/Rx body coil was calculated for the measured transmit field (B_1^+) in the transverse slice of the phantom for different rotation angles and compared with the simulation.
In the scope of this work, the two MR images for the calculation of the B_1 maps of the RF body coil were acquired with a gradient echo sequence with chosen flip angles of $\alpha_1 = 60°$ and $\alpha_2 = 120°$ as they provide the best results for volume coils [Stollberger and Wach, 1996]. The MR measurements with the flip angle $\alpha_1 = 60°$ were also used to calculate the signal-to-noise ratio of the RF body coil.

3.4.4 Determination of signal-to-noise ratio

To calculate the SNR from the MR images (see eq. 2.52), the mean signal intensity (S_{mean}) within the homogeneous phantom and the standard deviation (SD) of the background signal (voxels without phantom (air), excluding voxels in close proximity to the phantom) were determined [NEMA, 2008] (NEMA, method 4). To separate the voxels inside the phantom from the background, masks were defined using thresholds. The selected masks contain a sufficient number of voxels to obtain a representative value for the signal intensity and the image noise from the background. For the comparison between different RF coils, the thresholds were adjusted so that the number of voxels within the masks was approximately the same. Since the measured signal intensity in the background of the MR image follows a Rayleigh distribution, a correction factor is required to calculate the image noise:

$$Image\ noise = \frac{SD}{0.66} \tag{3.9}$$

3.5 Particle irradiation

In this section, the ion beam therapy facility used for the radiation experiments in this thesis is introduced and specific characteristics of the beam delivery and the experimental setup for depth dose measurements are described. In this context, the penetration depth of an ion beam in a water column is measured to investigate the ion attenuation caused by the materials used in the construction of the RF coils.

3.5.1 Ion beam facility

All irradiation experiments presented in this thesis were performed at the Heidelberg Ion Beam Therapy Center [Haberer et al., 2004] (HIT). The ion beam facility consists of a linear accelerator and a synchrotron, with beam energies of approximately $50 - 430\,\frac{\mathrm{MeV}}{\mathrm{u}}$ for hydrogen, helium, carbon and oxygen ions. This energy range corresponds to penetration depths of $2-30\,\mathrm{cm}$ in water and thus enables potential application in cancer therapy. The beam delivery of the particles is actively modulated by the intensity-controlled rasterscan technique using magnetic fields to deflect the ion beam laterally [Haberer et al., 1993]. This allows the ion beam to cover a treatment field of up to $20\times20\,\mathrm{cm}^2$. The cross section of a pencil beam determines the beam spot size in the treatment field and is usually given by the full width at half maximum, which can be varied between $4-10\,\mathrm{mm}$ [Haberer et al., 2004]. The beam intensity for protons and carbon ions is different and corresponds to $4 \cdot 10^{10}$ and $1 \cdot 10^{9}$ particles per synchrotron cycle, respectively.

3.5.2 Investigation of depth-dose curves for particles

A Peakfinder Water Column (PTW Freiburg, Freiburg, Germany) can be used to measure the depth-dose curve of particle beams in water [Karger et al., 2010]. An ionization chamber (see section 2.5.1) scans the ionization charge or the integrated dose-area product for each position along the water column, resulting in the typical dose distribution of a Bragg curve (see section 2.5.3). To measure the stopping power of specific components containing unknown materials or materials of uncertain thickness, these components can be positioned in the beam path in front of the peak finder. The depth dose curve obtained in water was then compared to a reference measurement without attenuating materials in front of the peak finder, and the change in the Bragg peak position relative to the reference measurement was used to determine the corresponding WET of the components. In addition, a change of the longitudinal width of the Bragg peak can indicate scattering effects or ion attenuation of only a portion of the beam cross section.
To evaluate the effect of the components used to construct the RF coils, such as the acrylic-based adhesive layers (3M467) of uncertain thickness (specified as $12-25\,\mu\mathrm{m}$ and $50\,\mu\mathrm{m}$ by db electronic® GmbH, Waldshut-Tiengen, Germany) and chemical

composition, on the ion beam and to validate the calculated stopping power for known materials according to eq. 2.77, the WET of the RF coil components (see fig. 3.5) was measured at the HIT. For this measurement, a representative piece of the flexible printed circuit board, which is required for the construction of the RF coil, was placed between the exit of the beam line and the entrance of the water column at a distance of approximately 25 cm to the water column (see fig. 3.19).

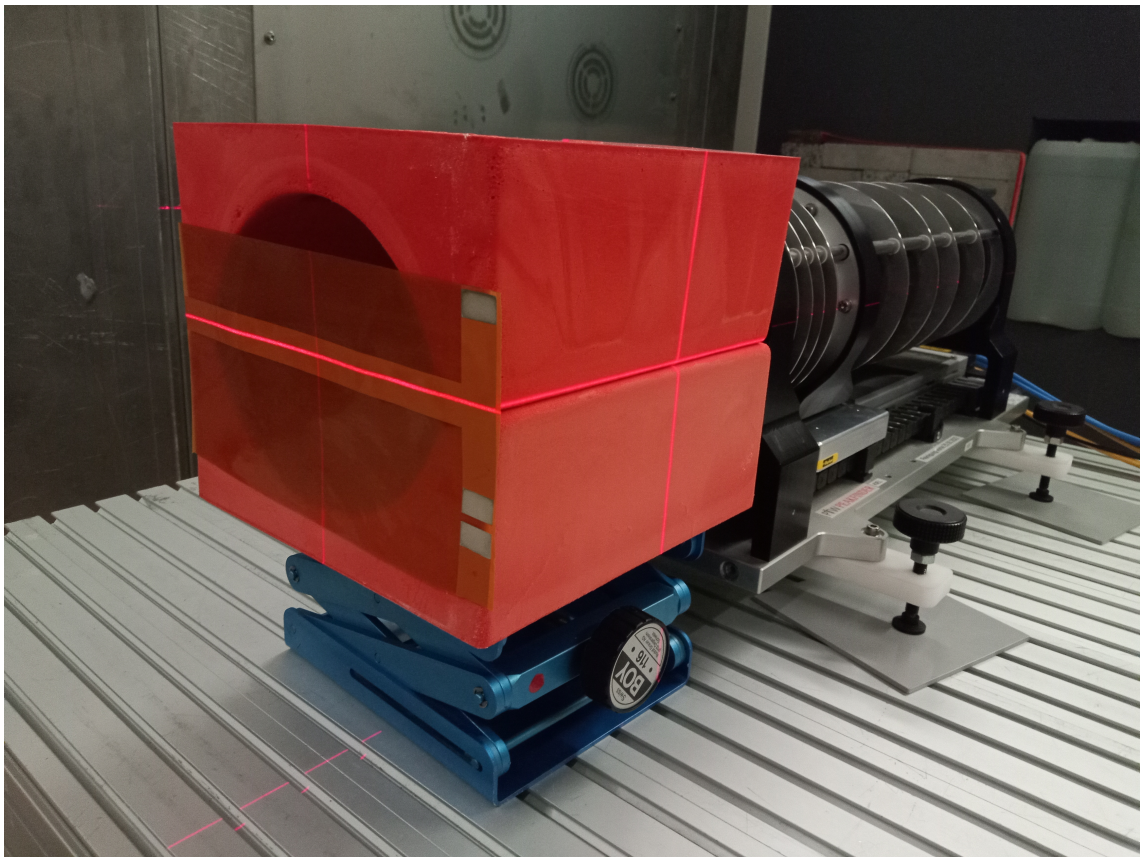

Figure 3.19: Measurement setup of the Peakfinder water column to determine the depth dose curves of particle beams. A portion of a flexible printed circuit board, identical to that of the RF body coil was attached to a height-adjustable rigid foam with an opening that allowed only the flexible circuit board to be irradiated. The laser positioning system was used to direct the particle beam to specific structures on the flexible circuit board. The image shows the positioning for irradiation through the conductor.

Irradiation of the different RF coil sections was performed using $^{12}C^{6+}$ ions with a full-width-half-maximum of 5.1 mm at a beam energy of 200.3 $\frac{\text{MeV}}{\text{u}}$ and a particle rate of $5 \cdot 10^6$ particles per second. For sufficient spatial resolution of the resulting depth dose curve along the beam axis, the step size for the movable ionization chamber in the water column was set to 50 µm. The beam axis of a pencil beam is indicated with a laser system, allowing the flexible PCB to be positioned accordingly.

For a complete evaluation of the ion attenuation in the irradiation window, the flexible circuit board was irradiated at three different positions and the corresponding depth dose curves were recorded with the water column:

- **Case 1:** Irradiation of the flexible printed circuit board at a position where the ion beam penetrates all layers, including the copper conductor, for maximum ion attenuation.
- **Case 2:** Irradiation of the flexible printed circuit board at the edge of the conductor, where half of the beam cross section of the ion beam penetrates all layers including the conductor and the other half penetrates all layers except the conductor. Possible scattering effects of the non-uniform ion attenuation along the beam cross section can partly be investigated in the depth dose curve.
- **Case 3:** Irradiation of the flexible printed circuit board at a position where the ion beam penetrates all layers except the conductor and thus experiences the minimum ion attenuation.

In addition, another depth dose curve was recorded without the flexible PCB as a reference measurement. Hence, the WET for each case could be calculated from the change in the position of the Bragg peak between the measurement and the reference measurement.
In contrast to the polyimide, the adhesive layers and the patient capsule where the material can be assumed to be homogeneously distributed, the conductor does not cover the entire irradiation window and thus cannot be compensated with higher beam energies. Furthermore, the high density of the copper ($8.92\frac{g}{cm^3}$) results in a high stopping power (see eq. 2.77). Therefore, the ion attenuation of the conductor is of major importance in assessing the radiation transparency of the RF coil. Accordingly, the WET for the conductor was calculated by subtracting the WET from cases 1 and 3.
To ensure that the flexible PCB does not cause any substantial range straggling effects [Newhauser and Zhang, 2015], the longitudinal width of the Bragg peak along the beam axis was determined for each case and compared with one another. Furthermore, the measurements for the cases mentioned above were repeated with a different part of the flexible printed circuit board in order to evaluate possible deviations in layer thickness and the reproducibility of the measurement procedure with the water column.

Chapter 4

Results

In this chapter, both the radiation transparency and the imaging properties of the two developed RF coils are subjected to a quantitative analysis and the results of this investigation are presented. On the one hand, the RF field homogeneity and the signal-to-noise ratio (SNR) of the developed RF coils in a region of interest (ROI) were evaluated in comparison to commercially available coils, and on the other hand, the influence of rotation on the imaging properties was assessed. All graphs with quantitative numbers were created using Python (Python package: matplotlib.pyplot [Hunter, 2007]). In addition, MR imaging was performed in heterogeneous phantoms and in vivo to demonstrate the ability to illustrate different tissue types.

4.1 Radiation transparency for particles

This section covers the calculations and measurements related to the radiation transparency of the RF coils. In particular, the stopping power of the materials used and the water-equivalent thickness of the RF coil components are discussed. To investigate the influence of the RF coil on a potential irradiation plan, the position and width of the Bragg peak were examined using depth dose measurements in a water column (see section 3.5.2).

4.1.1 Theoretical determination of the ion attenuation

For a detailed examination of the radiation transparency of the individual layers of the RF coil (see fig. 3.5), the stopping power of copper, polyimide and PMMA was calculated according to eq. 2.77. In addition, the stopping power of water was calculated to compare the ion attenuation of each material with that of water and to determine the water equivalent thickness (see eq. 2.80) of the different materials. To calculate the stopping power, the average ionization potential and the electron density were determined for each material (see eq. 2.79 and 2.78). For materials consisting of several atoms (water, polyimide or PMMA), an effective atomic number (Z_{eff}) and mass number (A_{eff}) was derived from the mass ratio of the atoms in the

molecule. For example, the mass-weighted effective atomic number of H_2O can be calculated from the atomic numbers (Z_H, Z_O) and masses (m_H, m_O) of the hydrogen and oxygen atoms:

$$Z_{eff}(H_2O) = \frac{2 \cdot Z_H \cdot m_H + Z_O \cdot m_O}{2 \cdot m_H + m_O} \approx 7.22 \tag{4.1}$$

A list of all material properties used in the stopping power calculation of the RF coil components is shown in table 4.1.

Table 4.1: Material properties for the different layers in the developed RF coils.

Material properties	**Copper**	**Polyimide**	**PMMA**	**Water**
Density (ρ) in $\frac{g}{cm^3}$	8.96	1.42	1.19	1.00
Atomic number (Z_{eff})	29.00	6.36	6.24	7.22
Mass number (A_{eff})	63.62[1]	12.69	12.39	14.32
Ratio $\frac{Z_{eff}}{A_{eff}}$ in %	45.58	50.12	50.36	50.42
Ionization potential (I_E) in eV	290	63.6	62.4	72.2
Electron density (n) in $\frac{electrons}{m^3}$	$2.46 \cdot 10^{30}$	$4.29 \cdot 10^{29}$	$3.61 \cdot 10^{29}$	$3.04 \cdot 10^{29}$

[1] The mass number of copper is calculated from the average of the two naturally occurring copper isotopes ^{63}Cu and ^{65}Cu taking into account the natural abundances of approximately $A(^{63}\text{Cu}) \approx 69.15\,\%$ and $A(^{65}\text{Cu}) \approx 30.85\,\%$ [Laeter et al., 2003] [Kondev et al., 2021].

Using the values from table 4.1, the stopping power and the stopping power ratio (SPR) relative to water of each material can be calculated for an ion beam energy range of 48−221 MeV for protons with charge number z=+1 and $88 - 430\,\frac{\text{MeV}}{\text{u}}$ for carbon ions (z=+6).
The calculated stopping powers for the different materials in the layered structure of the developed RF coils show a dominant ion attenuation by the conductor (see fig. 4.1). In the evaluated energy range, the stopping power of copper reaches values of $2.6 - 7.7\frac{MeV}{mm}$ for protons and $65.9 - 174.4\frac{MeV}{mm}$ for carbon ions. The stopping power of the other substances is considerably lower, but a similar energy dependence can be observed. Consequently, the stopping power ratio of the materials relative to water results in almost constant values over the energy range.
The calculated average stopping power ratio of the different materials is shown in table 4.2 for the complete energy range and for both particles.

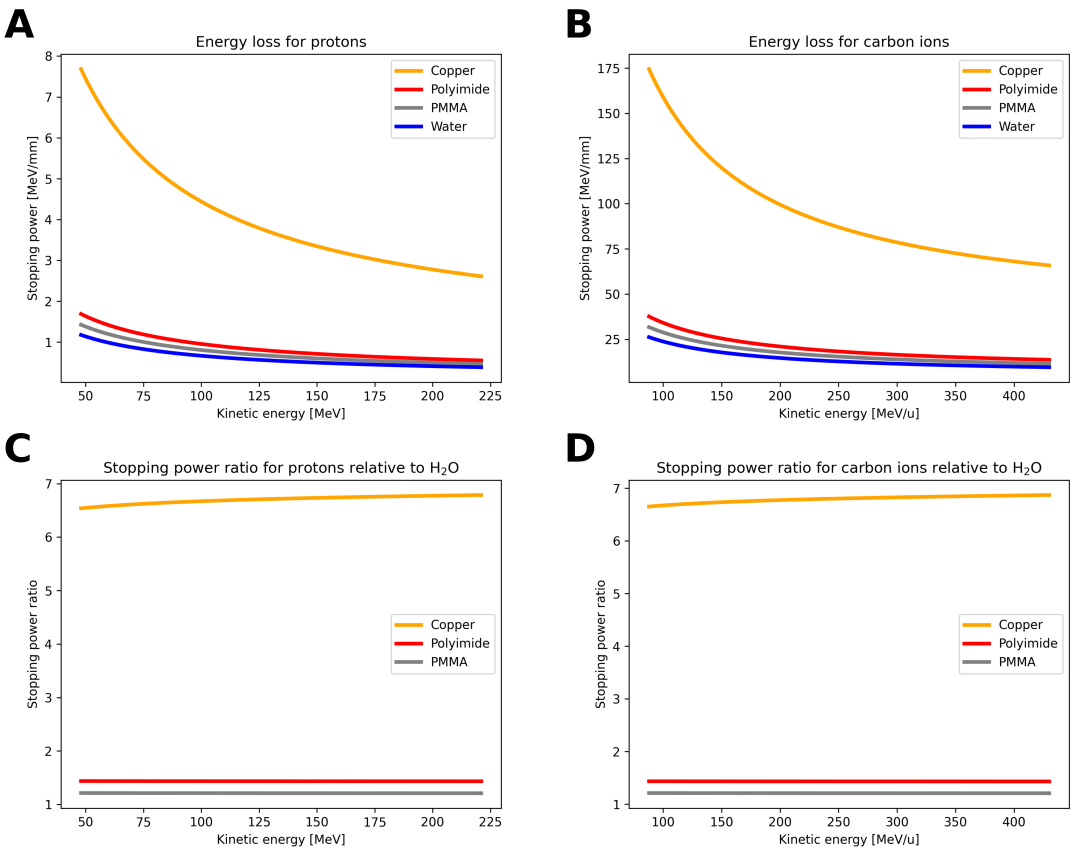

Figure 4.1: Stopping powers in copper, polyimide, PMMA and water for protons (**A**) and carbon ions (**B**) in the clinically relevant energy range calculated with eq. 2.77. In addition, the stopping power ratio of the above materials relative to water was determined for protons (**C**) and carbon ions (**D**) in order to calculate the water equivalent thickness. Copper has a substantially higher stopping power than the other materials and must therefore in particular be considered for the radiation transparency of the RF coils.

Table 4.2: Calculated stopping power ratio relative to water for the materials of the developed RF coils averaged over the clinically relevant energy range.

Stopping power ratio (SPR) (average over energy range)	**Copper**	**Polyimide**	**PMMA**	**Water**
SPR (protons)	6.70	1.43	1.21	1.00
SPR (carbon ions)	6.79	1.43	1.21	1.00

In contrast to polyimide and PMMA, the average stopping power ratio of copper is slightly dependent on the particle type. For a conductor with a thickness of 35 µm, this results in a calculated average WET of 235 µm for protons and 238 µm for carbon ions. In addition, the corresponding stopping power ratio of 6.77 can be given for the carbon ions from section 3.5.2 for the applied energy of 200.3 MeV. Therefore, a value of 237 µm is expected for the measured WET of the conductor.
The stopping power for the adhesive layers in the coil structure (see fig. 3.5) cannot be calculated because the exact chemical composition of the adhesive is not known. However, assuming that the stopping power is proportional to the density of the material ($S \propto \rho$), the stopping power ratio relative to water can be estimated ($\mathrm{SPR}_{glue} \approx 1.01 \cdot \mathrm{SPR}_{\mathrm{H_2O}}$) based on the known density of the glue ($\rho_{glue} = 1.01 \frac{g}{cm^3}$). Thus, the WET of 75−101 µm for all adhesive layers included, the estimated total WET of the developed RF coils, excluding the PMMA cylinders, is 419−445 µm for the applied energy of 200.3 MeV.
To fully account for the ion attenuation of the RF body coil and the RF calf coil, the wall thickness of the PMMA cylinders was measured. The average wall thickness amounts to (9.29 ± 0.07) mm for the RF body coil and (4.02 ± 0.03) mm for the RF calf coil. The specified errors correspond to the standard deviations of the individual measurements. The standard deviation of the wall thickness of the PMMA cylinders due to manufacturer tolerances results in a WET deviation of 88 µm for the RF body coil and 40 µm for the RF calf coil.

4.1.2 Bragg peak measurements

To determine the depth dose curve for carbon ions using a water column (see section 3.5.2), a penetration depth between 83.5 mm and 87.5 mm was examined with a spatial resolution of 50 µm. The measured dose in the ionization chamber for irradiation of the flexible circuit board including the conductor (case 1: all layers) is shown in fig. 4.2 for the different penetration depths.

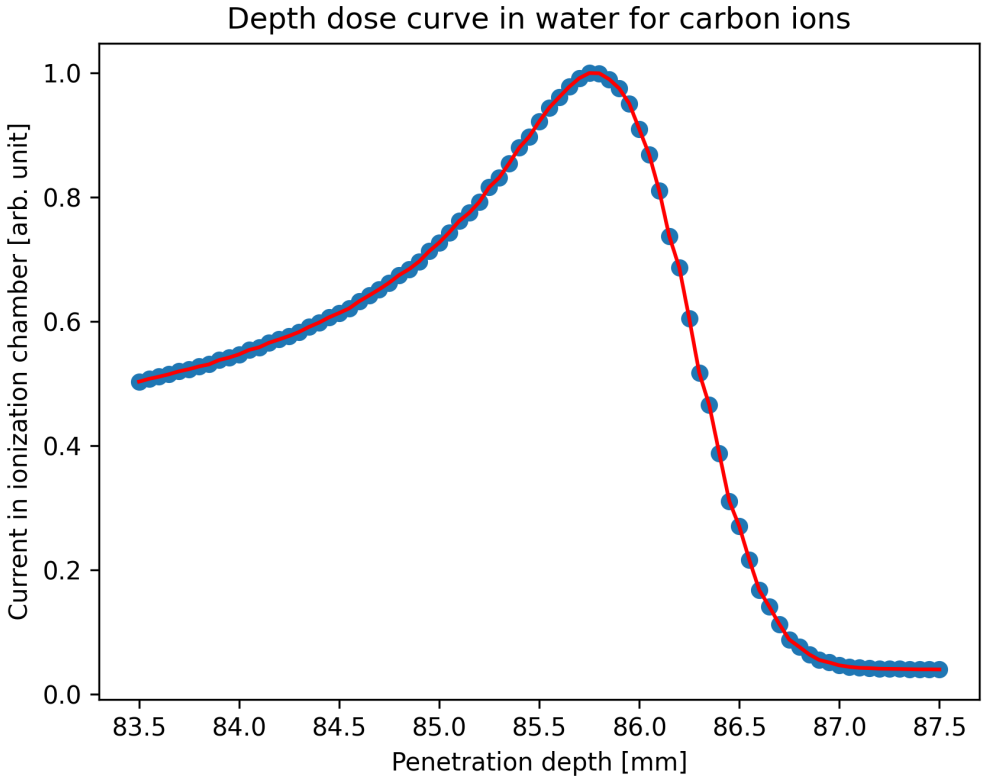

Figure 4.2: Measured depth dose curve for carbon ions in the water column during irradiation of the flexible printed circuit board including the conductor. A total of 81 individual measurements (blue) were conducted at intervals of 50 µm to investigate the depth dose at penetration depths between 83.5 mm and 87.5 mm. Linear interpolation (red) was performed between the data points to more accurately determine the width of the Bragg peak and the D_{50} value.

A linear interpolation between the 81 data points allows a more precise characterization of the Bragg peak with respect to the penetration depth in the water column and the longitudinal width along the beam axis. In particular, the position of the Bragg peak was determined both at the dose maximum and at half the dose maximum (D_{50}) towards the end of the particle range, for the described irradiation

positions (case 1: all layers, case 2: edge of conductor, case 3: no conductor, reference: air). Furthermore, the longitudinal width of the Bragg peak along the beam axis at dose values of 80 % and 90 % of the maximum dose was extracted from the interpolated data. The results of the two measurements for each irradiation position on the flexible circuit board of the RF coils are shown in table 4.3.

Table 4.3: Measured change in the peak position, the D_{50} position and the width of the Bragg peak in the depth dose curve for the irradiation of different RF coil layers in comparison to the reference measurement with no materials in front of the water column.

Measurement 1 **Change in:**	**Case 1:** **All layers**	**Case 2:** **Edge of conductor**	**Case 3:** **No conductor**
Peak position [mm]	0.45	0.35	0.25
D_{50} position [mm]	0.40	0.31	0.22
90 % peak width [mm]	-0.02[1]	0.01	-0.02[1]
80 % peak width [mm]	-0.01[1]	0.03	0.00
Measurement 2 **Change in:**	**Case 1:** **All layers**	**Case 2:** **Edge of conductor**	**Case 3:** **No conductor**
Peak position [mm]	0.40	0.35	0.25
D_{50} position [mm]	0.40	0.30	0.20
90 % peak width [mm]	-0.02[1]	0.01	-0.01[1]
80 % peak width [mm]	0.00	0.03	0.01

[1] Negative values correspond to a reduction in the peak width compared to the reference measurement.

The average of the two measurements shows a shift in the Bragg peak positions of 0.43 mm for the peak maximum and 0.40 mm for D_{50} relative to the reference measurement for the irradiation of all layers (case 1) in the flexible PCB of the RF coils. When the flexible PCB is irradiated at a position with no conductor (case 3), an average shift in the Bragg peak positions of 0.25 mm for the peak maximum and 0.21 mm for D_{50} was observed. Thus, the measurements suggest that the conductor layer is responsible for a WET of 0.18−0.19 mm (subtraction: mean(case 1) − mean(case 3)). Compared to the simulated values (all layers: $\approx$ 0.42−0.45 mm, conductor layer: $\approx$ 0.24 mm), the measurements result in similar or

slightly lower values for the WET of the flexible circuit board and the conductor layer.
Furthermore, the peak widths indicate that the coil components do not cause any scattering (range straggling) of the ion beam along the beam axis. In particular, no substantial longitudinal broadening of the Bragg peak width was observed in the partial irradiation of the heterogeneous conductor layer (case 2).
Due to the negligible influence on the particle beam in terms of ion attenuation and range straggling of the Bragg peak, the developed RF coils can be considered as radiation-transparent for particle beams.

4.2 Body coil for 1.5 T "offline" MR system

In this section the developed RF body coil is investigated in terms of RF field homogeneity, transmit power efficiency and SNR. In this context, the influence of rotation is assessed in both simulations and MR measurements to evaluate the suitability in combination with a patient rotation system. In addition, the imaging performance of the RF body coil is compared to the internal body coil of the MR scanner. Furthermore, the RF body coil is used for imaging in a heterogeneous phantom in order to visualize different image contrasts.

4.2.1 Simulated S-parameters

The S-parameters of the RF body coil at port 1 and 2 were simulated for different rotation angles ($0-360°$) with a step size of 15° including the reflection parameters (S_{11}, S_{22}) for the homogeneous torso phantom and the human voxel model at the respective ports (see fig. 4.3). As a measure of the decoupling between the two ports, the transmitted RF power (S_{21}) between the two ports was also considered.

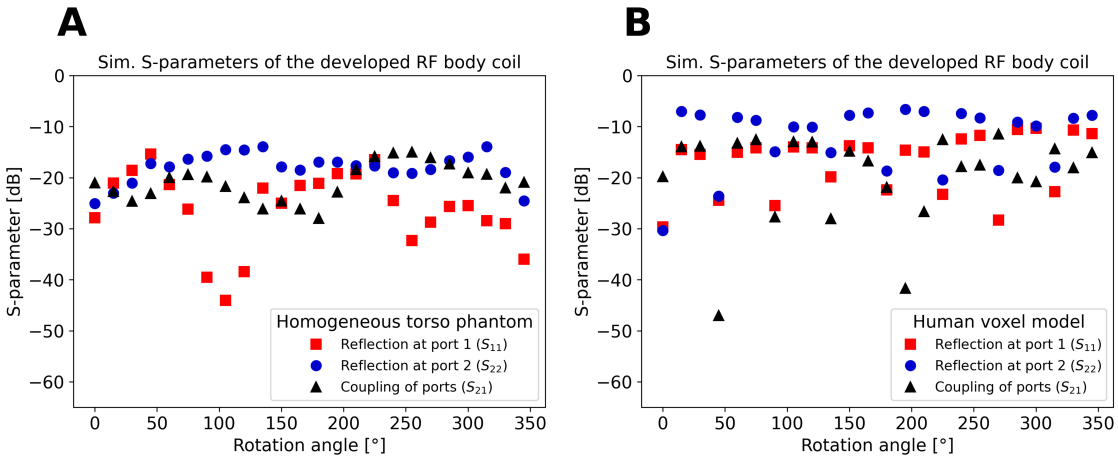

Figure 4.3: Simulated S-parameters at the two matching networks of the RF body coil for all rotation angles of the homogeneous torso phantom (**A**) and the human voxel model (**B**). This includes the reflection coefficients (S_{11}, S_{22}) as well as the power transfer between the two coil ports (S_{21}) to evaluate their coupling. The capacitor values were optimized for a horizontal position of the phantom or voxel model (0° rotation) and kept constant for all other rotation angles.

Good tuning and matching of the RF body coil was achieved for the homogeneous torso phantom with simulated S-parameters better than $-15.4\,\mathrm{dB}$ (S_{11}), $-13.9\,\mathrm{dB}$ (S_{22}) and $-14.9\,\mathrm{dB}$ (S_{21}) for all rotation angles. For the human voxel model, good tuning and matching was achieved for the horizontal position (0° rotation), however the S-parameters take values of up to $-10.6\,\mathrm{dB}$ (S_{11}), $-6.6\,\mathrm{dB}$ (S_{22}) and $-11.5\,\mathrm{dB}$

(S_{21}) across a full rotation of the voxel model. Rotation angles of multiples of 45° result in S-parameters below −19.8 dB (S_{11}), −14.9 dB (S_{22}) and −11.5 dB (S_{21}).

4.2.2 Radiofrequency field homogeneity

The RF field homogeneity of the developed RF body coil is first examined and compared to the internal body coil for two rotation angles (0°, 30°) in the central layers. Later, a more detailed evaluation of the RF field homogeneity is performed for 24 different rotation angles. To visualize the transmit and receive field distribution of the RF body coil, two MR images of the homogeneous torso phantom were acquired and the B_1 maps were calculated using the double-angle method (see section 3.4.3) for the three 2D slices at X = 0 mm, Y = 56 mm (elevated phantom position due to the integrated MR table (see fig. 3.12)) and Z = 0 mm. In addition, the B_1 maps were determined for a rotation angle of 0° and 30° of the patient rotation system. The selected parameters of the GRE sequence are listed below:

- **Slices:** Orthogonal to the x, y and z axes, a single slice with a thickness of 4 mm was selected in the center of the phantom.
- **Voxel size:** Each voxel in the image data was equal to $(4\,\text{mm})^3$.
- **Echo time (T_E):** The echo time of the GRE sequence was set to 5 ms for all conducted MR measurements.
- **Repetition time (T_R):** To avoid artifacts in the B_1 maps, an almost complete relaxation of the magnetization to the ground state is beneficial before the renewed manipulation with an RF pulse. Therefore, a repetition time of 10 s was used for all MR measurements.
- **Flip angle (FA):** For the calculation of the B_1 maps, a nominal flip angle of 60° and 120° was chosen for the two MR images of a slice using a pulse voltage of 105 V and 210 V, respectively.
- **Measurement time:** The measurement time for a 2D slice varied for the different axes and the chosen FOV depending on the position of the phantom (0°, 30°). For the phantom in horizontal position, the measurement time was 10 min 42 s in the transverse, 16 min 2 s in the coronal and 10 min 42 s in the sagittal slice. For a phantom rotated by 30°, the measurement time was 13 min 2 s in the transverse, 16 min 2 s in the coronal and 13 min 2 s in the sagittal slice.
- **FOV:** Depending on the slice and the rotation angle of the phantom, different FOV were acquired to cover the entire phantom (see table 4.4).

Table 4.4: Nominal FOV for the phantom MR measurements with the radiation-transparent RF body coil and the internal body coil for the three central slices with a phantom rotation of 0° and 30°, respectively.

Measurements	**X = 0 mm**	**Y = 56 mm**	**Z = 0 mm**
FOV (0° rotation)	384×240 mm^2	384×256 mm^2	256×256 mm^2
FOV (30° rotation)	384×312 mm^2	384×256 mm^2	312×256 mm^2

To evaluate the RF field homogeneity of the developed RF body coil, additional measurements were performed with the internal body coil of the MR scanner coil using the same sequence parameters from above. In addition, a similar FOV was chosen for the simulated 2D slices of the transmit and receive field in the center of the phantom. A comparison of the B_1 maps for the central slices in the x, y and z directions are shown in fig. 4.4 for the horizontal position of the phantom (0° rotation) and in fig. 4.5 for the rotated orientation of the phantom (30° rotation). The presented relative B_1 maps of the radiation-transparent RF coil demonstrate a high degree of homogeneity for the transmit and receive field distributions of the three slices. Moreover, a good agreement between measurement and simulation can be observed for the RF field distributions. Furthermore, the uniformity of the B_1 maps is maintained even when the RF body coil and phantom are rotated by 30°. Slight inhomogeneities in the RF field distributions can be seen in both the MR measurement and the simulation of the radiation-transparent RF body coil, especially at the edges of the homogeneous torso phantom. Similar asymmetries in the RF field distribution can be observed for the internal RF coil of the MR scanner. Comparing the transverse transmit and receive maps shows that the inhomogeneities in the RF field distributions occur at the mirrored positions along the phantom's axes. Comparable non-uniform patterns of the B_1^+ and B_1^- fields of RF coils have already been reported in the literature [Vaidya et al., 2016] [Cloos et al., 2016] for the given frequency.
A quantitative analysis of the RF field uniformity was performed by calculating the coefficient of variation (COV) in a ROI. The COV of a selected dataset corresponds to the relative variation and is defined as follows:

$$\mathrm{COV} = \frac{standard\ deviation}{mean} \tag{4.2}$$

The COV values in the rectangular ROIs (white) in the center of the 2D slices in fig. 4.4 and 4.5 provide a measure of the relative deviation (in %) of the flip angle (transmit field (B_1^+)) and the sensitivity (receive field (B_1^-)), and can be seen in table 4.5.

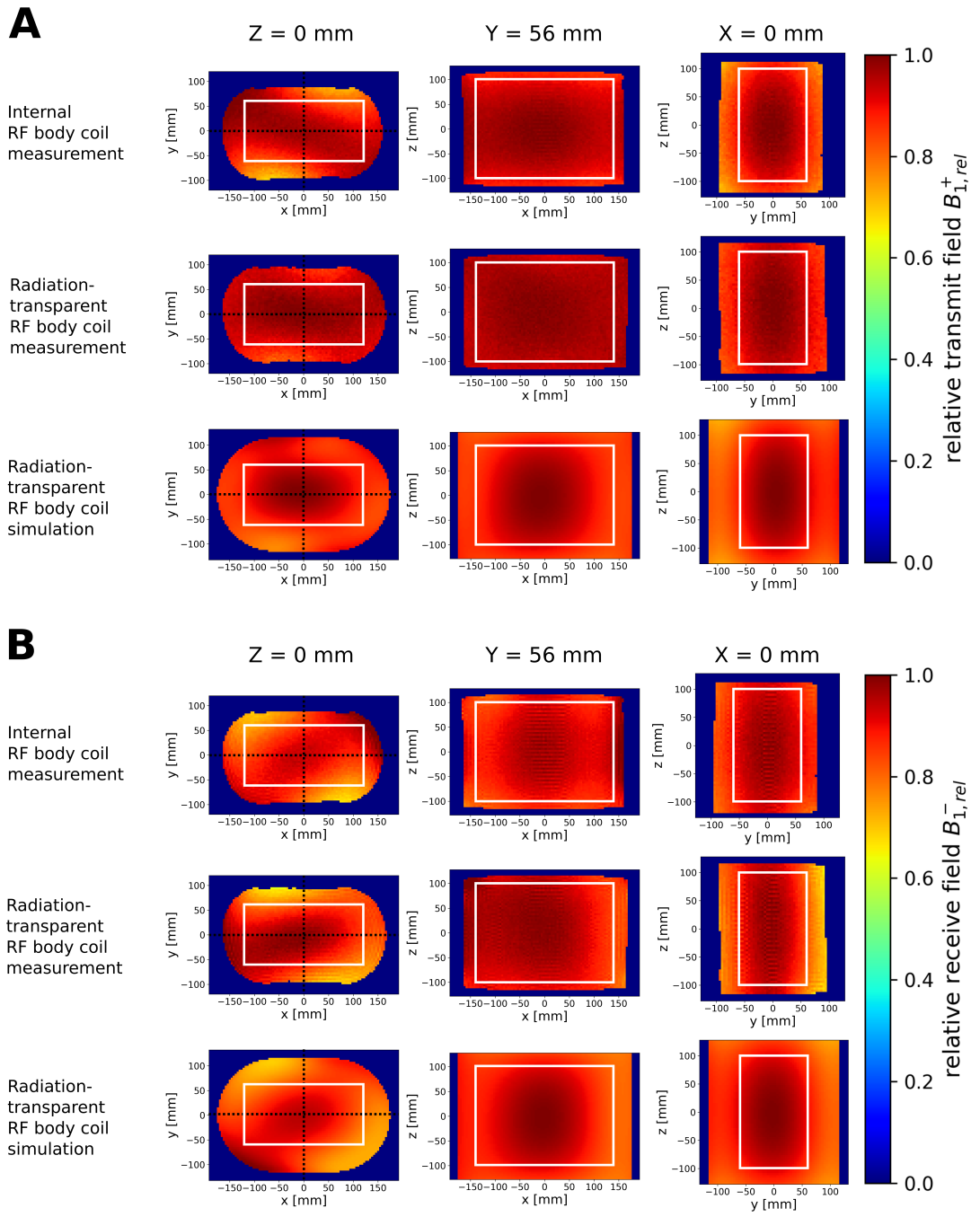

Figure 4.4: Relative transmit (**A**) and receive (**B**) field distributions for three orthogonal slices (indicated in black) at the center of the homogeneous torso phantom in horizontal position (0° rotation) obtained from the flip angle map of the radiation-transparent RF body coil and the internal body coil as well as the simulation. The simulated B_1 maps with a pixel size of $(4\,\mathrm{mm})^2$ were normalized to the maximum value, while the measured B_1 maps were normalized to the 99th percentile to exclude extreme values that can occur with the double-angle method at the edges of the phantom. In addition, a ROI (white) is shown for a quantitative analysis of the RF field homogeneity.

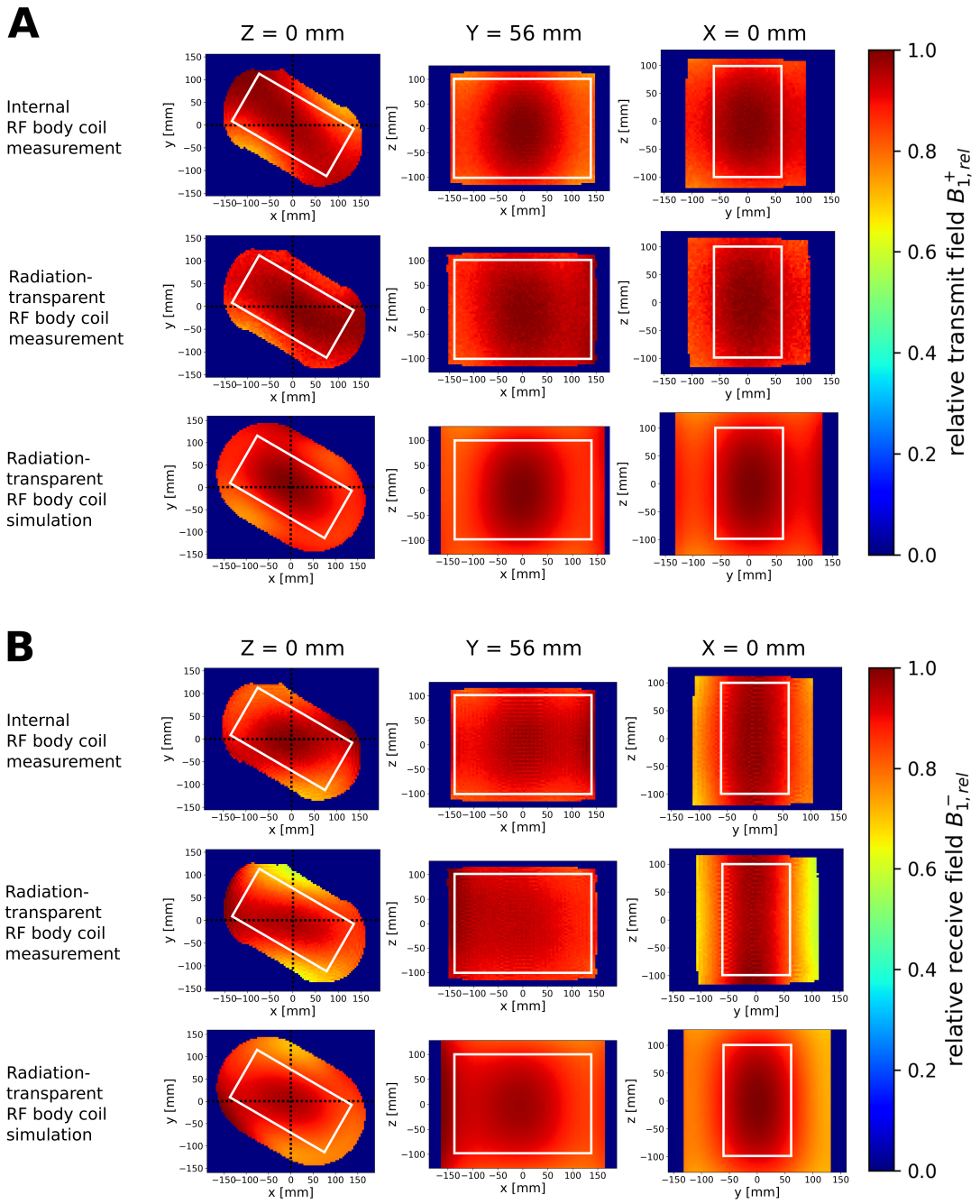

Figure 4.5: Relative transmit (**A**) and receive (**B**) field distributions for three orthogonal slices (indicated in black) at the center of the homogeneous torso phantom in a rotated position (30° rotation) obtained from the flip angle map of the radiation-transparent RF body coil and the internal body coil as well as the simulation. The simulated B_1 maps with a pixel size of $(4\,\mathrm{mm})^2$ were normalized to the maximum value, while the measured B_1 maps were normalized to the 99th percentile to exclude extreme values that can occur with the double-angle method at the edges of the phantom. In addition, a ROI (white) is shown for a quantitative analysis of the RF field homogeneity.

For the transverse slice where the phantom was rotated by 30°, the ROI was rotated by the same angle in Python (Python package: scipy.ndimage [Virtanen et al., 2020]) to better compare the COV values with the horizontal phantom position.

Table 4.5: Coefficients of variation calculated for the measured and simulated transmit (B_1^+) and receive fields (B_1^-) of the radiation-transparent RF body coil and the internal RF body coil with a homogeneous torso phantom in horizontal position and in a position rotated by 30°.

COV in % **for 0° rotation**	**Z = 0 mm** **240×120mm²**	**Y = 56 mm** **280×200mm²**	**X = 0 mm** **120×200mm²**
B_1^+, internal coil	4.6	3.0	4.3
B_1^+, rad.-transparent coil	2.4	1.6	2.9
B_1^+, sim. rad.-transp. coil	4.3	4.8	3.9
B_1^-, internal coil	5.6	3.9	3.2
B_1^-, rad.-transparent coil	6.1	4.3	5.0
B_1^-, sim. rad.-transp. coil	5.4	5.6	3.7
COV in % **for 30° rotation**	**Z = 0 mm** **240×120mm²**	**Y = 56 mm** **280×200mm²**	**X = 0 mm** **120×200mm²**
B_1^+, internal coil	4.5	6.4	3.5
B_1^+, rad.-transparent coil	3.4	4.1	2.8
B_1^+, sim. rad.-transp. coil	4.1	5.4	3.4
B_1^-, internal coil	5.8	3.6	3.6
B_1^-, rad.-transparent coil	6.6	3.6	5.2
B_1^-, sim. rad.-transp. coil	5.0	4.4	3.7

The ROI in the measured transmit fields of the radiation-transparent body coil (see fig. 4.4 A and 4.5 A) yield COV values below 3.0 % for the phantom in horizontal position and below 4.2 % for the rotated phantom, in all slices (see table 4.5). Furthermore, the transmit field homogeneity (B_1^+) of the radiation-transparent RF body coil exceeds the homogeneity of the simulated transmit field as well as the transmit field homogeneity of the internal (non-radiation-transparent) body coil of the MR scanner in all slices of the two phantom orientations.

For the homogeneity of the measured receive fields (fig. 4.4 B and 4.5 B) of the radiation-transparent coil, the COV values in the three slices remain below 6.2 % for the horizontal orientation of the phantom and below 6.7 % for the rotated orientation (see table 4.5). The receive field distributions of the developed RF body coil show a slightly lower homogeneity compared to the simulation and the internal body coil, except for the plane at Y = 56 mm. In addition, the calculated COV values of the radiation-transparent coil show an increase in RF field inhomogeneities when the phantom is rotated except for the transmit field at X = 0 mm and the receive field at Y = 56 mm.
For a more detailed examination of the RF field homogeneity of the RF body coil, additional 3D datasets were measured and the corresponding B_1 maps were calculated. Two MR image datasets were acquired for 24 different angles to evaluate the RF field homogeneity for a full rotation of the patient capsule ($0 - 360°$) in steps of 15°. In order to obtain a complete acquisition of the B_1 maps in the homogeneous torso phantom in a 3D volume for different rotation angles, the following sequence parameters of the 2D measurements were adjusted:

- **Slices:** To obtain a 3D dataset, 42 slices were measured in the z direction. The slices each have a thickness of 6 mm and are adjacent to each other without a gap.
- **Voxel size:** The voxel size has been increased to $(6\,\text{mm})^3$, which is sufficient to spatially resolve non-abrupt changes in the RF field distributions, especially for homogeneous resonators.
- **Measurement time:** The measurement time is 10 min 42 s for the complete 3D dataset with 42 slices acquired in the z direction.
- **FOV:** To cover the phantom for a full rotation of the patient capsule, the FOV was increased to 384 mm×384 mm for all rotation angles.

With proper selection of the ROI in the acquired 3D MR image datasets of the phantom measurements, the RF field homogeneity could be evaluated for the 2D slices in the central transverse, coronal and sagittal planes of the phantom. For this purpose, new ROI with slightly different dimensions were defined (transversal: $240\times120\,\text{mm}^2$, coronal: $240\times180\,\text{mm}^2$, sagittal: $120\times180\,\text{mm}^2$) and rotated according to the orientation of the phantom to compare the same slice of the phantom for different rotation angles.
In addition, the COV was also evaluated in a volume of $\Delta z = 216$ mm around the center of the phantom ($-108\,\text{mm} \leq z \leq +108\,\text{mm}$), which covers the entire phantom in the x and y directions excluding voxels outside the phantom.
Additional simulations were performed with the homogeneous torso phantom and a heterogeneous voxel model (see section 3.2.3) for the same ROI and volume ($\Delta\ z\ = 216$ mm), respectively. One simulation was performed for the homogeneous

torso phantom at the same position as in the measurement (y = Y + 56 mm) and one for the hypothetical case where the RF body coil and phantom were positioned at the isocenter of the MR scanner (y = Y) with the table removed to investigate the effect of the off-center positioning of the phantom and the radiation-transparent RF body coil on the homogeneity of the RF field (see fig. 3.12). The human voxel model was simulated with capacitor values from the homogeneous torso phantom simulation and a position above the isocenter (y = Y + 56 mm) was chosen to mimic the setup from section 3.2.2. The dependence of the COV values on the rotation angle of the phantom and the radiation-transparent RF body coil is shown in fig. 4.6.

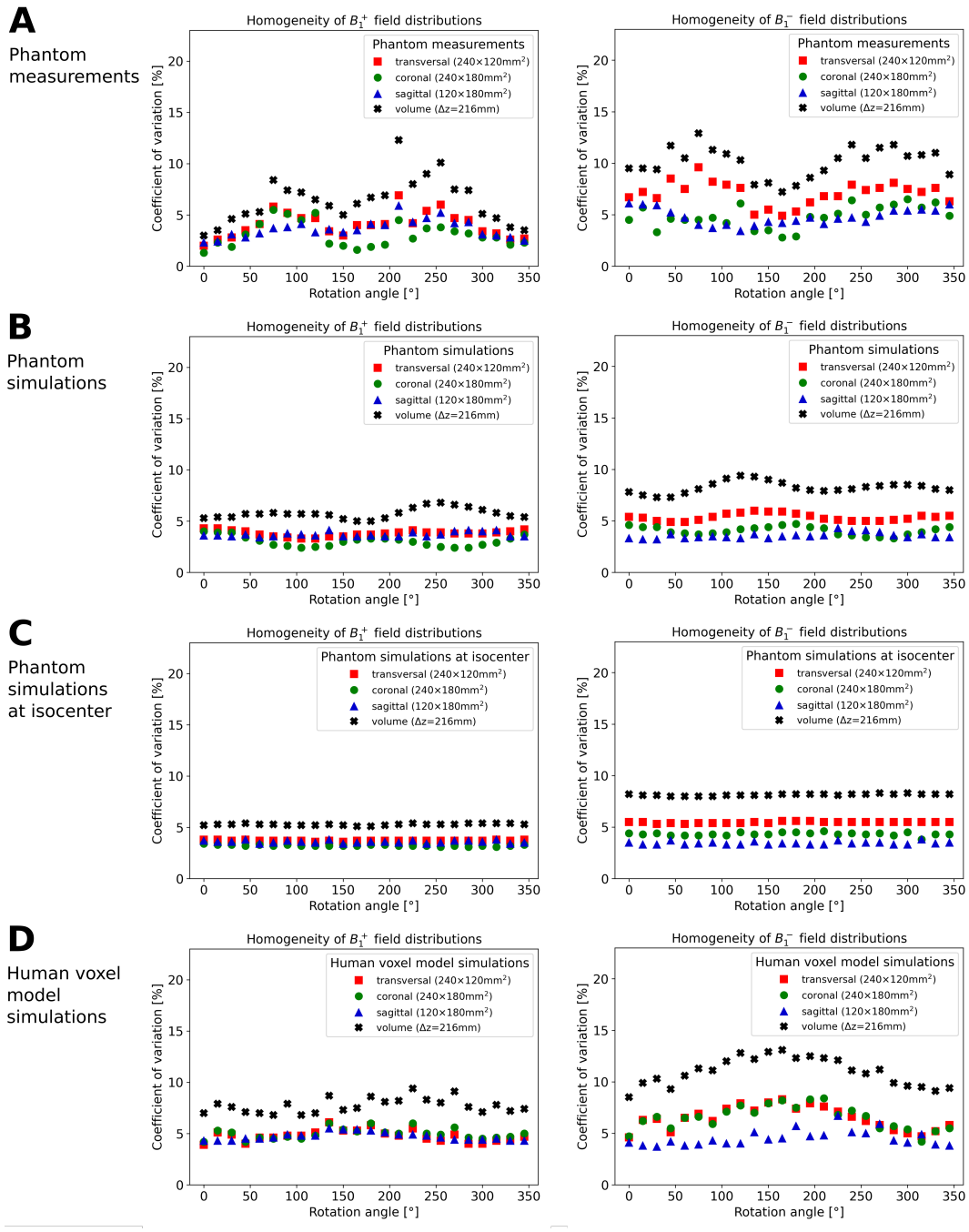

Figure 4.6: Coefficients of variation for the transmit and receive field of the radiation-transparent RF body coil calculated for a full rotation of the patient capsule (including RF coil and phantom) for the measurements with the homogeneous torso phantom (**A**), the corresponding phantom simulations (**B**), the phantom simulations with a hypothetical phantom and RF coil position in the isocenter of the MR scanner (**C**), and the simulations with the human voxel model (**D**). The COV values were determined in a ROI in the central transverse, coronal and sagittal slices of the phantom and in the whole volume for a full rotation of the patient capsule.

The evaluation of the RF field homogeneity for the phantom measurements (see fig. 4.6 A) shows an angular dependence of the COV values and a tendency to lower COV values can be observed near the rotation angles of 0° and 180° for the homogeneous torso phantom. Maximum COV values of 6.9 % (B_1^+) and 9.6 % (B_1^-) were calculated in the transverse, coronal, and sagittal slices for the 24 different rotation angles of the patient capsule. Calculation of RF field homogeneity in the entire phantom volume ($\Delta z = 216\,mm$) for all rotation angles yields COV values of 3.0−12.3 % (B_1^+) and 7.2−12.9 % (B_1^-) for the transmit and receive fields, respectively.
The evaluation of the simulated B_1 maps (see fig. 4.6 B) with the same position as in the measurement, shows an angular dependence of the field homogeneity with COV values below 4.4 % (B_1^+) and 6.1 % (B_1^-) for the three slices and COV values of 5.0−6.8 % and 7.3−9.4 % for the transmit and receive fields in the whole phantom volume ($\Delta z = 216\,mm$), respectively.
When the phantom is positioned at the isocenter of the magnet (see fig. 4.6 C), the dependence of the RF field homogeneity on the angle of rotation disappears in the simulated transmit and receive fields resulting in COV values that remain nearly constant for all rotation angles and do not exceed 6.2 % (B_1^+) and 3.8 % (B_1^-) for the slices, and 5.4 % (B_1^-) or 8.3 % (B_1^-) for the evaluated volume ($\Delta z = 216\,mm$). Compared to the homogeneous torso phantom, the heterogeneous voxel model with spatially varying dielectric properties shows higher COV values in the three slices and in the evaluated volume (see fig. 4.6 D). However, the COV values remain below 6.2 % (B_1^+) and 8.4 % (B_1^-) for all rotation angles, and do not increase above 9.1 % (B_1^+) and 13.1 % (B_1^-) for the evaluated volume ($\Delta z = 216\,mm$).
In most cases, for both the measurements and the simulations, better homogeneity was obtained for the transmitting field than for the receiving field.

4.2.3 Power efficiency

Values for the transmit power efficiency (see section 2.3.8) of the radiation-transparent RF body coil were determined from the relative B_1^+ maps for different rotation angles and compared to the simulation. The average power of the RF pulse (P_{RF}) with a pulse length of $t_{pulse} = 1\,ms$ was calculated for a nominal flip angle of $\alpha = 60°$ using the reference voltage ($U_{ref} = 315\,V$) and the impedance of $Z_0 = 50\,\Omega$:

$$P_{RF} = \frac{U_{pulse}^2}{50\,\Omega} \tag{4.3}$$

$$P_{RF} = \left(\frac{U_{ref} \cdot \alpha \cdot 1\,ms}{180° \cdot t_{pulse}}\right)^2 \cdot \frac{1}{50\,\Omega} \tag{4.4}$$

Subsequently, the measured transmit power efficiency ($\frac{B_1^+}{\sqrt{P_{RF}}}$ in $\frac{\mu T}{\sqrt{W}}$) could be calculated for the homogeneous torso phantom using the measured flip angle map of the transmit field (α_{map}) (see eq. 2.31):

$$\frac{B_1^+}{\sqrt{P_{RF}}} = \frac{\alpha_{map}}{\gamma_{\mathrm{H}} \cdot t_{pulse} \cdot \sqrt{P_{RF}}} \tag{4.5}$$

The simulated transmit field for the homogeneous torso phantom in the elevated (y = Y + 56 mm) and isocentric (y = Y) positions and the heterogeneous human voxel model were normalized to 1 W stimulated power. To calculate the simulated transmit power efficiency, the measured losses in the transmit/receive switch (see table 3.3) and the quadrature hybrid (see table 3.4) as well as the measured phase shift and the imperfect matching of the coil ports (see table 3.2) were taken into account for each simulation.
The measured and simulated average transmit power efficiencies in the ROI (240 mm × 120 mm) of the transverse slice of the phantom are shown in fig. 4.7 for the different rotation angles.

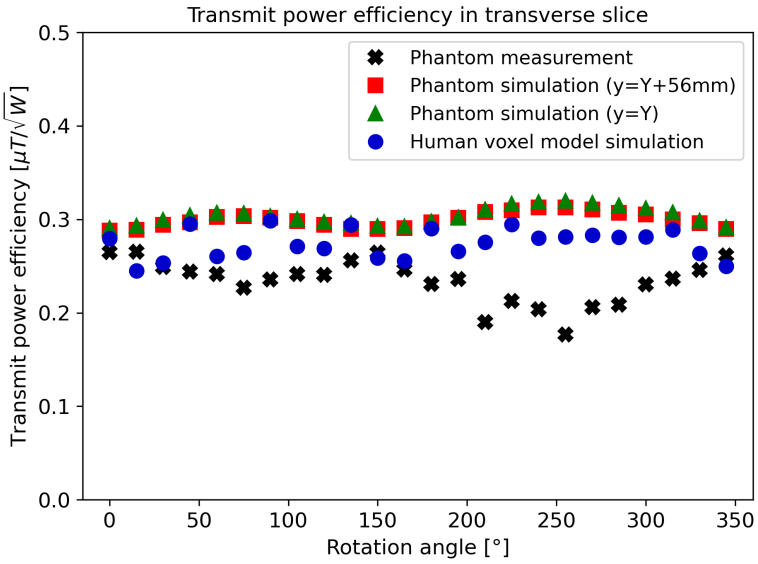

Figure 4.7: The measured and simulated transmit power efficiencies of the radiation-transparent RF body coil in the homogeneous torso phantom and the heterogeneous human voxel model. The transmit power efficiency was evaluated in the entire transverse slice in the center of the phantom for a full rotation of the patient capsule.

The mean transmit power efficiency of the radiation-transparent RF body coil varies between $0.18\frac{\mu T}{\sqrt{W}}$ and $0.27\frac{\mu T}{\sqrt{W}}$ for the measurements at different rotation angles of the phantom and RF coil. The simulated transmit power efficiencies are ranged between $0.29\frac{\mu T}{\sqrt{W}}$ and $0.31\frac{\mu T}{\sqrt{W}}$ for the phantom in elevated position (y = Y + 56 mm), between $0.29\frac{\mu T}{\sqrt{W}}$ and $0.32\frac{\mu T}{\sqrt{W}}$ for the phantom at the isocenter of the magnet (y = Y), and between $0.24\frac{\mu T}{\sqrt{W}}$ and $0.30\frac{\mu T}{\sqrt{W}}$ for the human voxel model across all rotation angles.

Overall, the measured transmit power efficiency for the homogeneous torso phantom remains below the simulated one for every single rotation angle.

4.2.4 Signal-to-noise ratio

The imaging properties of the radiation-transparent RF body coil as a receiving coil were investigated in terms of SNR and compared to the internal body coil. For this purpose, the signal intensities inside the phantom and the standard deviation of the noise outside the phantom (see section 3.4.4) were determined for each rotation angle of the phantom and the absolute SNR was calculated according to eq. 2.52 and eq. 3.9. The whole phantom (in the x and y directions) was analyzed in three different volumes ($\Delta z = 60\,\text{mm}$, $\Delta z = 120\,\text{mm}$, $\Delta z = 216\,\text{mm}$) centered along the z axis. The measured SNR values for the different rotation angles are shown in fig. 4.8.

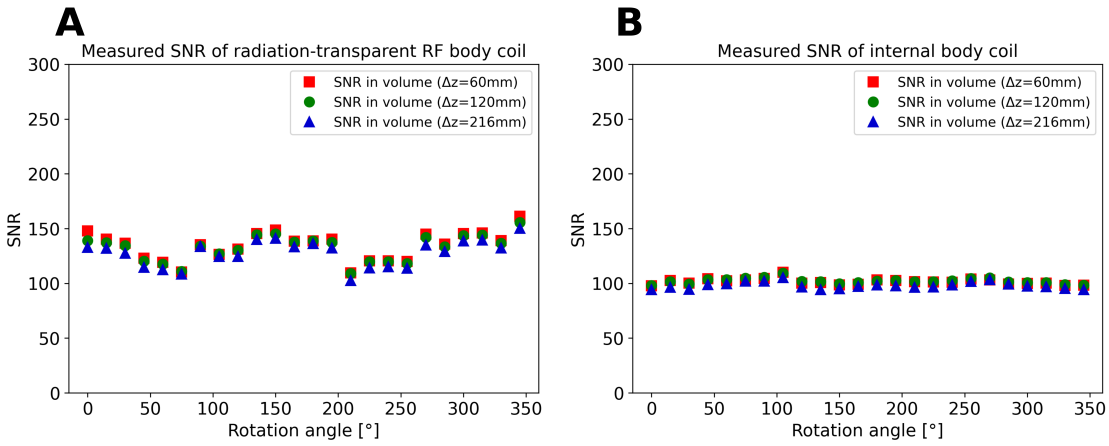

Figure 4.8: Comparison of the measured SNR for the radiation-transparent RF body coil and the internal body coil of the MR scanner. The SNR was studied in three subvolumes of different sizes ($\Delta z = 60\,\text{mm}$, $\Delta z = 120\,\text{mm}$, $\Delta z = 216\,\text{mm}$) in the homogeneous torso phantom for a full rotation of the patient capsule. The radiation-transparent RF body coil is rotated together with the patient capsule.

While the internal body coil achieves almost constant SNR values for the different angles of rotation, a slight angular dependence can be observed with the radiation-transparent RF body coil. The SNR values of the radiation-transparent RF body coil are $110 - 161$ ($\Delta z = 60\,\text{mm}$), $109 - 156$ ($\Delta z = 120\,\text{mm}$), and $103 - 150$ ($\Delta z = 216\,\text{mm}$), exceeding those of the internal body coil (internal coil: $\text{SNR}_{\Delta z=60\,\text{mm}}$: $98 - 105$, $\text{SNR}_{\Delta z=120\,\text{mm}}$: $98 - 105$, $\text{SNR}_{\Delta z=216\,\text{mm}}$: $94 - 105$) at every angle of rotation for every volume. The choice of different volumes for calculating the average signal intensity has little effect on the SNR, although slightly higher SNR values can be obtained for the smaller volumes.

4.2.5 Safety assessment

In order to evaluate the RF safety of the RF body coil, both the SAR limits according to table 2.1 and the corresponding maximum allowed transmit power (see eq. 3.3) were calculated in a heterogeneous human voxel model. The SAR and RF power limits are shown in fig. 4.9 for normal and first level operation mode for all rotation angles of the patient capsule.

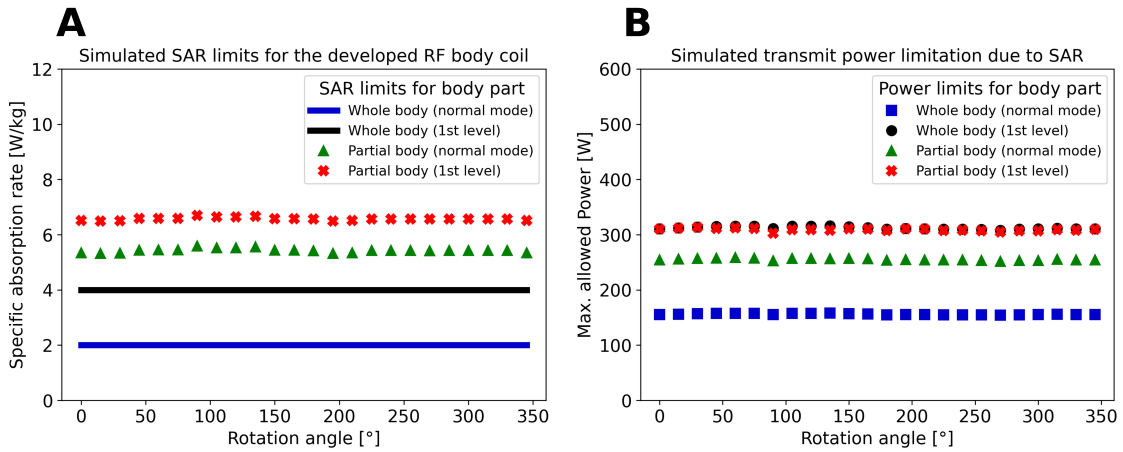

Figure 4.9: SAR limits (**A**) and the corresponding maximum allowable average RF power (**B**) of the developed RF body coil. The SAR limits specified here result from table 2.1 where the SAR limits for the partial body SAR, depend on the evaluated partial body mass. RF power limits were determined from the simulated accepted tissue power and the evaluated (partial) body mass in normal and first level modes of operation for a full rotation of the human voxel model.

The SAR and power limits remain nearly constant for all angles of rotation of the RF body coil. Comparing the whole body SAR and the partial body SAR, the RF power in normal operation mode is more limited by the whole body SAR which corresponds to a maximum average RF power of $\approx 155\,\mathrm{W}$. For the first level operating mode, both the whole body SAR and the partial body SAR limit the maximum average RF power to $\approx 310\,\mathrm{W}$.

4.2.6 Application in anthropomorphic phantom

To demonstrate that the RF body coil can achieve different image contrasts, MR measurements were performed on a heterogeneous torso-sized phantom (see fig. 3.11). The phantom is filled with substances with different relaxation times (T_1, T_2) to realistically represent organs in the human body. For the MR measurements with the RF body coil, the phantom was positioned on a pad and fixed in the patient capsule with vacuum mattresses (see fig. 3.8). MR images were then acquired with a T_1-weighted GRE (Volumetric Interpolated Breathhold Examination

(VIBE)-Dixon: opposed-phase) sequence and a T_2-weighted SE (BLADE) MR sequence. The coronal slices for the two MR sequences were displayed and exported using a DICOM reader software (Medical Imaging Interaction Toolkit (MITK), version: 2023.04 [Nolden et al., 2013] [Wolf et al., 2005]) and are shown in fig. 4.10 for two different rotation angles (0°, 90°) of the patient capsule.

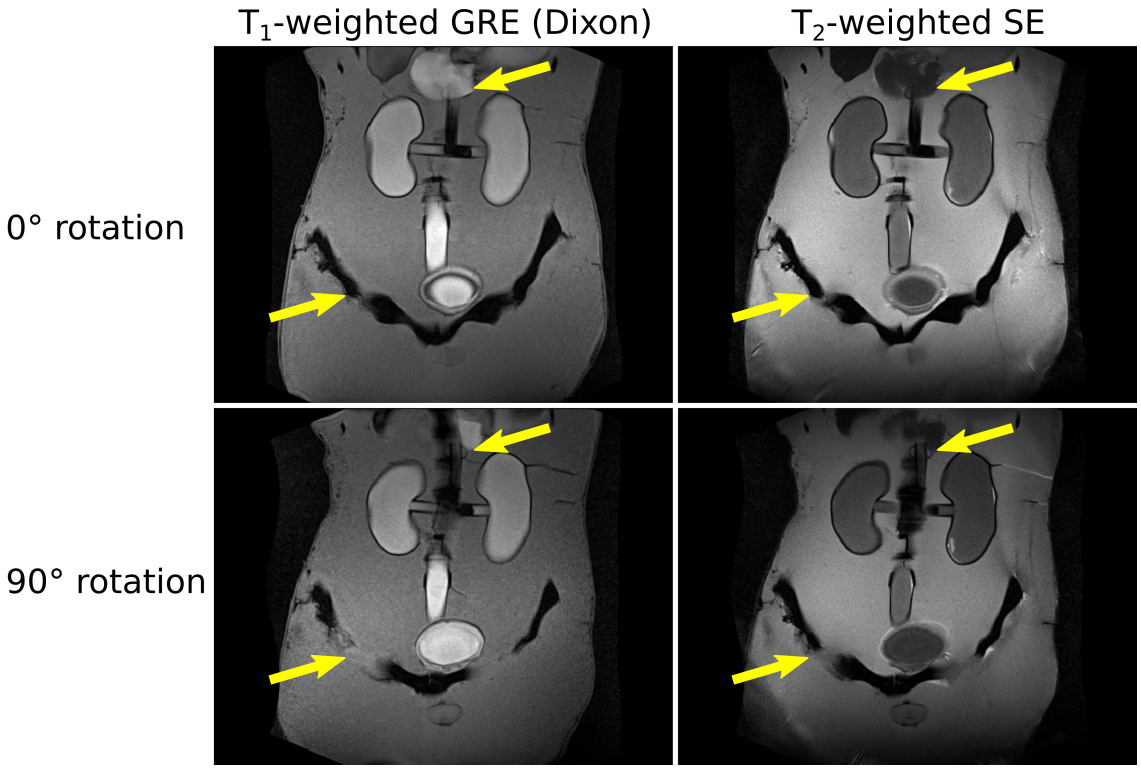

Figure 4.10: MR images for a coronal slice of a heterogeneous torso-sized phantom (see fig. 3.11) filled with organ-simulating substances. The MR images were acquired with the radiation-transparent RF body coil for two different rotation angles of the patient capsule (0° and 90°). To visualize the organ-simulating substances with different relaxation times (T_1, T_2), different contrasts could be realized with a T_1-weighted Dixon MR sequence (here shown: opposed-phase image and a T_2-weighted BLADE MR sequence. Deformation and displacement of structures in the torso-sized phantom are indicated (yellow).

The kidney-like and bladder-like structures can be visualized in different contrasts and MR imaging was also performed with the phantom rotated by 90°. Small changes in the MR images indicate an expected deformation or displacement of the organ-like structures due to gravity.

4.3 Calf coil for 0.25 T "online" MR system

In this section, the imaging characteristics of the developed RF calf coil are evaluated. This includes the investigation of the simulated S-parameters at the port of the RF calf coil as well as the homogeneity of the simulated receive fields and a comparison of the measured SNR for the developed RF calf coil and two commercial receive coils. In addition, in vivo MR images were acquired.

4.3.1 Simulated S-parameters

Similar to section 4.2.1, the reflection coefficient (S_{11}) of the RF calf coil port was simulated for each angle of rotation of the homogeneous calf phantom and the human calf voxel model (see fig. 4.11).

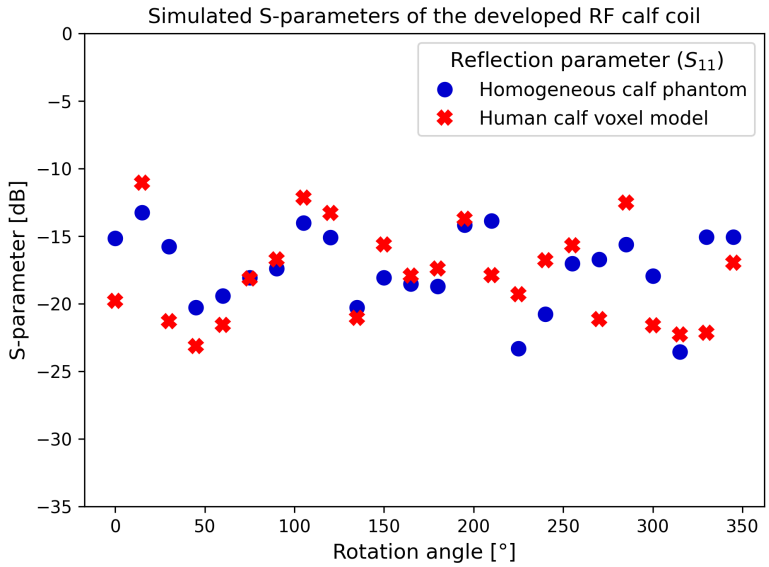

Figure 4.11: Simulated reflection coefficient at the matching network of the RF calf coil determined for all rotation angles of the RF calf coil including the homogeneous calf phantom and the human voxel model.

The reflection coefficient across all angles of rotation of the RF calf coil remains better than −13.2 dB and −11.0 dB for the homogeneous calf phantom and the human calf model, respectively.

4.3.2 Receive field homogeneity

Similar to section 4.2.2, the homogeneity of the simulated receive fields (B_1^-) of the radiation-transparent receive-only RF calf coil was evaluated in a cylindrical homogeneous calf phantom and a voxel model of a calf (see fig. 3.10). In both cases, the receive field homogeneity was simulated for a full rotation ($0 - 360°$) of the phantom or voxel model including the RF calf coil in steps of 15°. For the horizontal position (0° rotation), the simulated relative receive field distributions in the central transverse, coronal, and sagittal slices of the phantom and voxel model are shown in fig. 4.12.

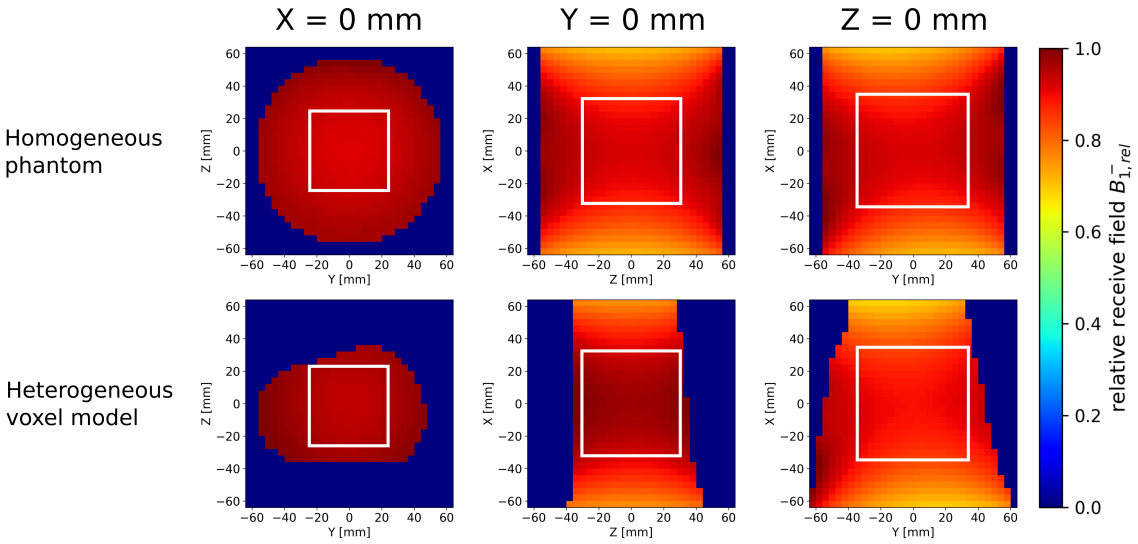

Figure 4.12: Simulated relative receive field distributions for the central transverse, coronal and sagittal in a cylindrical homogeneous phantom and a heterogeneous voxel model of a human calf (see fig. 3.10) in horizontal position (0° rotation). The receive sensitivity maps of the RF calf coil with a pixel size of $(4\,\mathrm{mm})^2$ were normalized relative to the maximum value in each slice. In addition, the ROI for a quantitative analysis of the receive field homogeneity is indicated (white).

The presented relative B_1^- maps of the radiation-transparent RF calf coil demonstrate a high degree of homogeneity in the receive sensitivity profile of the three orthogonal slices in both the phantom and the voxel model. Slight asymmetries in the receive field distribution can be observed in the sagittal (Y = 0 mm) and especially in the coronal slice (Z = 0 mm) of the homogeneous phantom.
For a quantitative assessment of the RF field homogeneity, COV values were calculated according to eq. 4.2 in a ROI (see fig. 4.12) in the central transverse ($48\times48\,\mathrm{mm}^2$), coronal ($72\times72\,\mathrm{mm}^2$) and sagittal ($64\times64\,\mathrm{mm}^2$) slices, and in a volume ($-64\,\mathrm{mm} \leq \mathrm{X} \leq +64\,\mathrm{mm}$ and complete Y and Z range) around the phantom center. The COV values in the ROI are shown in fig. 4.13, for a full rotation of the RF calf coil in increments of 15°.

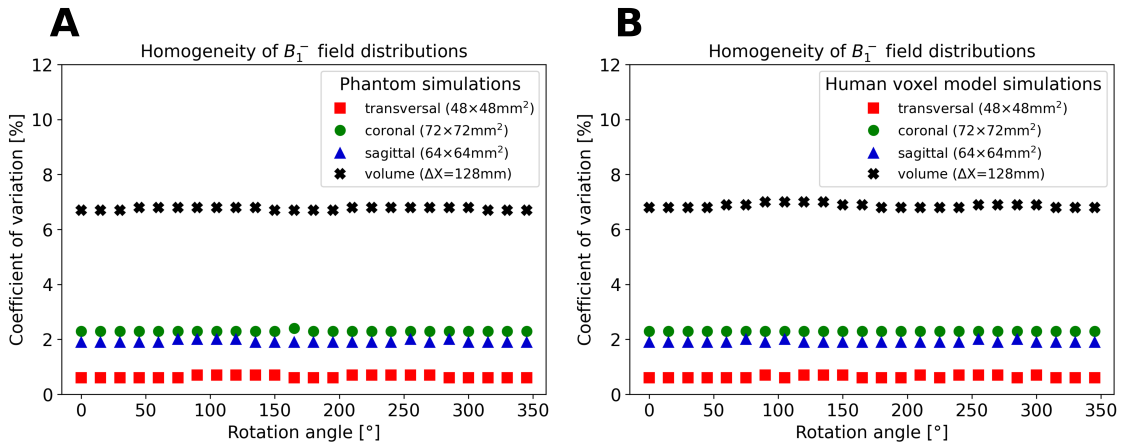

Figure 4.13: Coefficient of variation for the receive field of the radiation-transparent RF calf coil calculated in a ROI (see fig. 4.12) in a homogeneous cylindrical phantom (**A**) and a voxel model of a human calf (**B**) for a complete rotation of the RF calf coil and phantom. The ROI was rotated accordingly so that the COV could be determined in the same central transverse, coronal and sagittal slices. In addition, the COV was calculated in the entire phantom volume.

In both the homogeneous calf phantom and the voxel model, the COV values for the receive field remain below 0.8 % in the central transverse, 2.5 % in the coronal, and 2.1 % in the sagittal slices, for all rotation angles of the RF coil. The increased COV values of up to 7.0 % for the receive field in a volume of the homogeneous calf phantom or voxel model reveal larger inhomogeneities towards the edges of the phantom.

4.3.3 Signal-to-noise ratio

To characterize the radiation-transparent RF calf coil in terms of SNR, MR images were acquired using a GRE sequence with the following parameters:

- **Slices:** 42 slices each with a thickness of 2.5 mm were obtained along each axis (X, Y, Z). Only the three central slices were used for the SNR comparison.
- **Spatial resolution:** A spatial resolution of $(2.5\,\mathrm{mm})^2$ was chosen, corresponding to an image size of 128×128 pixels.
- **Echo time (T_E):** The echo time of the GRE sequence has been set to 16 ms.
- **Repetition time (T_R):** A repetition time of 1.6 s was used for the SNR measurements.
- **Flip angle (FA):** A nominal flip angle of 90° was chosen to achieve maximum signal intensity in the MR images.

- **Measurement time:** The total measurement time for all 42 slices along one axis was 3 min 30 s.
- **FOV:** The FOV corresponds to $320 \times 320\,\mathrm{mm}^2$ in the transverse, coronal and sagittal slices of the phantom.

MR images in the central transverse, sagittal, and coronal slices of the homogeneous calf phantom, acquired with the radiation-transparent RF calf coil and the commercial cervical coil as well as the commercial knee coil are shown in fig. 4.14.

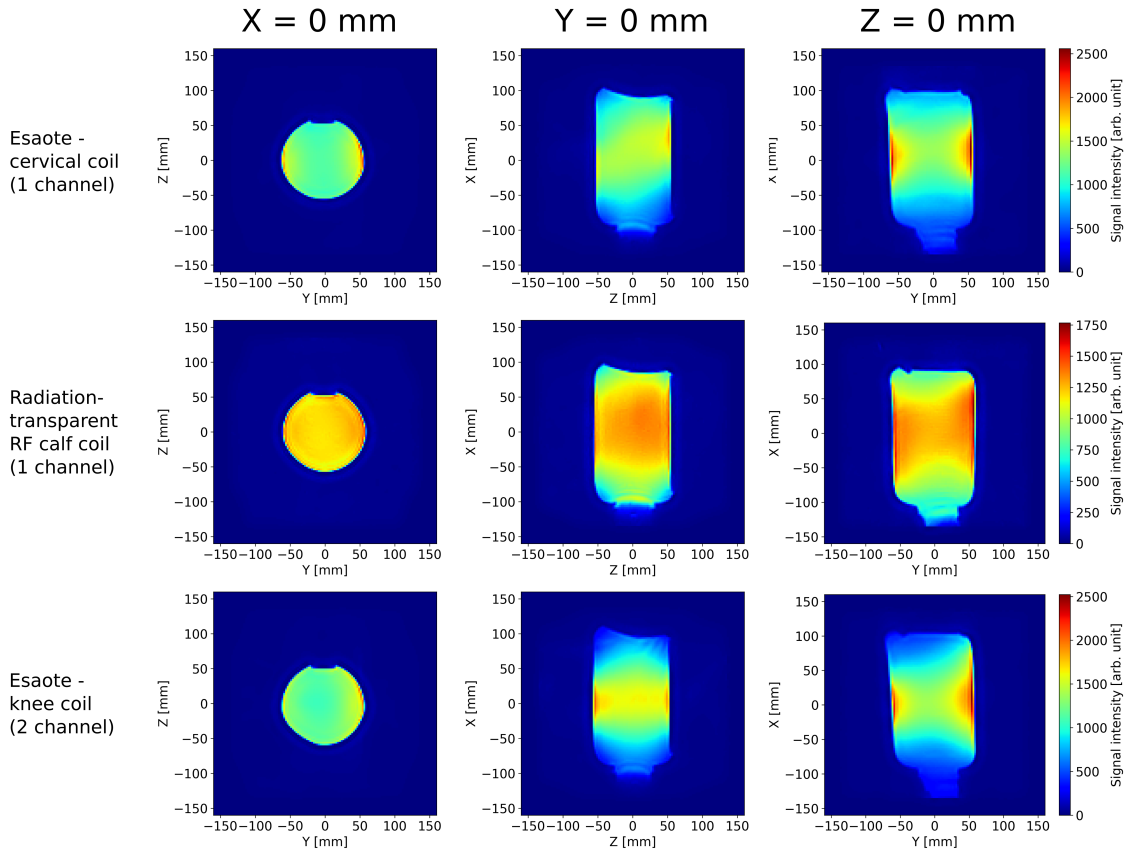

Figure 4.14: MR images in the transverse (X = 0 mm), sagittal (Y = 0 mm), and coronal (Z = 0 mm) slices at the center of the homogeneous calf phantom acquired with the radiation-transparent RF calf coil, the commercial cervical coil, and the commercial knee coil. The signal intensity in the phantom demonstrates high homogeneity of the receive sensitivity profile for the radiation-transparent RF calf coil as well as the large FOV compared to the commercial RF coils. Each MR image was acquired separately. MR images were scaled to the maximum intensity value within the three slices for each RF coil. For high |X| values, artifacts occur due to non-linear gradients of the MR scanner.

Comparing the signal intensity of the three RF coils in the measured 2D images in the center of a homogeneous calf phantom, a considerably more uniform signal

intensity distribution was achieved for the radiation-transparent RF calf coil than for the two commercial RF coils, suggesting a more homogeneous receive sensitivity profile over a larger FOV.

To better compare the three coils in absolute intensity values, a line plot of the signal intensity along each central axis of the phantom is shown in fig. 4.15.

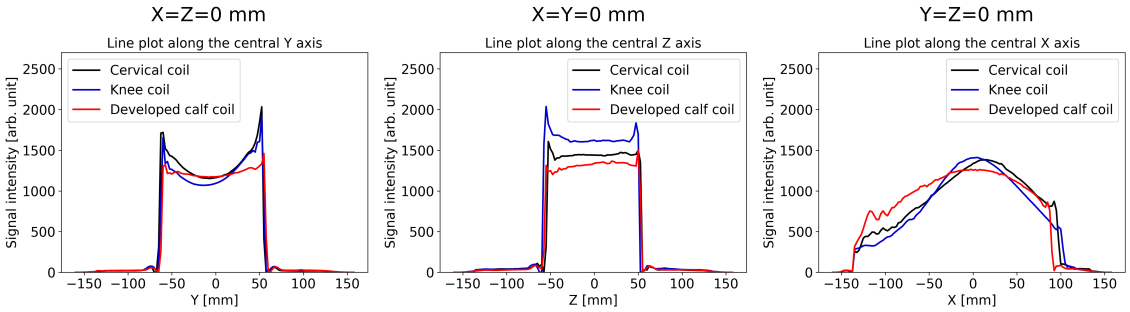

Figure 4.15: Line plots of the signal intensity in the homogeneous calf phantom along each central axis for the radiation-transparent RF calf coil, the commercial cervical coil, and commercial knee coil. The line plots show the signal intensity with 128 measured voxels, each with a slice thickness of 2.5 mm.

The comparison between the three different RF coils shows a slightly lower signal intensity for the radiation-transparent RF calf coil compared to the commercial coils in the center of the calf phantom along the central z axis, and toward the edges of the phantom along the X and Y axis. However, along the X axis away from the center, the signal intensity of the radiation-transparent RF calf coil exceeds the signal intensity of the commercial coils.

To better assess the imaging characteristics of the RF coils, a quantitative analysis of the SNR was performed using masks to define one ROI for the calculation of the mean signal in the phantom and one for the noise in the background of the image, as described in section 3.4.4. For the noise ROI, an upper and lower threshold was defined to exclude voxels in the phantom as well as the "noiseless" region at the edge of the acquired FOV, which is visible in all MR images (see fig. 4.14) The corresponding average signal intensity in a ROI inside the phantom, the image noise (see eq. 3.9) in a ROI outside the phantom, and the SNR of the three RF coils were evaluated in each slice and are shown in table 4.6. Furthermore, the coefficient of variation (see eq. 4.2) of the signal intensity inside the phantom ROI was calculated for each slice.

Table 4.6: Average signal intensity, coefficient of variation (COV), image noise and SNR of the radiation-transparent RF calf coil and of the two commercial RF coils calculated in a ROI for the measured three central slices in the homogeneous calf phantom (see fig. 4.14).

Average signal intensity in ROI	**X = 0 mm**	**Y = 0 mm**	**Z = 0 mm**
Esaote - Cervical coil	1252	1163	1164
Radiation-transparent RF calf coil	1194	1162	1154
Esaote - Knee coil	1242	1136	1141
COV in ROI in %	**X = 0 mm**	**Y = 0 mm**	**Z = 0 mm**
Esaote - Cervical coil	14.4	24.1	28.9
Radiation-transparent RF calf coil	7.5	13.6	15.4
Esaote - Knee coil	13.0	32.6	33.7
Image noise in background	**X = 0 mm**	**Y = 0 mm**	**Z = 0 mm**
Esaote - Cervical coil	10.46	15.49	14.94
Radiation-transparent RF calf coil	6.54	12.96	9.86
Esaote - Knee coil	9.85	15.27	14.17
SNR for imaging coils	**X = 0 mm**	**Y = 0 mm**	**Z = 0 mm**
Esaote - Cervical coil	120	75	78
Radiation-transparent RF calf coil	183	90	117
Esaote - Knee coil	126	74	81

The considered RF coils achieve similar values for the average signal intensity in the ROI and the COV values inside the phantom confirm a substantially higher homogeneity of the signal intensity distribution for the MR image of the radiation-transparent RF calf coil compared to the two commercial coils. Furthermore, the image noise for the MR images acquired with the radiation-transparent RF calf coil in combination with the developed preamplifier (see section 3.3.3) is considerably lower than for the commercial coils. Consequently, the SNR of the radiation-transparent RF calf coil shows an increase of $\approx 50\,\%$ in the transverse (X = 0 mm), $\approx 20\,\%$ in the sagittal (Y = 0 mm), and $\approx 50\,\%$ in the coronal (Z = 0 mm) slice compared to the commercial RF coils.

4.3.4 In vivo imaging

To verify the imaging properties of the RF calf coil with respect to the achievable image contrast for heterogeneous tissue, in vivo measurements were performed. 2D slices of a human calf were acquired in transverse, coronal and sagittal slices. MR images of a human hand were taken to demonstrate the applicability of the RF calf coil on the hand and wrist, for example. The 2D imaging parameters for the transverse, coronal, and sagittal slices using a T_1-weighted spin echo and a T_2-weighted gradient echo (Dixon) sequence are given in table 4.7.

Table 4.7: MR sequence parameters for 2D in vivo imaging of a human calf and hand using a T_1-weighted spin echo and a T_2-weighted gradient echo (Dixon) sequence.

Sequence parameter	**T_1-weighted SE**	**T_2-weighted GRE**
Slices	1	1
Slice thickness	5 mm	5 mm
Voxel size	0.98×0.98 mm^2	0.98×0.98 mm^2
Echo time (T_E)	20 ms	14 ms / 28 ms[1]
Repetition time (T_R)	500 ms	500 ms
Flip angle (FA)	90°	90°
Measurement time	2 min 12 s	2 min 12 s
FOV	250 mm×250 mm	250 mm×250 mm

[1] Various image contrasts (in-phase, opposed-phase, water-only, fat-only) were obtained from two MR images with different echo times [Dixon, 1984].

The in vivo data measured with the RF calf coil using the sequence parameters from table 4.7 are shown in fig. 4.16 and fig. 4.17 in a human calf and hand, respectively. The T_1-weighted and T_2-weighted MR images in fig. 4.16 provide insights into the structure of the human calf. In particular, the cortical bone and bone marrow of the tibia are clearly distinguishable from the rest of the tissue in the transverse and coronal slices, while individual muscles and a marginal layer of subcutaneous fat are visible in all slices. In addition, some veins are visible, particularly in the transverse slice of the water-only image. The bone marrow within the fibula was not observed in the transverse slice.
Fig. 4.17 shows the complex structure of the hand, including the finger bones, carpal bones, and adjacent joints and muscles. Especially in the coronal slice, the different tissue types can be distinguished and various image contrasts (T_1, T_2) are visible.

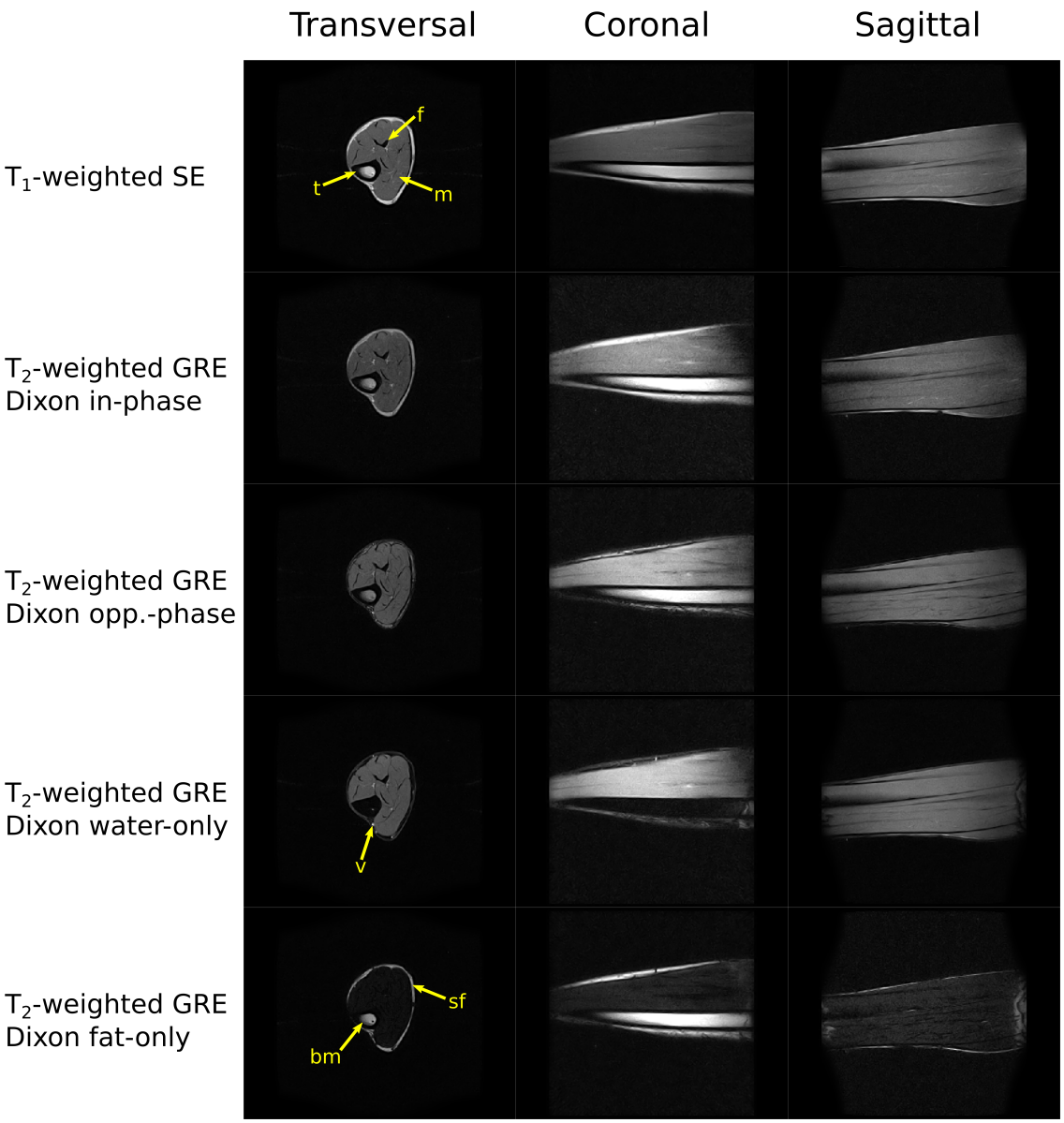

Figure 4.16: In vivo images of a human calf illustrating different image contrasts (T_1-weighted, T_2-weighted). The MR images were acquired with the RF calf coil in transverse, coronal and sagittal slices using a spin echo (SE) and a gradient echo (GRE) sequence. The Dixon method results in four different contrasts (in-phase, opposed-phase, water-only, fat-only) for the T_2-weighted GRE sequence. Different tissue types (t: tibia, bm: bone marrow, m: muscle, sf: subcutaneous fat, f: fibula, v: vein) are indicated.

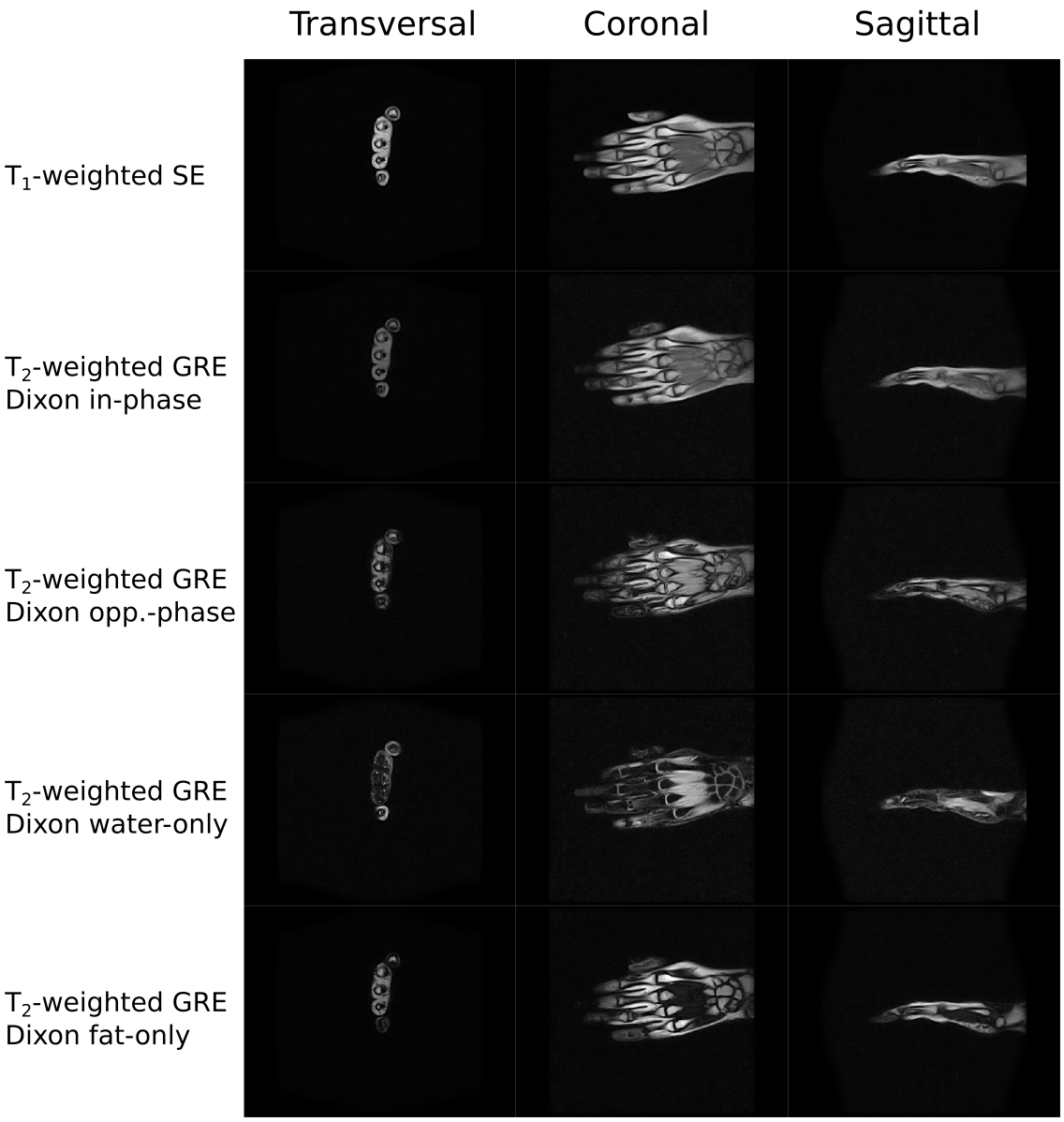

Figure 4.17: In vivo images of a human hand illustrating different image contrasts (T_1-weighted, T_2-weighted). The MR images were acquired with the RF calf coil in transverse, coronal and sagittal slices using a spin echo (SE) and a gradient echo (GRE) sequence. The Dixon method results in four different contrasts (in-phase, opposed-phase, water-only, fat-only) for the T_2-weighted GRE sequence.

Chapter 5

Discussion

The aim of this work was to develop radiofrequency coils suitable for MR-guided particle therapy with the concept of flexible treatment using a patient rotation system. In this context, two rotatable imaging coils with high radiation transparency were designed.

In a first step, the radiation transparency of the coil components was calculated and experimentally determined for a particle beam in a water column. The corresponding dose distribution showed negligible ion attenuation by the coil components, thus demonstrating compatibility for use in particle therapy.

In a second step, the transmit and receive characteristics of the developed RF body coil for the 1.5 T "offline" MR system were analyzed and evaluated in EM field simulations and MR measurements for different rotation angles of the RF body coil. Homogeneous transmit and receive field distributions in a large FOV and a high signal-to-noise ratio compared to the internal body coil of the MR scanner were demonstrated. In addition, the transmit power efficiency of the developed body coil was determined in simulations and MR measurements and the maximum allowable transmit powers in vivo were calculated in EM field simulations based on SAR limits.

In a third step, the homogeneity of the receive field for the developed receive-only RF calf coil for the 0.25 T "online" MR system was investigated in EM field simulations. To evaluate the imaging quality of the implemented RF coil setup, the SNR of the RF calf coil was quantified and compared with commercial receive coils. In vivo measurements demonstrated the applicability in human extremities and the high image contrast that could be achieved for different MR sequences.

In the following sections, the results of the particle irradiation of the coil components and the imaging characteristics of the two developed RF coils as well as the performance of the additional hardware components used in this thesis are discussed and evaluated.

5.1 Radiation transparency for particles

For the combination of MR imaging and radiotherapy, the integration of the MR system and the radiotherapy table in a single unit, e.g. an MR-linac [Klüter, 2019], offers the greatest benefit in terms of treatment options, allowing adaptive therapy with interfractional modifications to the treatment plan or real-time gating based on patient positioning and anatomical changes during the course of treatment. In MR imaging, a combination of two RF coils is often used: a large volume coil to manipulate the macroscopic magnetization of the nuclei in the patient, and a local surface coil close to the patient for optimal signal acquisition with high signal-to-noise ratio (SNR). In general, coil components with a high density (coil housing, capacitors, cables, preamplifiers, ...) can have a negative influence on the treatment quality if they are located in the beam path. Therefore, RF coils are preferably designed without rigid housing, using low-density materials (e.g., foam) to minimize ion attenuation [Zijlema et al., 2019]. While the effect of commercially available standard imaging coils on dose delivery is less problematic for conventional photon irradiation [Hoogcarspel et al., 2013], particle beams are more sensitive to non-homogeneous materials in the therapy plan due to their locally limited dose distribution (Bragg peak) which highly depends on the material in the beam path [Jäkel, 2009]. Consequently, when designing RF coils for MR-guided particle therapy, special attention must be paid to the coil configuration and the radiation transparency of the coil components.

5.1.1 Coil components

For particle irradiation, homogeneous materials in the path of the particle beam can be compensated to some extent, e.g. with higher beam energies, whereas non-uniformly distributed materials result in a variable ion attenuation depending on the position of the beam path and lead to a decrease in the precision of the particle range. Consequently, the design of the two developed RF coils took into account the radiation transparency of the coil components and avoided capacitors in the radiation window (see fig. 3.4 and fig. 3.6). Due to the calculated high stopping power of copper compared to the polyimide and adhesive layers (see fig. 4.1) as well as the inhomogeneous distribution of the conductive layer (see fig. 3.5), a small conductor thickness is advantageous for RF coils in MRgPT. However, the conductor thickness should be at least one skin depth [Giovannetti et al., 2023] (see eq. 3.1) for the given frequency to avoid SNR loss due to unfavorable current distribution along the conductor [Barta et al., 2021]. The skin depth for copper is $\approx 8\,\mu m$ for a frequency of 63.68 MHz (1.5 T) and $\approx 20\,\mu m$ for a frequency of 10.25 MHz (0.25 T). Therefore, a thickness of 35 µm with a calculated WET of $235-238\,\mu m$ was chosen for the copper layer. The measured change in the position of the Bragg peak maximum and D_{50} (see table 4.3) based on the dose distribution in a water column suggests a

WET of 180−190 µm for the copper layer. The small deviation between simulated and measured WET of the conductor (45−58 µm) can be attributed to a varying width of the Bragg peak between measurements caused by the stochastic uncertainty of the measured range for individual particles [Newhauser and Zhang, 2015] (range straggling) and the limited spatial resolution for a step size of 50 µm. In addition, the WET calculation was based on the Bethe-Bloch equation (see eq. 2.77) without considering reported corrections to the formula [Salvat, 2022] using approximate values for the ionization energy (see eq. 2.79) and a mass-weighted effective atomic number and mass number for multi-element materials (e.g., $Z_{eff}(H_2O) = 7.22$). However, deviating effective atomic numbers for water ($Z_{eff} = 7.68$) have already been reported in the literature [Taylor et al., 2012]. With a higher effective atomic number for water, the stopping power ratio of copper relative to water and the calculated WET of the conductor layer would be lower and could thus approach the measured value (see section 4.1.2). Furthermore, studies suggest an energy dependence of the effective atomic number of water at lower energies (< 20 MeV), especially for carbon ions [Rezaeian et al., 2023], which may also contribute to the observed deviation between the measured and calculated WET of the materials (see section 4.1). The exact determination of the lateral scattering effects of the particle beam due to the RF coil materials is rather complex [Newhauser and Zhang, 2015] and was not investigated in this thesis. However, a negligible increase of the lateral penumbra of the particle beam is expected due to the small thickness of the coil layers [Rana et al., 2013]. Since, in addition to the negligible change in the ion range due to a low WET, no substantial longitudinal range straggling was detected in the measured Bragg curves (see table 4.3), especially when the conductor was partially irradiated, the copper layer is considered to be radiation-transparent.

The flexible layers of the two developed RF coils were each mounted on a homogeneous PMMA cylinder in order to avoid uncorrectable ion attenuation or scattering effects due to a non-uniform mass distribution of a standard coil housing, e.g. with openings. While the wall thickness of the PMMA cylinder can be corrected with higher beam energies, the investigated variation in the wall thickness resulted in a standard deviation in the WET of 88 µm and 40 µm for different positions of the RF body coil and the RF calf coil, respectively. Therefore, the variation in the wall thickness and the corresponding variation in the WET of the PMMA cylinder is less important than the WET of the conductor and the PMMA cylinder can be used for particle beam irradiation despite manufacturer tolerances. However, the consideration of the calculated ion attenuation of the PMMA cylinder is only valid for an orthogonal irradiation direction of the particle beam. If a large tumor volume is irradiated using the raster scanning technique [Haberer et al., 1993], the effectively penetrated material thickness of the PMMA cylinder and the associated ion attenuation may increase depending on the irradiation angle.

In summary, the two coil configurations are particularly well suited for ion irradiation because both the transmit/receive RF body coil in a potential open-bore MR system

[Mislow et al., 2010] (e.g., double-doughnut shaped) and the RF calf coil in the C-shaped magnet allow MRgPT with only one RF coil in the irradiation path. In addition, no RF shielding was integrated into either RF coil to minimize the influence of the RF coil materials on the particle beam.
Overall, high radiation transparency or uniform mass distribution, and thus correctable ion attenuation, was demonstrated for all coil components, thus establishing the suitability of the RF coils for flexible MRgPT with multi-angle irradiation without having to consider the position of the conductor. Future studies should investigate the feasibility of simultaneous imaging with particle beam irradiation (real-time gating) in terms of image quality and long-term durability of RF coil materials, as radiation-induced currents in RF coils for MRI have been reported e.g., for photon irradiation [Burke et al., 2010] [Burke et al., 2012].

5.2 Imaging performance of the RF body coil

In order to evaluate the MR imaging properties of the RF body coil, especially during patient rotation, the transmit and receive field homogeneity was investigated in simulations and MR measurements. Furthermore, the SNR of the RF body coil was determined in a homogeneous phantom and compared to the internal body coil of the "offline" 1.5 T MR system. The simulated transmit power efficiency of the RF body coil was evaluated in the transverse slice for a homogeneous phantom and a human voxel model, and compared to the measured transmit power efficiency in a homogeneous phantom. In addition, the specific absorption rate was calculated in a heterogeneous voxel model to determine the maximum average allowed transmit power in vivo.

5.2.1 Patient rotation

To provide flexible multi-angle particle beam delivery for treatment centers without a costly ion gantry, the concept of patient rotation, first introduced for MR-linacs [Whelan et al., 2017] [Buckley et al., 2019] [Buckley et al., 2020], was implemented. In contrast to the work of Whelan and Buckley, in this work, the subject was rotated together with a developed RF body coil. To study the effect of patient rotation, an anthropomorphic phantom filled with various organ-simulating substances (see fig. 3.11) was first positioned in the patient capsule including the developed RF body coil and fixed with vacuum mattresses (see fig. 3.8) and then rotated in the magnet bore of an "offline" 1.5 T MR system. MR images of the phantom rotated by 0° and 90° show considerable displacement of the organs and deformation of the body contours due to the change in the direction of gravity (see fig. 4.10). This observation is consistent with in vivo measurements in the literature where non-rigid deformations and displacements of organs (e.g., bladder) have been reported [Buckley et al., 2019]. Therefore, MRI is needed to accurately capture changes in

body contours and organ position to allow for treatment modifications. For the transition from proof-of-concept to clinical application of MRgPT, open-bore systems such as a double-doughnut or C-shaped magnet [Mislow et al., 2010] are required in the final setup to avoid ion beam attenuation or scattering effects at the gradient coil, cryostat, or other components of the MR scanner. In addition, further studies are needed to investigate the patient tolerance of the patient rotation system, including anxiety [Marteau and Bekker, 1992], claustrophobia [Radomsky et al., 2001], and motion sickness [Keshavarz and Hecht, 2011], especially since increased anxiety and claustrophobia are expected in combination with MRI [Katz et al., 1994].

5.2.2 Radiofrequency field homogeneity

To evaluate the feasibility of patient rotation with the developed unshielded RF body coil, the RF field homogeneity of the transmit and receive fields of the RF body coil was investigated in simulations and MR measurements in a homogeneous phantom and a heterogeneous voxel model (in simulations only) for a complete rotation of the RF body coil and patient capsule in steps of 15°. In this context, the simulated and measured transmit and receive field distributions of the RF body coil were compared with the RF field distribution of the internal body coil in the central transverse layer of a homogeneous phantom. A qualitative analysis of the RF field distributions of the developed RF coil and the internal commercial coil shows non-uniform patterns in both cases, especially at the edge of the phantom (see fig. 4.4 and fig. 4.5). However, similar inhomogeneities have been reported in the literature [Vaidya et al., 2016] [Cloos et al., 2016].
A more detailed investigation of the measured transmit (B_1^+) and receive (B_1^-) fields results in maximum COV values of 6.9 % (B_1^+) and 9.6 % (B_1^-) in the central transverse ($240\times120\,\mathrm{mm}^2$), coronal ($240\times180\,\mathrm{mm}^2$) and sagittal ($120\times180\,\mathrm{mm}^2$) slices across 24 different rotation angles of the patient capsule (see fig. 4.6). For this full rotation of the patient capsule, the COV values in a 3D ROI ($-108\,\mathrm{mm} \leq$ z $\leq 108\,\mathrm{mm}$ and complete x and y range) of 3.0−12.3 % (B_1^+) and 7.2−12.9 % (B_1^-) are slightly elevated, indicating increased inhomogeneity at the edges of the phantom at 63.68 MHz. Similar COV values (B_1^+: 7.0 %, B_1^-: 8.0 %) were reported with an oval-shaped volume coil at 78.6 MHz in a 3D ROI ($-115\,\mathrm{mm} \leq$ x $\leq 115\,\mathrm{mm}$, $-65\,\mathrm{mm} \leq$ y $\leq 65\,\mathrm{mm}$, $-100\,\mathrm{mm} \leq$ z $\leq 100\,\mathrm{mm}$) of a homogeneous torso phantom [Platt et al., 2018]. For a 3D ROI in the heterogeneous voxel model, the COV values of the transmit and receive field homogeneity do not exceed 9.1 % (B_1^+) and 13.1 % (B_1^-). The RF field homogeneity (see fig. 4.6) in the heterogeneous voxel model increases (B_1^-) or decreases (B_1^+) if the RF body coil is rotated by multiples of 45°. Similarly, better tuning and matching (see fig. 4.3 B) could be achieved for the same rotation angles. These phenomena could be related to the symmetry of the 16-rung birdcage resonator ($360°/16 = 22.5°$).
Compared to COV values of 26.9 % (B_1^+) reported in the literature for a 33 cm

long body coil at a magnetic field strength of 7 T at 298 MHz [Gokyar et al., 2022], the here developed RF body coil achieves considerably better field homogeneity, as expected for an RF coil with a lower resonance frequency.
The dependence of the RF field homogeneity on the rotation angle of the RF body coil including the phantom (see fig. 4.6) can be partly attributed to the asymmetric shape of the phantom: Since the resonance frequency of the RF body coil was tuned for the phantom in horizontal position (see fig. 4.3), the COV values are lower for rotation angles near 0° and 180° and maximum for rotation angles near 90° and 270°. However, the elevated position of the patient capsule with respect to the central axis of the magnet bore (y = Y + 56 mm), due to the lack of space in the magnet bore (see fig. 3.12), also leads to a higher dependency of the RF field homogeneity on the rotation angle compared to the simulated rotation in the isocenter of the MR system (see fig. 4.6).
Overall, a good agreement between measurement and simulation and sufficient RF field homogeneity in a large FOV was achieved for the developed RF body coil in order to differentiate between different tissue types in the torso.

5.2.3 Transmit power efficiency

The simulated and measured average transmit power efficiency of the RF body coil in the central transverse slice of a homogeneous phantom has been calculated with respect to the applied reference power of the RF pulse (see eq. 4.4) at the input of the transmit/receive switch and corresponds to $0.29 - 0.31\frac{\mu T}{\sqrt{W}}$ (simulations) and $0.18 - 0.27\frac{\mu T}{\sqrt{W}}$ (MR measurements), respectively, depending on the rotation angle of the patient capsule. Due to power losses along the transmit path of -0.92 dB (see section 5.4.1) only $\approx 81\,\%$ of the transmit power reaches the ports of the RF body coil. To characterize the RF body coil without the transmit chain (transmit/receive switch, quadrature hybrid, coaxial cable, ...) the measured average transmit power efficiencies were corrected for the power losses assuming 1 W transmit power at the RF coil ports. As a result, average transmit power efficiencies of $0.20 - 0.30\frac{\mu T}{\sqrt{W}}$ were achieved for a full rotation of the RF body coil. In comparison, transmit power efficiencies of $0.25\frac{\mu T}{\sqrt{W}}$ [Gokyar et al., 2022] (birdcage resonator), $0.17\frac{\mu T}{\sqrt{W}}$ [Gokyar et al., 2022] (transverse EM resonators [Vaughan et al., 1994]), and $0.10\frac{\mu T}{\sqrt{W}}$ [Orzada et al., 2019] (parallel transmit systems) with respect to the applied RF power at the RF coil ports have been reported for whole body imaging at 7 T in the isocenter of a homogeneous phantom. In addition, the lower reference voltage of the RF body coil compared to the internal body coil is a good indicator that the RF body coil achieves a sufficient transmit field to efficiently manipulate the nuclear magnetization. The simulated average transmit power efficiency in the transverse slice of the heterogeneous voxel model ($0.24 - 0.30\frac{\mu T}{\sqrt{W}}$) is slightly lower compared to the phantom simulation. Similar to the reduction of the simulated RF field homogeneity in the heterogeneous voxel model at specific rotation angles due to the

symmetry of the birdcage design (discussed in the previous section 5.2.2), the simulated transmit power efficiency in the voxel model appears to be slightly increased if the RF body coil is rotated by multiples of 45° (see fig. 4.7).

5.2.4 Signal-to-noise ratio

In terms of imaging quality, the SNR of the radiation-transparent RF body coil was determined in a central subvolume ($\Delta z = 60\,mm$ and complete x and y range) of a homogeneous torso phantom, yielding SNR values between 110 and 161 depending on the angle of rotation of the RF body coil and patient capsule (see fig. 4.8). These values represent an SNR improvement between 7−64 % compared to the internal body coil ($SNR_{\Delta z=60\,mm}$: 98−105). The larger variations in the SNR of the radiation-transparent RF body coil compared to the internal body coil can be attributed to the off-axis rotation (see fig. 3.12) of the radiation-transparent RF body coil as already discussed in section 5.2.2. Slightly lower SNR values (SNR: 87 − 103) have been reported for a 1 T MR system in combination with a patient rotation system [Buckley et al., 2020]. Due to the inherently better SNR at higher magnetic field strengths (see eq. 2.56) and different MR sequence parameters (T_R, T_E, FOV, slice thickness, measurement time), the SNR values are not directly comparable. Furthermore, the SNR values reported in the literature, were obtained in a spherical body phantom for three different rotation angles (0°, 90°, 180°) using a spin echo sequence (see section 2.2.5), whereas the SNR in the radiation-transparent RF body coil was determined in an oval-shaped torso phantom filled with a different solution and for 24 rotation angles using a GRE sequence. In general, higher SNR values were obtained with the radiation-transparent RF body coil compared to the internal body coil. Furthermore, a higher stability of the SNR across different rotation angles can be expected if the RF coil was located in the center of the magnet bore (y = Y).

5.2.5 Specific absorption rate & maximum transmit power

To assess the RF safety of the RF body coil, the partial body and whole body SAR were simulated for a heterogeneous voxel model and the corresponding SAR limits were determined based on the IEC standards (see table 2.1) in normal and first level operation (see fig. 4.9 A). Since the 1.5 T field strength is associated with relatively minor RF field interference [Cloos et al., 2016], the whole body SAR of a body coil imposes a more stringent limit (normal mode: $2\,\frac{W}{kg}$, first level mode: $4\,\frac{W}{kg}$) than the partial body SAR. The resulting maximum average transmit power (see fig. 4.9 B) is limited to 155 W by the whole body SAR in the normal mode and to 310 W by both the whole body SAR and the partial body SAR in the first level mode, which is sufficient for efficient B_1^+ field generation in a patient with a standard body coil [Zhang et al., 2021]. In addition, the simulated power limits remain approximately constant for all 24 rotation angles of the RF body coil, including the human voxel

model, demonstrating the applicability of patient rotation in terms of RF safety.

5.3 Imaging performance of the RF calf coil

To evaluate the imaging performance of the receive-only RF calf coil, the homogeneity of the simulated receive fields was calculated in the three central slices and in a volume of a homogeneous phantom for a complete rotation in steps of 15°. In addition, the SNR was determined for the central transverse, coronal, and sagittal slices in a homogeneous phantom and then compared with the SNR of commercially available receive coils. In addition, to demonstrate the suitability of the RF calf coil for clinical use, in vivo imaging of human extremities was performed.

5.3.1 Receive field homogeneity

In this work, only simulated and not measured receive maps could be examined (see eq. 3.7), since no transmit maps could be determined from measurements with different flip angles on the clinical C-shaped 0.25 T MR system due to different automatic calibration between measurements. The simulated receive field distributions show high homogeneity in the central slices of a homogeneous phantom and a voxel model of a calf (see fig. 4.12) while slightly reduced receive fields at the opening of the solenoid in the sagittal slice (Y = 0 mm) and especially in the coronal slice (Z = 0 mm) can be attributed to the solenoid structure of the RF calf coil (see fig. 3.6). In contrast to the RF body coil of the "offline" 1.5 T MR system, the RF calf coil of the "online" 0.25 T MR system is located in the isocenter of the magnet. Furthermore, the homogeneous phantom used for the RF calf coil is rotationally symmetric and represents a human calf with a less complex tissue distribution compared to the human torso (see fig. 3.10). Therefore, rotation of the phantom or voxel model including the RF calf coil has little effect on the homogeneity of the receive field (see fig. 4.3.2). The quantitative analysis of the homogeneity of the simulated receive fields in a 2D ROI showed COV values below 0.8 % (48×48 mm^2) in the transverse, 2.5 % (72×72 mm^2) in the coronal and 2.1 % (64×64 mm^2) in the sagittal slice in the center of a homogeneous phantom and a heterogeneous voxel model of a human calf for all simulation angles investigated (see section 4.3.2). COV values up to 7 % in a 3D ROI ($-64\,mm \leq X \leq +64\,mm$ and complete Y and Z range) indicate reduced field homogeneity towards the edges of the phantom. Similar COV values (measurement: 8.0 %, simulation: 6.7 %) for the receive field distribution have been reported in a 3D ROI ($-115\,mm \leq x \leq 115\,mm$, $-65\,mm \leq y \leq 65\,mm$, $-100\,mm \leq z \leq 100\,mm$) with an oval-shaped body resonator for torso imaging at 78.6 MHz [Platt et al., 2021].
Overall, the developed radiation-transparent RF calf coil shows a homogeneous receive sensitivity profile with low COV values in the simulation. The high homogeneity of the receive field distribution of the RF calf coil compared to two commercially

available coils is also reflected in the signal intensity distribution of the MR images in a homogeneous phantom (cf. fig. 4.12 and fig. 4.14), where the COV values confirm considerably better homogeneity of the RF calf coil in all central slices compared to two commercial coils (see table 4.6). In further studies, the presented results could be investigated in more realistic EM field simulations with a larger body part of a more detailed human voxel model with better spatial resolution, including more tissue types such as arteries, veins, cartilage, tendons, ligaments and bone marrow.

5.3.2 Signal-to-noise ratio

The signal-to-noise ratio (SNR) in the acquired MR images was determined for the radiation-transparent RF calf coil according to section 3.4.4 and an increase in SNR of 20−50 % was achieved depending on the central slice in the homogeneous phantom (see table 4.6) compared to the two commercial imaging coils. A lower image noise of the transverse slice (X = 0 mm) compared to the sagittal (Y = 0 mm) and coronal (Z = 0 mm) slices for all three coils can be attributed to fewer artifcats in the noise ROI (defined with thresholds) of the MR images. Although the gain in SNR compared to commercial coils is mainly due to the reduced noise figure of the preamplifier (see section 5.4.2), the geometry of a solenoid coil inherently provides higher sensitivity than a linear saddle or birdcage coil [Hoult and Richards, 1976]. In addition, the RF calf coil was designed so that the length of the solenoid (length: 139 mm) is 70−80 % of the diameter (diameter: 180 mm) and the distance between the turns is at least three times the width of the strip, resulting in an optimal SNR according to literature [Hoult and Lauterbur, 1979]. The solenoid structure results in higher signal intensities further away from the coil center compared to the two commercial coils of the "online" MR system at 0.25 T based on surface loops (see fig. 4.15). In addition, an increased turn density at the coil ends was implemented (see fig. 3.6) to achieve a more uniform receive sensitivity profile [Leifer, 1993] covering a larger FOV along the central x axis (Y = Z = 0 mm). The RF calf coil achieves 92.7 % (X = +40 mm) and 90.4 % (X = −40 mm) of the SNR in the coil center along the central X axis at a distance D = 40 mm from the coil isocenter (X = 0 mm). A theoretical maximum of 90 % of the SNR at the coil center has been reported in the literature for ordinary solenoid coils of twice the length of the developed RF calf coil (length: 280 mm) and larger diameter (diameter: 280 mm) along the central longitudinal axis at a distance of D = −80 mm or D = +80 mm [Blasiak et al., 2009].
Overall, the RF calf coil with the modified solenoid geometry achieves an increase in RF field homogeneity and covers a larger FOV while exceeding the SNR of commercial imaging coils.

5.3.3 In vivo imaging

MR imaging with a low-field MR system finds clinical application especially in the imaging of the musculoskeletal system in the extremities, and high diagnostic value

has been reported [Vellet et al., 1995] [Ejbjerg et al., 2005], despite the inherently lower SNR of MRI at lower field strengths (see eq. 2.56). Often, the diagnostic performance is sufficient to identify pathologies in the extremities such as tumors, cysts, and tears in cartilage, ligaments, or tendons with a similar prevalence as standard MRI at higher field strengths [Ghazinoor et al., 2007] [Lopez Schmidt et al., 2023]. This is partly due to the B_0 field dependence of the spin-lattice relaxation time T_1, as T_1 decreases at lower field strengths, leading to improved image contrast (e.g., between fat and muscle tissue), especially in T_1-weighted images [Rooney et al., 2007]. In the in vivo MR images of a human calf and hand (see fig. 4.16 and fig. 4.17), it is possible to differentiate between fat, bone, bone marrow, veins (calf only), and muscle tissue, including different muscle regions. However, no bone marrow was observed in the fibula, which may be due to the limited resolution and SNR of the MR images. In general, the in vivo MR imaging capability of the RF calf coil has been demonstrated in the human calf and hand. In future studies, for example, the in vivo image quality of the developed RF calf coil could be compared with that of commercially available coils in collaboration with radiologists. Other possible radiation-transparent RF coil designs, such as a larger RF coil for the human head or an oval RF coil for imaging the torso, could be realized in future studies.

5.4 Supplementary electronics

Additional hardware components in the transmit/receive chain have been designed and built to maximize the imaging performance of the RF coils. This includes the transmit/receive switch (see section 3.3.1) and the quadrature hybrid for the RF body coil at the "offline" 1.5 T MR system and the preamplifier (see section 3.3.2) for the RF calf coil at the "online" 0.25 T MR system.

5.4.1 Transmit/receive switch & quadrature hybrid

The RF body coil is operated as a transmit/receive coil and a transmit/receive switch with actively controlled PIN diodes allows switching between the transmit and receive mode. In the case of transmission, sufficient isolation of $-47.3\,\mathrm{dB}$ (see table 3.3) between the transmit port and the receive path was achieved. The quadrature hybrid between the transmit/receive switch and the RF body coil provides an isolation of $-22.64\,\mathrm{dB}$ (see table 3.4). In the transmit case, signal losses of $-0.6\,\mathrm{dB}$ (see table 3.3) occur in the transmit/receive switch and $-0.32\,\mathrm{dB}$ (see table 3.4) in the quadrature hybrid. These values are comparable to those reported in the literature [Thapa et al., 2016] for the isolation between the transmit and receive path of a transmit/receive switch (isolation: $-49\,\mathrm{dB}$) and a quadrature hybrid (isolation: $-20\,\mathrm{dB}$) during transmission, and a signal loss of $-0.8\,\mathrm{dB}$ (transmit/receive switch) and $-0.5\,\mathrm{dB}$ (quadrature hybrid) on the transmit path when the RF excitation is

transmitted. Therefore, both the transmit/receive switch and the quadrature hybrid are well tuned to the appropriate frequency (63.68 MHz) and are suitable for transmission of the RF excitation signal to the RF body coil, for protection of the preamplifier and for forwarding the detected MR signal to the sensitive preamplifier.

5.4.2 Preamplifier

As part of this work, a low-noise preamplifier was developed to amplify the MR signal at a frequency of 10.25 MHz acquired with the RF calf coil. A gain of 23.5 dB and a noise figure of 1.0 dB were achieved for the developed preamplifier, which meets the literature specifications of a gain of 20−30 dB and a noise figure of 0.5−1.2 dB [Webb and O'Reilly, 2023]. In addition, a lower noise figure was achieved than for the commercial preamplifier at 63.68 MHz (noise figure: 2.5 dB). Since the noise figure of the preamplifier is a decisive factor for the noise in the final MR image [Webb and O'Reilly, 2023], the quality of the preamplifier can also be confirmed by the image noise in the background (see table 4.6). In particular, the image noise in the background acquired with the radiation-transparent RF calf coil including the developed preamplifier corresponds to only 62.5−66.4 % (X = 0 mm), 83.7−84.9 % (Y = 0 mm) and 66.0−69.6 % (Z = 0 mm) of the image noise of the commercial coils. Due to the low noise figure in the designed preamplifier, the SNR of the designed RF calf coil is increased compared to the commercial cervical coil and the commercial knee coil.

Chapter 6

Conclusion

The aim of this work was to develop RF coils for MR imaging that can be combined with particle radiation. As part of this work, a rotatable, radiation-transparent transmit/receive RF body coil for a 1.5 T MR system and a rotatable, radiation-transparent receive-only RF calf coil for a 0.25 T C-shaped MR system were designed and constructed, including additional hardware (RF switch, quadrature hybrid, preamplifier, ...). The designed coil configurations enable 360° rotation of the patient, allowing flexible multi-angle irradiation even for treatment facilities with a static particle beam that cannot afford an ion gantry. Using a conductor layer with negligible water-equivalent thickness, high radiation transparency was achieved for two different coil geometries (solenoid, birdcage) for a large irradiation window. Despite a conductor thickness of only a few skin depths at the corresponding frequency, the two developed RF coils show excellent imaging performance in terms of homogeneity of the receive sensitivity profile over a large FOV and in terms of SNR for different rotation angles compared to commercial RF coils, indicating suitability for a clinical application. High transmit field homogeneity and power efficiency were also achieved for the RF body coil. In summary, the presented RF coil designs demonstrate the feasibility of combined MRI and particle irradiation for flexible cancer therapy, e.g., in the abdomen or the extremities while maintaining the dose delivery precision and treatment quality of particle therapy.

Appendix

Publications

Conferences

Parts of this thesis have been presented at international conferences.

E-poster presentation

- **Dietrich, Kilian A.**; Klüter, Sebastian; Debus, Jürgen; Ladd, Mark E.; Platt, Tanja, "Performance of a rotatable Tx/Rx body coil for MR-guided particle therapy", Proceedings of the 31st Annual Meeting of the ISMRM, Toronto, Canada (2023), Abstract 4385

- **Dietrich, Kilian A.**; Klüter, Sebastian; Debus, Jürgen; Dinkel, Fabian; Echner, Gernot; Ladd, Mark E.; Platt, Tanja, "Construction of a Tx/Rx body coil on a rotatable patient capsule for MR-guided particle therapy", Proceedings of the 30th Annual Meeting of the ISMRM, London, England (2022), Abstract 1094

- **Dietrich, Kilian A.**; Klüter, Sebastian; Knowles, Benjamin R.; Debus, Jürgen; Ladd, Mark E.; Platt, Tanja, "Comparison of birdcage resonator designs for clinical MR-guided radiotherapy", Proceedings of the 29th Annual Meeting of the ISMRM, virtual (Vancouver, Canada) (2021), Abstract 4013

Study group presentation

- **Dietrich, Kilian A.**, Klüter Sebastian, Debus Jürgen, Ladd Mark E., Platt Tanja, "A rotatable Tx/Rx body coil for MR-guided particle therapy", Abstract Nominee for Trainee Award during the Study Group Business Meeting of the ISMRM Study Group MR Engineering at the 31st Annual Meeting of the ISMRM, Toronto, Canada (2023)

Further submissions

Parts of this thesis have been submitted to a journal and a further conference:

Research article submitted for the journal of Medical Physics

- **Dietrich, Kilian A.**; Klüter, Sebastian; Dinkel, Fabian; Echner, Gernot; Brons, Stephan; Orzada, Stephan; Debus, Jürgen; Ladd, Mark E.; Platt, Tanja, "An essentially radiation-transparent body coil integrated with a patient rotation system for MR-guided particle therapy", (2023)

Abstract submitted to ISMRM conference in 2024

- **Dietrich, Kilian A.**; Orzada, Stephan; Fielder, Thomas M.; Dinkel, Fabian; Echner, Gernot; Klüter, Sebastian; Debus, Jürgen; Ladd, Mark E.; Platt, Tanja, "A radiation-transparent, rotatable receive-only extremity RF coil for flexible MR-guided particle therapy at 0.25 T", Submitted to the 32nd Annual Meeting of the ISMRM, Singapore, Singapore (2023)

Bibliography

[Abragam, 1983] Abragam, A. (1983). *The Principles of Nuclear Magnetism*. International Series of Monographs on Physics. Oxford University Press, Oxford, New York.

[Acharya et al., 2016] Acharya, S., Fischer-Valuck, B. W., Kashani, R., Parikh, P., Yang, D., Zhao, T., Green, O., Wooten, O., Li, H. H., Hu, Y., Rodriguez, V., Olsen, L., Robinson, C., Michalski, J., Mutic, S., and Olsen, J. (2016). Online Magnetic Resonance Image Guided Adaptive Radiation Therapy: First Clinical Applications. *International Journal of Radiation Oncology*Biology*Physics*, 94(2):394–403.

[Barta et al., 2021] Barta, R., Volotovskyy, V., Wachowicz, K., Fallone, B. G., and De Zanche, N. (2021). How thin can you go? Performance of thin copper and aluminum RF coil conductors. *Magnetic Resonance in Medicine*, 85(4):2327–2333. _eprint: https://onlinelibrary.wiley.com/doi/pdf/10.1002/mrm.28540.

[Bernstein et al., 2004] Bernstein, M. A., King, K. F., and Zhou, X. J., editors (2004). *Handbook of MRI - Pulse Sequences*. Academic Press, Burlington.

[Blasiak et al., 2009] Blasiak, B., Volotovskyy, V., Deng, C., and Tomanek, B. (2009). An optimized solenoidal head radiofrequency coil for low-field magnetic resonance imaging. *Magnetic Resonance Imaging*, 27(9):1302–1308.

[Bloch, 1933] Bloch, F. (1933). Zur Bremsung rasch bewegter Teilchen beim Durchgang durch Materie. *Annalen der Physik*, 408(3):285–320. _eprint: https://onlinelibrary.wiley.com/doi/pdf/10.1002/andp.19334080303.

[Bloch, 1946] Bloch, F. (1946). Nuclear Induction. *Physical Review*, 70(7-8):460–474. Publisher: American Physical Society.

[Bohoudi et al., 2017] Bohoudi, O., Bruynzeel, A. M. E., Senan, S., Cuijpers, J. P., Slotman, B. J., Lagerwaard, F. J., and Palacios, M. A. (2017). Fast and robust online adaptive planning in stereotactic MR-guided adaptive radiation therapy (SMART) for pancreatic cancer. *Radiotherapy and Oncology: Journal of the European Society for Therapeutic Radiology and Oncology*, 125(3):439–444.

[Buckley et al., 2020] Buckley, J. G., Dong, B., and Liney, G. P. (2020). Imaging performance of a high-field in-line magnetic resonance imaging linear accelerator with a patient rotation system for fixed-gantry radiotherapy. *Physics and Imaging in Radiation Oncology*, 16:130–133.

[Buckley et al., 2019] Buckley, J. G., Rai, R., Liney, G. P., Dowling, J. A., Holloway, L. C., Metcalfe, P. E., and Keall, P. J. (2019). Anatomical deformation due to horizontal rotation: towards gantry-free radiation therapy. *Physics in Medicine & Biology*, 64(17):175014. Number: 17 Publisher: IOP Publishing.

[Burke et al., 2010] Burke, B., Fallone, B. G., and Rathee, S. (2010). Radiation induced currents in MRI RF coils: application to linac/MRI integration. *Physics in Medicine & Biology*, 55(3):735. Number: 3.

[Burke et al., 2012] Burke, B., Wachowicz, K., Fallone, B. G., and Rathee, S. (2012). Effect of radiation induced current on the quality of MR images in an integrated linac-MR system. *Medical Physics*, 39(10):6139–6147. Number: 10 _eprint: https://onlinelibrary.wiley.com/doi/pdf/10.1118/1.4752422.

[Callaghan, 1993] Callaghan, T. l. P. T. (1993). *Principles of Nuclear Magnetic Resonance Microscopy*. Oxford University Press, Oxford, New York.

[Chen et al., 1983] Chen, C. N., Hoult, D. I., and Sank, V. J. (1983). Quadrature detection coils—A further $\sqrt{2}$ improvement in sensitivity. *Journal of Magnetic Resonance (1969)*, 54(2):324–327.

[Christ et al., 2009] Christ, A., Kainz, W., Hahn, E. G., Honegger, K., Zefferer, M., Neufeld, E., Rascher, W., Janka, R., Bautz, W., Chen, J., Kiefer, B., Schmitt, P., Hollenbach, H.-P., Shen, J., Oberle, M., Szczerba, D., Kam, A., Guag, J. W., and Kuster, N. (2009). The Virtual Family—development of surface-based anatomical models of two adults and two children for dosimetric simulations. *Physics in Medicine & Biology*, 55(2):N23. Number: 2.

[Clemens and Weiland, 2001] Clemens, M. and Weiland, T. (2001). Discrete Electromagnetism with the Finite Integration Technique. *Progress In Electromagnetics Research*, 32:65–87.

[Cloos et al., 2016] Cloos, M. A., Knoll, F., Zhao, T., Block, K. T., Bruno, M., Wiggins, G. C., and Sodickson, D. K. (2016). Multiparametric imaging with heterogeneous radiofrequency fields. *Nature Communications*, 7(1):12445. Number: 1 Publisher: Nature Publishing Group.

[Collins et al., 1998] Collins, C. M., Li, S., and Smith, M. B. (1998). SAR and B1 field distributions in a heterogeneous human head model within a birdcage coil. *Magnetic Resonance in Medicine*, 40(6):847–856. _eprint: https://onlinelibrary.wiley.com/doi/pdf/10.1002/mrm.1910400610.

[Cooley and Tukey, 1965] Cooley, J. and Tukey, J. (1965). An algorithm for the machine calculation of complex Fourier series. *Mathematics of Computation*, 19(90):297301.

[Corradini et al., 2019] Corradini, S., Alongi, F., Andratschke, N., Belka, C., Boldrini, L., Cellini, F., Debus, J., Guckenberger, M., Hörner-Rieber, J., Lagerwaard, F. J., Mazzola, R., Palacios, M. A., Philippens, M. E. P., Raaijmakers, C. P. J., Terhaard, C. H. J., Valentini, V., and Niyazi, M. (2019). MR-guidance in clinical reality: current treatment challenges and future perspectives. *Radiation Oncology*, 14(1):92. Number: 1.

[Diaham et al., 2020] Diaham, S., O'Sullivan, L., Ceccarelli, E., Lambkin, P., O'Malley, J., Fitzgibbon, J., Stenson, B., Murphy, P., Zhao, Y., Cornett, J., Sow, A., Chen, B., and Geary, S. (2020). Improving Polyimide Isolation Performance by Tailoring Interfaces with Nitride Layers for Digital Isolator Application. *2020 IEEE 3rd International Conference on Dielectrics (ICD)*, pages 570–573.

[Dixon, 1984] Dixon, W. T. (1984). Simple proton spectroscopic imaging. *Radiology*.

[Dzierma et al., 2018] Dzierma, Y., Mikulla, K., Richter, P., Bell, K., Melchior, P., Nuesken, F., and Rübe, C. (2018). Imaging dose and secondary cancer risk in image-guided radiotherapy of pediatric patients. *Radiation Oncology*, 13(1):168. Number: 1.

[Ebert et al., 2019] Ebert, N., Tillner, F., and Baumann, M. (2019). *Radiation Oncology*. Academic Press, Oxford.

[Ejbjerg et al., 2005] Ejbjerg, B. J., Narvestad, E., Jacobsen, S., Thomsen, H. S., and Østergaard, M. (2005). Optimised, low cost, low field dedicated extremity MRI is highly specific and sensitive for synovitis and bone erosions in rheumatoid arthritis wrist and finger joints: comparison with conventional high field MRI and radiography. *Annals of the Rheumatic Diseases*, 64(9):1280–1287. Publisher: BMJ Publishing Group Ltd Section: Extended report.

[Esaote, 2019] Esaote (2019). S-Scan User Manual - 350003100 Rev. 11. Esaote, Genova, Italy.

[Fiedler et al., 2017] Fiedler, T. M., Ladd, M. E., and Bitz, A. K. (2017). RF safety assessment of a bilateral four-channel transmit/receive 7 Tesla breast coil: SAR versus tissue temperature limits. *Medical Physics*, 44(1):143–157. _eprint: https://onlinelibrary.wiley.com/doi/pdf/10.1002/mp.12034.

[Fiedler et al., 2018] Fiedler, T. M., Ladd, M. E., and Bitz, A. K. (2018). SAR Simulations & Safety. *NeuroImage*, 168:33–58.

[Foot, 2004] Foot, C. J. (2004). *Atomic Physics*. Oxford Master Series in Physics. Oxford University Press, Oxford, New York.

[Gabriel et al., 1996] Gabriel, C., Gabriel, S., and Corthout, E. (1996). The dielectric properties of biological tissues: I. Literature survey. *Physics in Medicine & Biology*, 41(11):2231.

[Gao et al., 2018] Gao, Y., Zhou, Z., Han, F., Cao, M., Shaverdian, N., Hegde, J. V., Bista, B. B., Steinberg, M., Lee, P., Raldow, A., Low, D. A., Yang, Y., and Hu, P. (2018). Accelerated 3D bSSFP imaging for treatment planning on an MRI-guided radiotherapy system. *Medical Physics*, 45(6):2595–2602. Number: 6 _eprint: https://onlinelibrary.wiley.com/doi/pdf/10.1002/mp.12924.

[Ghazinoor et al., 2007] Ghazinoor, S., Crues III, J. V., and Crowley, C. (2007). Low-field musculoskeletal MRI. *Journal of Magnetic Resonance Imaging*, 25(2):234–244. _eprint: https://onlinelibrary.wiley.com/doi/pdf/10.1002/jmri.20854.

[Giovannetti et al., 2023] Giovannetti, G., Flori, A., and Frijia, F. (2023). Conductor Losses in Radiofrequency Coils for Magnetic Resonance below 3T: Estimation Methods and Minimization Strategies. *Sensors*, 23(12):5586. Number: 12 Publisher: Multidisciplinary Digital Publishing Institute.

[Glover et al., 1985] Glover, G. H., Hayes, C. E., Pelc, N. J., Edelstein, W. A., Mueller, O. M., Hart, H. R., Hardy, C. J., O'Donnell, M., and Barber, W. D. (1985). Comparison of linear and circular polarization for magnetic resonance imaging. *Journal of Magnetic Resonance (1969)*, 64(2):255–270.

[Gokyar et al., 2022] Gokyar, S., Voss, H. U., Taracila, V., Robb, F. J. L., Bernico, M., Kelley, D., Ballon, D. J., and Winkler, S. A. (2022). A pathway towards a two-dimensional, bore-mounted, volume body coil concept for ultra high-field magnetic resonance imaging. *NMR in Biomedicine*, 35(12):e4802. _eprint: https://onlinelibrary.wiley.com/doi/pdf/10.1002/nbm.4802.

[Gurler and Ider, 2015] Gurler, N. and Ider, Y. Z. (2015). Numerical methods and software tools for simulation, design, and resonant mode analysis of radio frequency birdcage coils used in MRI. *Concepts in Magnetic Resonance Part B: Magnetic Resonance Engineering*, 45(1):13–32. _eprint: https://onlinelibrary.wiley.com/doi/pdf/10.1002/cmr.b.21279.

[Gérard et al., 2019] Gérard, M., Corroyer-Dulmont, A., Lesueur, P., Collet, S., Chérel, M., Bourgeois, M., Stefan, D., Limkin, E. J., Perrio, C., Guillamo, J.-S., Dubray, B., Bernaudin, M., Thariat, J., and Valable, S. (2019). Hypoxia Imaging and Adaptive Radiotherapy: A State-of-the-Art Approach in the Management of Glioma. *Frontiers in Medicine*, 6.

[Haacke et al., 2014] Haacke, M. E., Brown, R. W., Thompson, M. R., and Venkatesan, R. (2014). *Magnetic Resonance Imaging - Physical Principles and Sequence Design*. John Wiley & Sons, Ltd. _eprint: https://onlinelibrary.wiley.com/doi/pdf/10.1002/9781118633953.fmatter.

[Haberer et al., 1993] Haberer, T., Becher, W., Schardt, D., and Kraft, G. (1993). Magnetic scanning system for heavy ion therapy. *Nuclear Instruments and Methods in Physics Research Section A: Accelerators, Spectrometers, Detectors and Associated Equipment*, 330(1):296–305.

[Haberer et al., 2004] Haberer, T., Debus, J., Eickhoff, H., Jäkel, O., Schulz-Ertner, D., and Weber, U. (2004). The heidelberg ion therapy center. *Radiotherapy and Oncology*, 73:S186–S190.

[Hamilton et al., 2017] Hamilton, J., Franson, D., and Seiberlich, N. (2017). Recent advances in parallel imaging for MRI. *Progress in Nuclear Magnetic Resonance Spectroscopy*, 101:71–95.

[Harrabi et al., 2016] Harrabi, S. B., Bougatf, N., Mohr, A., Haberer, T., Herfarth, K., Combs, S. E., Debus, J., and Adeberg, S. (2016). Dosimetric advantages of proton therapy over conventional radiotherapy with photons in young patients and adults with low-grade glioma. *Strahlentherapie und Onkologie*, 192(11):759–769. Number: 11.

[Harris et al., 2020] Harris, C. R., Millman, K. J., van der Walt, S. J., Gommers, R., Virtanen, P., Cournapeau, D., Wieser, E., Taylor, J., Berg, S., Smith, N. J., Kern, R., Picus, M., Hoyer, S., van Kerkwijk, M. H., Brett, M., Haldane, A., del Río, J. F., Wiebe, M., Peterson, P., Gérard-Marchant, P., Sheppard, K., Reddy, T., Weckesser, W., Abbasi, H., Gohlke, C., and Oliphant, T. E. (2020). Array programming with NumPy. *Nature*, 585(7825):357–362. Number: 7825 Publisher: Nature Publishing Group.

[Harris et al., 2002] Harris, R. K., Becker, E. D., Cabral de Menezes, S. M., Goodfellow, R., and Granger, P. (2002). NMR Nomenclature: Nuclear Spin Properties and Conventions for Chemical Shifts: IUPAC Recommendations 2001. *Solid State Nuclear Magnetic Resonance*, 22(4):458–483.

[Hasgall et al., 2022] Hasgall, P. A., Di Gennaro, F., Baumgartner, C., Neufeld, E., Lloyd, B., Gosselin, M. C., Payne, D., Klingenböck, A., and Kuster, N. (2022). IT'IS Database for thermal and electromagnetic parameters of biological tissues. Version 4.1.

[Hayes et al., 1985] Hayes, C. E., Edelstein, W. A., Schenck, J. F., Mueller, O. M., and Eash, M. (1985). An efficient, highly homogeneous radiofrequency coil for whole-body NMR imaging at 1.5 T. *Journal of Magnetic Resonance (1969)*, 63(3):622–628.

[Hess et al., 2016] Hess, C. B., Thompson, H. M., Benedict, S. H., Seibert, J. A., Wong, K., Vaughan, A. T., and Chen, A. M. (2016). Exposure Risks Among Children Undergoing Radiation Therapy: Considerations in the Era of Image Guided Radiation Therapy. *International Journal of Radiation Oncology*Biology*Physics*, 94(5):978–992. Number: 5.

[Hoffmann et al., 2020] Hoffmann, A., Oborn, B., Moteabbed, M., Yan, S., Bortfeld, T., Knopf, A., Fuchs, H., Georg, D., Seco, J., Spadea, M. F., Jäkel, O., Kurz, C., and Parodi, K. (2020). MR-guided proton therapy: a review and a preview. *Radiation Oncology*, 15(1):129. Number: 1.

[Hoogcarspel et al., 2013] Hoogcarspel, S. J., Crijns, S. P. M., Lagendijk, J. J. W., Vulpen, M. v., and Raaymakers, B. W. (2013). The feasibility of using a conventional flexible RF coil for an online MR-guided radiotherapy treatment. *Physics in Medicine & Biology*, 58(6):1925. Number: 6 Publisher: IOP Publishing.

[Hoult, 2000] Hoult, D. I. (2000). The principle of reciprocity in signal strength calculations—A mathematical guide. *Concepts in Magnetic Resonance*, 12(4):173–187. _eprint: https://onlinelibrary.wiley.com/doi/pdf/10.1002/1099-0534%282000%2912%3A4%3C173%3A%3AAID-CMR1%3E3.0.CO%3B2-Q.

[Hoult and Lauterbur, 1979] Hoult, D. I. and Lauterbur, P. C. (1979). The sensitivity of the zeugmatographic experiment involving human samples. *Journal of Magnetic Resonance (1969)*, 34(2):425–433.

[Hoult and Richards, 1976] Hoult, D. I. and Richards, R. E. (1976). The signal-to-noise ratio of the nuclear magnetic resonance experiment. *Journal of Magnetic Resonance (1969)*, 24(1):71–85.

[Hunter, 2007] Hunter, J. D. (2007). Matplotlib: A 2D Graphics Environment. *Computing in Science & Engineering*, 9(3):90–95. Conference Name: Computing in Science & Engineering.

[IEC, 2022] IEC (2022). International Electrotechnical Communications - 60601-2-33:2022.

[Insko and Bolinger, 1993] Insko, E. K. and Bolinger, L. (1993). Mapping of the Radiofrequency Field. *Journal of Magnetic Resonance, Series A*, 103(1):82–85. Number: 1.

[Ipsen et al., 2014] Ipsen, S., Blanck, O., Oborn, B., Bode, F., Liney, G., Hunold, P., Rades, D., Schweikard, A., and Keall, P. J. (2014). Radiotherapy beyond cancer: Target localization in real-time MRI and treatment planning for cardiac radiosurgery. *Medical Physics*, 41(12):120702. _eprint: https://onlinelibrary.wiley.com/doi/pdf/10.1118/1.4901414.

[Jung and Weigel, 2013] Jung, B. A. and Weigel, M. (2013). Spin echo magnetic resonance imaging. *Journal of Magnetic Resonance Imaging*, 37(4):805–817. _eprint: https://onlinelibrary.wiley.com/doi/pdf/10.1002/jmri.24068.

[Jäkel, 2009] Jäkel, O. (2009). Medical physics aspects of particle therapy. *Radiation Protection Dosimetry*, 137(1-2):156–166.

[Karger et al., 2010] Karger, C. P., Jäkel, O., Palmans, H., and Kanai, T. (2010). Dosimetry for ion beam radiotherapy. *Physics in Medicine & Biology*, 55(21):R193.

[Katz et al., 1994] Katz, R. C., Wilson, L., and Frazer, N. (1994). Anxiety and its determinants in patients undergoing Magnetic Resonance Imaging. *Journal of Behavior Therapy and Experimental Psychiatry*, 25(2):131–134.

[Keshavarz and Hecht, 2011] Keshavarz, B. and Hecht, H. (2011). Validating an Efficient Method to Quantify Motion Sickness. *Human Factors*, 53(4):415–426. Number: 4 Publisher: SAGE Publications Inc.

[Klüter, 2019] Klüter, S. (2019). Technical design and concept of a 0.35 T MR-Linac. *Clinical and Translational Radiation Oncology*, 18:98–101.

[Kondev et al., 2021] Kondev, F. G., Wang, M., Huang, W. J., Naimi, S., and Audi, G. (2021). The NUBASE2020 evaluation of nuclear physics properties *. *Chinese Physics C*, 45(3):030001. Publisher: Chinese Physical Society and the Institute of High Energy Physics of the Chinese Academy of Sciences and the Institute of Modern Physics of the Chinese Academy of Sciences and IOP Publishing Ltd.

[Kurz et al., 2020] Kurz, C., Buizza, G., Landry, G., Kamp, F., Rabe, M., Paganelli, C., Baroni, G., Reiner, M., Keall, P. J., van den Berg, C. A. T., and Riboldi, M. (2020). Medical physics challenges in clinical MR-guided radiotherapy. *Radiation Oncology*, 15(1):93. Number: 1.

[Laeter et al., 2003] Laeter, J. R. d., Böhlke, J. K., Bièvre, P. D., Hidaka, H., Peiser, H. S., Rosman, K. J. R., and Taylor, P. D. P. (2003). Atomic weights of the elements. Review 2000 (IUPAC Technical Report). *Pure and Applied Chemistry*, 75(6):683–800. Publisher: De Gruyter.

[Lauterbur, 1973] Lauterbur, P. C. (1973). Image Formation by Induced Local Interactions: Examples Employing Nuclear Magnetic Resonance. *Nature*, 242(5394):190–191. Number: 5394 Publisher: Nature Publishing Group.

[Leeman et al., 2017] Leeman, J. E., Romesser, P. B., Zhou, Y., McBride, S., Riaz, N., Sherman, E., Cohen, M. A., Cahlon, O., and Lee, N. (2017). Proton therapy for head and neck cancer: expanding the therapeutic window. *The Lancet Oncology*, 18(5):e254–e265. Number: 5.

[Leifer, 1993] Leifer, M. C. (1993). RF Solenoid with Extended Equiripple Field Profile. *Journal of Magnetic Resonance, Series A*, 105(1):1–6.

[Lopez Schmidt et al., 2023] Lopez Schmidt, I., Haag, N., Shahzadi, I., Frohwein, L. J., Schneider, C., Niehoff, J. H., Kroeger, J. R., Borggrefe, J., and Moenninghoff, C. (2023). Diagnostic Image Quality of a Low-Field (0.55T) Knee MRI Protocol Using Deep Learning Image Reconstruction Compared with a Standard (1.5T) Knee MRI Protocol. *Journal of Clinical Medicine*, 12(5):1916. Number: 5 Publisher: Multidisciplinary Digital Publishing Institute.

[Markl and Leupold, 2012] Markl, M. and Leupold, J. (2012). Gradient echo imaging. *Journal of Magnetic Resonance Imaging*, 35(6):1274–1289. _eprint: https://onlinelibrary.wiley.com/doi/pdf/10.1002/jmri.23638.

[Marteau and Bekker, 1992] Marteau, T. M. and Bekker, H. (1992). The development of a six-item short-form of the state scale of the Spielberger State—Trait Anxiety Inventory (STAI). *British Journal of Clinical Psychology*, 31(3):301–306. Number: 3 _eprint: https://onlinelibrary.wiley.com/doi/pdf/10.1111/j.2044-8260.1992.tb00997.x.

[Mislow et al., 2010] Mislow, J. M., Golby, A. J., and Black, P. M. (2010). Origins of Intraoperative MRI. *Magnetic resonance imaging clinics of North America*, 18(1):1–10. Number: 1.

[Mispelter et al., 2006] Mispelter, J., Lupu, M., and Briguet, A. (2006). *NMR Probeheads for Biophysical and Biomedical Experiments: Theoretical Principles and Practical Guidelines*. Imperial College Press.

[Mitin and Zietman, 2014] Mitin, T. and Zietman, A. L. (2014). Promise and Pitfalls of Heavy-Particle Therapy. *Journal of Clinical Oncology*, 32(26):2855–2863. Number: 26 Publisher: Wolters Kluwer.

[NEMA, 2008] NEMA (2008). Determination of Signal-to-Noise Ratio (SNR) in Diagnostic Magnetic Resonance Imaging.

[Newhauser and Zhang, 2015] Newhauser, W. D. and Zhang, R. (2015). The physics of proton therapy. *Physics in Medicine & Biology*, 60(8):R155. Publisher: IOP Publishing.

[Nolden et al., 2013] Nolden, M., Zelzer, S., Seitel, A., Wald, D., Müller, M., Franz, A. M., Maleike, D., Fangerau, M., Baumhauer, M., Maier-Hein, L., Maier-Hein, K. H., Meinzer, H. P., and Wolf, I. (2013). The Medical Imaging Interaction Toolkit: challenges and advances. *International Journal of Computer Assisted Radiology and Surgery*, 8(4):607–620.

[Oborn et al., 2015] Oborn, B. M., Dowdell, S., Metcalfe, P. E., Crozier, S., Mohan, R., and Keall, P. J. (2015). Proton beam deflection in MRI fields: Implications for MRI-guided proton therapy. *Medical Physics*, 42(5):2113–2124. Number: 5 _eprint: https://onlinelibrary.wiley.com/doi/pdf/10.1118/1.4916661.

[Orzada et al., 2019] Orzada, S., Solbach, K., Gratz, M., Brunheim, S., Fiedler, T. M., Johst, S., Bitz, A. K., Shooshtary, S., Abuelhaija, A., Voelker, M. N., Rietsch, S. H. G., Kraff, O., Maderwald, S., Flöser, M., Oehmigen, M., Quick, H. H., and Ladd, M. E. (2019). A 32-channel parallel transmit system add-on for 7T MRI. *PLoS ONE*, 14(9):e0222452.

[Pascone et al., 1991] Pascone, R. J., Garcia, B. J., Fitzgerald, T. M., Vullo, T., Zipagan, R., and Cahill, P. T. (1991). Generalized electrical analysis of low-pass and high-pass birdcage resonators. *Magnetic Resonance Imaging*, 9(3):395–408.

[Platt et al., 2021] Platt, T., Ladd, M. E., and Paech, D. (2021). 7 Tesla and Beyond: Advanced Methods and Clinical Applications in Magnetic Resonance Imaging. *Investigative Radiology*, 56(11):705.

[Platt et al., 2018] Platt, T., Umathum, R., Fiedler, T. M., Nagel, A. M., Bitz, A. K., Maier, F., Bachert, P., Ladd, M. E., Wielpütz, M. O., Kauczor, H.-U., and Behl, N. G. (2018). In vivo self-gated 23Na MRI at 7 T using an oval-shaped body resonator. *Magnetic Resonance in Medicine*, 80(3):1005–1019. Number: 3 _eprint: https://onlinelibrary.wiley.com/doi/pdf/10.1002/mrm.27103.

[Pollard et al., 2017] Pollard, J. M., Wen, Z., Sadagopan, R., Wang, J., and Ibbott, G. S. (2017). The future of image-guided radiotherapy will be MR guided. *The British Journal of Radiology*, 90(1073):20160667. Number: 1073.

[Purcell et al., 1946] Purcell, E. M., Torrey, H. C., and Pound, R. V. (1946). Resonance Absorption by Nuclear Magnetic Moments in a Solid. *Physical Review*, 69(1-2):37–38. Publisher: American Physical Society.

[Raaymakers et al., 2017] Raaymakers, B. W., Jürgenliemk-Schulz, I. M., Bol, G. H., Glitzner, M., Kotte, A. N. T. J., Asselen, B. v., Boer, J. C. J. d., Bluemink, J. J., Hackett, S. L., Moerland, M. A., Woodings, S. J., Wolthaus, J. W. H., Zijp, H. M. v., Philippens, M. E. P., Tijssen, R., Kok, J. G. M., Breugel, E. N. d. G.-v., Kiekebosch, I., Meijers, L. T. C., Nomden, C. N., Sikkes, G. G., Doornaert, P. A. H., Eppinga, W. S. C., Kasperts, N., Kerkmeijer, L. G. W., Tersteeg, J. H. A., Brown, K. J., Pais, B., Woodhead, P., and Lagendijk, J. J. W. (2017). First patients treated with a 1.5 T MRI-Linac: clinical proof of concept of a high-precision, high-field MRI guided radiotherapy treatment. *Physics in Medicine & Biology*, 62(23):L41. Number: 23 Publisher: IOP Publishing.

[Radomsky et al., 2001] Radomsky, A. S., Rachman, S., Thordarson, D. S., McIsaac, H. K., and Teachman, B. A. (2001). The Claustrophobia Questionnaire. *Journal of Anxiety Disorders*, 15(4):287–297. Number: 4.

[Rana et al., 2013] Rana, S., Zeidan, O., Ramirez, E., Rains, M., Gao, J., and Zheng, Y. (2013). Measurements of lateral penumbra for uniform scanning proton beams under various beam delivery conditions and comparison to the XiO treatment planning system. *Medical Physics*, 40(9):091708. _eprint: https://onlinelibrary.wiley.com/doi/pdf/10.1118/1.4818283.

[Rezaeian et al., 2023] Rezaeian, P., Kashian, S., and Mehrara, R. (2023). Investigation of the effective atomic number dependency on kinetic energy using collision stopping powers for electrons, protons, alpha, and carbon particles. *Scientific Reports*, 13(1):3573. Number: 1 Publisher: Nature Publishing Group.

[Rooney et al., 2007] Rooney, W. D., Johnson, G., Li, X., Cohen, E. R., Kim, S.-G., Ugurbil, K., and Springer Jr., C. S. (2007). Magnetic field and tissue dependencies of human brain longitudinal 1H2O relaxation in vivo. *Magnetic Resonance in Medicine*, 57(2):308–318. _eprint: https://onlinelibrary.wiley.com/doi/pdf/10.1002/mrm.21122.

[Salvat, 2022] Salvat, F. (2022). Bethe stopping-power formula and its corrections. *Physical Review A*, 106(3):032809. Publisher: American Physical Society.

[Schlegel et al., 2018] Schlegel, W., Karger, C. P., and Jäkel, O., editors (2018). *Medizinische Physik: Grundlagen – Bildgebung – Therapie – Technik*. Springer, Berlin, Heidelberg.

[Seeber et al., 2004] Seeber, D., Jevtic, J., and Menon, A. (2004). Floating shield current suppression trap. *Concepts in Magnetic Resonance Part B: Magnetic Resonance Engineering*, 21B(1):26–31. Number: 1 _eprint: https://onlinelibrary.wiley.com/doi/pdf/10.1002/cmr.b.20008.

[Siemens, 2020] Siemens (2020). MAGNETOM Sola Betreiberhandbuch - syngo MR XA20 - Technische Daten. Siemens Healthineers, Erlangen, Germany.

[Slichter, 1978] Slichter, C. P. (1978). *Principles of Magnetic Resonance*. Springer Series in Solid-State Sciences. Springer, Berlin, Heidelberg.

[Spindeldreier et al., 2021] Spindeldreier, C. K., Klüter, S., Hoegen, P., Buchele, C., Rippke, C., Tonndorf-Martini, E., Debus, J., and Hörner-Rieber, J. (2021). MR-guided radiotherapy of moving targets. *Der Radiologe*, 61(1):39–48. Number: 1.

[Stollberger and Wach, 1996] Stollberger, R. and Wach, P. (1996). Imaging of the active B1 field in vivo. *Magnetic Resonance in Medicine*, 35(2):246–251. _eprint: https://onlinelibrary.wiley.com/doi/pdf/10.1002/mrm.1910350217.

[Taflove and Hagness, 2005] Taflove, A. and Hagness, S. C. (2005). *Computational Electrodynamics: The Finite-difference Time-domain Method*. Artech House. Google-Books-ID: n2ViQgAACAAJ.

[Taylor et al., 2012] Taylor, M. L., Smith, R. L., Dossing, F., and Franich, R. D. (2012). Robust calculation of effective atomic numbers: The Auto-Zeff software. *Medical Physics*, 39(4):1769–1778. _eprint: https://onlinelibrary.wiley.com/doi/pdf/10.1118/1.3689810.

[Thapa et al., 2016] Thapa, B., Kaggie, J., Sapkota, N., Frank, D., and Jeong, E.-K. (2016). Design and Development of a General-Purpose Transmit/Receive (T/R) Switch for 3T MRI, Compatible for a Linear, Quadrature and Double-Tuned RF Coil. *Concepts in Magnetic Resonance Part B: Magnetic Resonance Engineering*, 46B(2):56–65. _eprint: https://onlinelibrary.wiley.com/doi/pdf/10.1002/cmr.b.21321.

[Thomson, 2013] Thomson, M. (2013). *Modern Particle Physics*. Cambridge University Press.

[Tinganelli et al., 2015] Tinganelli, W., Durante, M., Hirayama, R., Krämer, M., Maier, A., Kraft-Weyrather, W., Furusawa, Y., Friedrich, T., and Scifoni, E. (2015). Kill-painting of hypoxic tumours in charged particle therapy. *Scientific Reports*, 5(1):17016. Number: 1 Publisher: Nature Publishing Group.

[Tommasino et al., 2016] Tommasino, F., Scifoni, E., and Durante, M. (2016). New Ions for Therapy. *International Journal of Particle Therapy*, 2(3):428–438. Number: 3.

[Tropp, 1989] Tropp, J. (1989). The theory of the bird-cage resonator. *Journal of Magnetic Resonance (1969)*, 82(1):51–62.

[Vaidya et al., 2016] Vaidya, M. V., Collins, C. M., Sodickson, D. K., Brown, R., Wiggins, G. C., and Lattanzi, R. (2016). Dependence of and field patterns of surface coils on the electrical properties of the sample and the MR operating frequency. *Concepts in Magnetic Resonance Part B: Magnetic Resonance Engineering*, 46(1):25–40. Number: 1 _eprint: https://onlinelibrary.wiley.com/doi/pdf/10.1002/cmr.b.21319.

[Vaughan et al., 1994] Vaughan, J. T., Hetherington, H. P., Otu, J. O., Pan, J. W., and Pohost, G. M. (1994). High frequency volume coils for clinical NMR imaging and spectroscopy. *Magnetic Resonance in Medicine*, 32(2):206–218. _eprint: https://onlinelibrary.wiley.com/doi/pdf/10.1002/mrm.1910320209.

[Vellet et al., 1995] Vellet, A. D., Lee, D. H., Munk, P. L., Hewett, L., Eliasziw, M., Dunlavy, S., Vidito, L., Fowler, P. J., Miniaci, A., and Amendola, A. (1995).

Anterior cruciate ligament tear: prospective evaluation of diagnostic accuracy of middle- and high-field-strength MR imaging at 1.5 and 0.5 T. *Radiology*.

[Virtanen et al., 2020] Virtanen, P., Gommers, R., Oliphant, T. E., Haberland, M., Reddy, T., Cournapeau, D., Burovski, E., Peterson, P., Weckesser, W., Bright, J., van der Walt, S. J., Brett, M., Wilson, J., Millman, K. J., Mayorov, N., Nelson, A. R. J., Jones, E., Kern, R., Larson, E., Carey, C. J., Polat, I., Feng, Y., Moore, E. W., VanderPlas, J., Laxalde, D., Perktold, J., Cimrman, R., Henriksen, I., Quintero, E. A., Harris, C. R., Archibald, A. M., Ribeiro, A. H., Pedregosa, F., and van Mulbregt, P. (2020). SciPy 1.0: fundamental algorithms for scientific computing in Python. *Nature Methods*, 17(3):261–272. Number: 3 Publisher: Nature Publishing Group.

[Webb and O'Reilly, 2023] Webb, A. and O'Reilly, T. (2023). Tackling SNR at low-field: a review of hardware approaches for point-of-care systems. *Magnetic Resonance Materials in Physics, Biology and Medicine*, 36(3):375–393.

[Weiland, 1977] Weiland, T. (1977). A discretization model for the solution of Maxwell's equations for six-component fields. *Archiv Elektronik und Uebertragungstechnik*, 31:116–120. ADS Bibcode: 1977ArElU..31..116W.

[Weiland, 1996] Weiland, T. (1996). Time Domain Electromagnetic Field Computation with Finite Difference Methods. *International Journal of Numerical Modelling: Electronic Networks, Devices and Fields*, 9(4):295–319. _eprint: https://onlinelibrary.wiley.com/doi/pdf/10.1002/%28SICI%291099-1204%28199607%299%3A4%3C295%3A%3AAID-JNM240%3E3.0.CO%3B2-8.

[Whelan et al., 2017] Whelan, B., Liney, G. P., Dowling, J. A., Rai, R., Holloway, L., McGarvie, L., Feain, I., Barton, M., Berry, M., Wilkins, R., and Keall, P. (2017). An MRI-compatible patient rotation system — design, construction, and first organ deformation results. *Medical Physics*, 44(2):581–588. Number: 2 _eprint: https://onlinelibrary.wiley.com/doi/pdf/10.1002/mp.12065.

[Wolf et al., 2005] Wolf, I., Vetter, M., Wegner, I., Böttger, T., Nolden, M., Schöbinger, M., Hastenteufel, M., Kunert, T., and Meinzer, H.-P. (2005). The medical imaging interaction toolkit. *Medical Image Analysis*, 9(6):594–604.

[Yee, 1966] Yee, K. (1966). Numerical solution of initial boundary value problems involving maxwell's equations in isotropic media. *IEEE Transactions on Antennas and Propagation*, 14(3):302–307. Conference Name: IEEE Transactions on Antennas and Propagation.

[Zhang et al., 2021] Zhang, B., Wang, K., and Jiang, T. (2021). RF power design optimization in MRI system. *Magnetic Resonance Letters*, 1(1):89–98.

[Zijlema et al., 2019] Zijlema, S. E., Tijssen, R. H. N., Malkov, V. N., Dijk, L. v., Hackett, S. L., Kok, J. G. M., Lagendijk, J. J. W., and Berg, C. A. T. v. d. (2019). Design and feasibility of a flexible, on-body, high impedance coil receive array for a 1.5 T MR-linac. *Physics in Medicine & Biology*, 64(18):185004. Publisher: IOP Publishing.

[Zinke and Brunswig, 1995] Zinke, O. and Brunswig, H. (1995). *Lehrbuch der Hochfrequenztechnik*. Number 1. Springer Berlin, Heidelberg, 5 edition.

List of Figures

2.1 Energy level scheme for a nucleus with $I = \frac{1}{2}$. 7
2.2 Decomposition of a linearly-polarized RF field into circularly-polarized field components with opposite angular directions of rotation. 13
2.3 A linear gradient field for slice selection in the z direction G_z allows for uniform spatial encoding, where the relationship between the bandwidth and the slice thickness depends on the slope of the gradient. 15
2.4 Schematic illustration of a solenoid coil with a capacitor on the conductor to adjust the resonance frequency. 21
2.5 Schematic illustration of a birdcage resonator in a low-pass and high-pass configuration. 22
2.6 Illustration of a linearly-polarized and a circularly-polarized B_1-field for different phases generated in a birdcage resonator. 23
2.7 Schematic of a series RLC circuit and a matching network for impedance matching of the RLC circuit including a parallel capacitor and a serial reactance. 27
2.8 Illustration and schematic of a quadrature hybrid including inductors and capacitors. 29
2.9 Functionality of a transmit/receive switch that separates the transmit and receive paths. 30
2.10 Schematic of a π-element between an RF input ($\mathrm{RF_{in}}$) and an RF output ($\mathrm{RF_{out}}$) consisting of an inductor and two capacitors. 31
2.11 π-element between transmit and receive path with illustration of the two switching states using a PIN diode. 32
2.12 Illustration of a Yee cell representing a hexahedral voxel on a three-dimensional grid (i, j, k) with spatial coordinates (x, y, z) including electric and magnetic field components. 34

3.1 Whole-body closed-bore MR system with a static magnetic field of 1.5 T. 40
3.2 A Tim Coil Interface adapter required to connect custom RF coils to the coil socket of the "offline" 1.5 T MR system. 41
3.3 C-shaped permanent magnet with a magnetic field strength of 0.25 T. 42

3.4 3D model of the RF body coil with a human voxel model on a custom pad to simulate realistic patient loading. 45
3.5 Cross-sectional view of the layered structure of the developed RF coils. 46
3.6 3D model of the developed RF calf coil including the three positions for the tuning capacitors and the matching network where the RF coil is connected to the scanner via a coaxial cable. 48
3.7 Schematic structure of the transmit and receive chain for the developed RF body coil. 50
3.8 Measurement setup of the RF body coil at the "offline" 1.5 T MR system. 51
3.9 Measurement setup of the developed RF calf coil including the developed preamplifier and the constructed holder at the "online" 0.25 T MR system. 53
3.10 Torso and calf phantoms used for MR measurements and simulations, as well as body parts from heterogeneous voxel models for calculation of realistic dielectric properties. 55
3.11 Torso-sized anthropomorphic phantom used for MR measurements with the RF body coil to simulate realistic patient loading. 56
3.12 Simplified models of the "offline" 1.5 T and "online" 0.25 T MR systems with the components essential for the RF field calculations of the RF coils. 57
3.13 Schematic of a balanced matching network with one parallel and two serial capacitors for impedance matching. 60
3.14 Schematic of a designed transmit/receive switch for the "offline" 1.5 T MR system, including the capacitors, inductors, and resistors involved. 64
3.15 Transmit/receive switch with a preamplifier designed for 63.68 MHz. . 66
3.16 Realization of a quadrature hybrid at 63.68 MHz. 67
3.17 Schematic of the designed preamplifier for the "online" 0.25 T MR system, including the capacitors, inductors, and resistors involved. . . 69
3.18 Low-noise preamplifier design to amplify the received MR signal from the RF calf coil. 70
3.19 Measurement setup of the Peakfinder water column to determine the depth dose curves of particle beams. 76

4.1 Stopping powers in copper, polyimide, PMMA and water for protons and carbon ions in the clinically relevant energy range. 81
4.2 Measured depth dose curve for carbon ions in the water column during irradiation of the flexible printed circuit board including the conductor. 83
4.3 Simulated S-parameters at the two matching networks of the RF body coil for all rotation angles of the homogeneous torso phantom and the human voxel model. 86

4.4 Relative transmit and receive field distributions for three orthogonal slices at the center of the homogeneous torso phantom in horizontal position (0° rotation). 89
4.5 Relative transmit and receive field distributions for three orthogonal slices at the center of the homogeneous torso phantom in a rotated position (30° rotation). 90
4.6 Measured and simulated coefficients of variation for the transmit and receive field of the radiation-transparent RF body coil calculated for a full rotation of the patient capsule with a homogeneous torso phantom and a human voxel model. 94
4.7 The measured and simulated transmit power efficiencies of the radiation-transparent RF body coil in the homogeneous torso phantom and the heterogeneous human voxel model. 96
4.8 Comparison of the measured SNR for the radiation-transparent RF body coil and the internal body coil of the MR scanner. 97
4.9 SAR limits and the corresponding maximum allowable average RF power of the developed RF body coil. 98
4.10 MR images for a coronal slice of a heterogeneous torso-sized phantom filled with organ-simulating substances. 99
4.11 Simulated reflection coefficient at the matching network of the RF calf coil determined for all rotation angles of the RF calf coil including the homogeneous calf phantom and the human voxel model. 100
4.12 Simulated relative receive field distributions (B_1^-) for the central transverse, coronal and sagittal slices in a cylindrical homogeneous phantom and a heterogeneous voxel model of a human calf. 101
4.13 Coefficient of variation for the receive field of the radiation-transparent RF calf coil calculated in a ROI in a homogeneous cylindrical phantom and a voxel model of a human calf for a complete rotation of the RF calf coil and phantom. 102
4.14 MR images in the transverse, sagittal, and coronal slices at the center of the homogeneous calf phantom acquired with the radiation-transparent RF calf coil, the commercial cervical coil, and the commercial knee coil. 103
4.15 Line plots of the signal intensity in the homogeneous calf phantom along each central axis for the radiation-transparent calf coil, the commercial cervical coil, and commercial knee coil. 104
4.16 In vivo images of a human calf illustrating different image contrasts (T_1-weighted, T_2-weighted). 107
4.17 In vivo images of a human hand illustrating different image contrasts (T_1-weighted, T_2-weighted). 108

List of Tables

2.1 SAR limits for volume transmit coils from the IEC. 24
2.2 Calculated inductance and capacitance values of a quadrature hybrid at 63.9 MHz. 30
2.3 Calculated inductance and capacitance values of a π-element at 63.9 MHz. 32

3.1 Comparison of simulated and actual tuning capacitor values to tune the resonance frequency of the two developed RF coils to the corresponding Larmor frequency. 59
3.2 Reflection coefficient (S_{11}) and impedance matching at the two coil ports (P1, P2) of the RF body coil and the port of the RF calf coil, measured at the corresponding Larmor frequencies. 61
3.3 S-parameters between the different RF ports of the transmit/receive switch during transmission and reception, measured at 63.68 MHz. . . 65
3.4 S-parameters, transmitted power and accumulated phases between the different RF outputs of the quadrature hybrid measured at 63.68 MHz. 67

4.1 Material properties for the different layers in the developed RF coils. 80
4.2 Calculated stopping power ratio relative to water for materials of the developed RF coils averaged over the clinically relevant energy range. 81
4.3 Measured change in the peak position, the D_{50} position and the width of the Bragg peak in the depth dose curve for the irradiation of different RF coil layers in comparison to the reference measurement with no materials in front of the water column. 84
4.4 Nominal FOV for the phantom MR measurements with the radiation-transparent RF body coil and the internal body coil for the three central slices with a phantom rotation of 0° and 30°, respectively. . . 88
4.5 Coefficients of variation calculated for the measured and simulated transmit (B_1^+) and receive fields (B_1^-) of the radiation-transparent RF body coil and the internal RF body coil with a homogeneous torso phantom in horizontal position and in a position rotated by 30°. 91

4.6 Average signal intensity, coefficient of variation, image noise and SNR of the radiation-transparent RF calf coil and of the two commercial RF coils calculated in a ROI for the measured three central slices in the homogeneous calf phantom. 105
4.7 MR sequence parameters for 2D in vivo imaging of a human calf and hand using a T_1-weighted spin echo and a T_2-weighted gradient echo (Dixon) sequence. 106

Acronyms

2D	Two dimensional
3D	Three dimensional
ARTEMIS	Adaptive Radiotherapy with Ion beams
BLADE	MR sequence with reduced motion artifacts
bSSFP	balanced Steady State Free Precession
COV	Coefficient of variation
CP	Circularly-polarized
CT	Computer tomography
DC	Direct current
DICOM	Digital Imaging and Communications in Medicine
DNA	Deoxyribonucleic acid
EM	Electromagnetic
FA	Flip angle
FDTD	Finite difference time domain
FFT	Fast Fourier Transform
FID	Free induction decay
FIT	Finite integration technique
FOV	Field of view
GRE	Gradient echo
HIT	Heidelberg Ion Beam Therapy center
IEC	International Electrotechnical Commission
linac	Linear accelerator
LP	Linearly-polarized
MITK	Medical Imaging Interaction Toolkit
MR	Magnetic resonance
MRgPT	Magnetic resonance-guided particle therapy
MRgRT	Magnetic resonance-guided radiotherapy
MRI	Magnetic resonance imaging
NMR	Nuclear magnetic resonance

OAR	Organs at risk
PIN	Positive intrinsic negative
PCB	Printed circuit board
PEC	Perfect electrical conductor
PMMA	Polymethylmethacrylate
PVP	Polyvinylpyrrolidone
RBE	Relative biological effectiveness
RF	Radiofrequency
ROI	Region of interest
Rx	Receive
SAR	Specific absorption rate
SE	Spin echo
SINC	$\frac{sin(x)}{x}$
SNR	Signal-to-noise ratio
SPR	Stopping power ratio
$\mathbf{T_E}$	Echo time
$\mathbf{T_R}$	Repetition time
Tx	Transmit
VIBE	Volumetric interpolated breath-hold examination
WET	Water equivalent thickness

Acknowledgements

I would like to thank all the people who supported me during my time as graduate student, especially:

- **Prof. Dr. Mark E. Ladd** for supervising my doctoral studies at the Faculty of Physics at the University of Heidelberg, for evaluating this thesis as first referee, and for giving me the opportunity to work at the Department of Medical Physics in Radiology at the German Cancer Research Center (DKFZ).
- **Prof. Dr. Leif Schröder** for evaluating this thesis as second referee.
- **Prof. Dr. Dr. Jürgen Debus** for creating the opportunity to perform research in the intriguing interdisciplinary field of MR-guided particle therapy at the Heidelberg University Hospital and the Heidelberg Ion Therapy Center.
- **Dr. Sebastian Klüter** for the coordination of the ARTEMIS project (Adaptive Radiotherapy with Ion beams) and my position, as well as supporting further personal training in the field of medical physics for physicists.
- **Dr. Tanja Platt** for the support, the many informative explanations, the helpful advice, the friendly communication, and the flawless supervision in general.
- **Dr. Stephan Orzada** for the many helpful advice in the field of RF technology.
- **Dr. Thomas M. Fiedler** for the helpful and instructive advice to improve electromagnetic field simulations.
- **Dr. Stephan Brons** for the support with radiation measurements at the HIT.
- **Dr. Stefan Dorsch** for the support and the coordination of MR measurements.

- **Cedric Beyer** for the support in preparing the measurement setup at the "offline" MR system at 1.5 T.
- **Fabian Dinkel & Gernot Echner** for the intensive cooperation and creative ideas for the practical implementation of the rotation setup.
- **Employees of the precision mechanics workshop** for the technical support.
- **Christian Kindtner** for the support with organizational matters at the DKFZ.
- **Colleagues in the ARTEMIS project** for the successful cooperation in the interdisciplinary field of MRgPT.
- **Colleagues in the 7T group of the DKFZ** for interesting lunch discussions and the friendly work environment.
- **Family & Friends** for their unconditional support during my time as a graduate student.

Declaration

I hereby declare that I wrote this thesis independently, and that I have used only the specified sources and tools.

Heidelberg, 27.11.2023 .....